博士論文

Theoretical investigations on controlling the properties of semiconductor photocatalysts by modifying structural factors

(半導体光触媒の構造的要因を利用した物性制御に関する理論的研究)

久保　綾子

Theoretical investigations on controlling the properties of semiconductor photocatalysts by modifying structural factors

Ayako Kubo

Department of Chemical System Engineering

Graduate School of Engineering

The University of Tokyo

February 2015

Preface

With the explosion of energy demand and the drastic growth of environmental issues associated with the rapid industrialization in a global scale, renewable and environmentally friendly energy resources alternative to fossil fuels have been exhaustively explored during these decades. Among a number of possible candidates for the alternative energy resources, hydrogen fuel generated through the photocatalytic or photoelectrochemical water splitting is considered to be the most promising one, since it only needs the abundant resources (water and sunlight) and only emits the harmless product (water).

Most of the photocatalysts and photoelectrodes are semiconductors, and their activities are strongly related to their fundamental properties. In particular, semiconductor photocatalyts that consist of mixed ion compounds such as oxynitrides and solid solutions have been getting wide attention due to the broad range of controllability of their fundamental properties resulting from the wide variety of their structural features. Nevertheless, there still remains a crucial difficulty in understanding the relation between their properties and structural factors owing to their complexity, and thus the guidelines to control their properties have not been fully obtained.

Hence, in this thesis, the author tried to investigate the structural and the electronic features of such mixed ion compounds by means of first-principle calculations, in order to directly relate the two complex features. Furthermore, by understanding the relation between the structural and

electronic features, the author aimed to provide the guidelines to control their properties and to enhance their photocatalytic or photoelectrochemical activities for water splitting. The author finally accomplished the theoretical studies on four different mixed ion compounds in this thesis: conventional perovskite oxynitrides ($CaTaO_2N$ and $MgTaO_2N$), perovskite solid solution ($LaMg_xTa_{1-x}O_{1+3x}N_{2-3x}$), and chalcopyrite solid solution ($(ZnSe)_{0.85}(CuIn_{0.7}Ga_{0.3}Se_2)_{0.15}$). The contents of this thesis are outlined as follows.

In chapter 1, the general background of this thesis is introduced including the basic knowledge of the photocatalyst and photoelectrodematerials such as their reaction processes, historical overviews, and present status. The author especially shed light on the importance and the difficulty of investigating the mixed ion compounds in order to demonstrate the motivation of the research objectives of this thesis.

In chapter 2, the theoretical framework to calculate the electronic structures of solids from first principle is introduced. In particular, the author focused on how the electronic structures of materials are obtained from the geometry of their constituent atomic nuclei, and traced the development of the theories basing on the fundamental quantum mechanics. Additionally, the approximate methods used in the calculations of the electronic structures of many body systems such as solids are introduced, and their influence on the description of the electronic structures are explained.

In chapter 3, the study on the specific anionic arrangements of O/N (= anion ordering) in

$CaTaO_2N$ is presented. In particular, the correlation between the anion ordering and the photocatalytic related properties such as bandgaps, carrier effective masses, and band edge positions is investigated, and consequently the guidelines to modify the properties of $CaTaO_2N$ by controlling its anion ordering are provided.

In chapter 4, the applicability of $MgTaO_2N$, a theoretically predicted novel oxynitride photocatalyst, is discussed by investigating the effect of octahedral-tiltings and crystal polymorphism that had not been considered in the previous theoretical studies. Here, the fundamental properties of $MgTaO_2N$ in perovskite polymorph with octahedral-tiltings and in ilmenite polymorph are investigated, and their applicability as water splitting photocatalysts are estimated. Besides, based on the calculation results, the relation between the octahedral-tiltings and the photocatalyst related properties in perovskites are disclosed.

In chapter 5, the author focused on $LaMg_xTa_{1-x}O_{1+3x}N_{2-3x}$ ($0 \leq x \leq 2/3$), a solid solution photocatalyst that had achieved overall water splitting under visible light. Here, I investigated the dependence of its photocatalyst related properties on its composition in order to reveal the factor that made the photocatalytic activity of $LaMg_xTa_{1-x}O_{1+3x}N_{2-3x}$ reach the maximum at $x = 1/3$.

In chapter 6, I focused on $(ZnSe)_{0.85}(CuIn_{0.7}Ga_{0.3}Se_2)_{0.15}$, a solid solution photocathode material consisting of p-type semiconductor. Here, I investigated the structures and the properties of the point defects in $(ZnSe)_{0.85}(CuIn_{0.7}Ga_{0.3}Se_2)_{0.15}$ in order to unravel the origin of the p-type

characteristics of this material. I also estimated the dependence of the concentrations of such defects and the positive carriers on the external conditions, such as partial pressures, to obtain a guideline to enhance its photocathodic activities.

Finally, in chapter 7, I summarized the research topics, results, and the conclusions reported in the previous chapters, and subsequently presented the concluding remarks based on the insights obtained through this thesis. Furthermore, a future outlook was provided in order that the next challenges to develop the photocatalytic research field may be presented for the researchers in the future generations.

Here, I would like to express my deepest gratitude to the people who had supported my work in my Ph.D. program. First, I would like to appreciate Professor Koichi Yamashita for providing me great guidance and encouragement on my studies as the supervisor. He also gave me many opportunities to gain a wide range of experience by supporting me to join conferences, workshops, internships, and collaborative researches with experimentalists. It was really a meaningful time for me to engage in academic research under him for five years.

I’m also grateful to Associate Professor Hiroshi Ushiyama for giving me a lot of advice on my studies. Especially, I really thank him for having offered me a beneficial counseling when I need any advice and comments on preparing for academic presentations and reports.

As the examiners for my defense from other laboratories, I would also like to show my

acknowledgements to Professor Atsuo Yamada, Professor Kazuya Yamaguchi, Associate Professor Toru Wakihara, and Associate Professor Tsutomu Minegishi. I especially appreciate for their attendance to my defense despite being busy, and giving me a lot of beneficial advice for brushing up my thesis.

For the great instruction in conducting the researches, I would like to express my sincere appreciation to Associate Professor Giacomo Giorgi in the University of Perugia, who is a former member of our laboratory. Since I joined this laboratory in 2013, he had provided me comprehensive direction for the academic research, from the introduction of the research background to the guidelines to use the computational programs. With his great guidance and care, I could finally complete the studies on perovskite oxynitrides as collaborate researches with him.

Immeasurable direction and supports were also provided from the members in Domen's laboratory, which is a group of experimentalists on photocatalysts and related materials. Professor Kazunari Domen had arranged me regular discussion on my research, with giving me a lot of information of the state-of-the-art findings on photocatalysts. Associate Professor Tsutomu Minegishi and Mr. Hiroyuki Kaneko also had provided me thorough discussion on photoelectrode materials consisting of chalcopyrite solid-solution, which finally led to the joint research among us. It was a very fruitful experience for me to collaborate with experimentalists, and thus I would like to deeply thank all the people involving me with the joint research.

I also thank to my colleagues in Yamashita-Ushiyama's laboratory for a lot of supports and encouragements. Research Associate Professor Hiroyuki Tamura and Assistant Professor Mikiya Fujii gave me lots of helpful advice on academic life, academic reports, presentations, and career planning. They also offered me many opportunities to interact with people in academic field during conferences and workshops. Many current and former academic staffs, Dr. Kenji Mishima, Dr. Pradeep R. Varadwaj, Dr. Saeid Arabnejad K., Dr. James S. M. Anderson, Ms. Arpita Varadwaj, Dr. Hideyuki Kamisaka, Dr. Ryota Jono, Dr. Ahmed Slimani, Dr. Xuefang Yu, also gave me a lot of beneficial advice both on researches and daily lives. Two secretaries, Ms. Mayumi Iyama and Ms. Noriko Sanpei also supported me in various areas of my academic life. Dr. Hiroki Kawai and Dr. Tomoyuki Hata, my senior colleagues in photocatalyst group of our laboratory, had also provided me great guidance and care in conducting the research and preparing for presentations and reports. The senior colleagues of the other groups of our lab., Dr. Ayaka Kuroki, Dr. Tomotaka Kunisada, Dr. Eriko Watanabe, and Mr. Katsuhiko Nishimra, had also helped me on learning the basis of theoretical frameworks and setting up the computational environment. The junior colleagues in Ph.D. program, Mr. Masanori Kaneko and Mr. Eisuke Kawashima, had also provided me a great deal of technical help as machine administrators. I would also like to thank all the other students for sharing the cheerful days with me.

Here, I'm also grateful to the support from the Program for Leading Graduate Schools MERIT (Materials Education program for the future leaders in Research, Industry, and Technology).

The program had offered me not only the strong financial support but also a variety of educational opportunities to learn a wide range of research field related to material science. I also express great appreciation to Ito Scholarship Foundation, who had provided me the opportunity to attend college with a great financial support, and to interact with talented students from different disciplines. Acknowledgements are also expressed to the Supercomputer Center in Institute for Solid State Physics (ISSP) of University of Tokyo and the Research Center for Computational Science in Institute for Molecular Science (IMS) in Okazaki. Most of the theoretical calculations in this thesis were performed using their facilities. I would also like to thank the "Katsushika Library" of Tokyo University of Science and the "Katsushika Central Library" of Katsushika city for providing me the place for writing my thesis. It was very helpful for me to have comfortable spaces to conduct my work not only inside but also outside the laboratory.

Finally, I would like to express great appreciate to my family for encouraging me to enroll in Ph.D. program, and supporting me for these twenty-six years.

Tokyo February 2018 *Ayako Kubo*

Contents

Chapter 1.
General Introduction

1-1. Photocatalyts and photoelectrode systems for hydrogen production

Starting with the industrial revolution occurred in the United Kingdom in the 18th century, we, the human race, have established a lifestyle based on fossil fuels such as coals and petroleum oil as indispensable energy resource. However, as the energy demand expands drastically due to the world population explosion and rapid industrialization after the middle of the 20th century, the depletion of such fossil fuels is getting more and more accelerated. Furthermore, the increasing of the greenhouse effect gas such as CO_2 associated with the consumption of fossil fuels has been causing serious problems such as massive weather disasters and global ecological destruction through accelerating the global warming. Therefore, it has been an urgent issue for the human family to secure a new and clean energy resources alternative to fossil fuels.

One of the promising candidates for the alternative energy resources is hydrogen. Hydrogen is a fuel that can be directly converted to electrical energy by using fuel cells, only emitting water as a by-product (Eq (1.1)).

$$2H_2 + O_2 \rightarrow 2H_2O + \text{energy} \qquad (1.1)$$

Thus, hydrogen is considered to be a clean fuel that doesn't causes any environmental problem. Also, hydrogen is rather suitable to the existing energy infrastructure, since it has been already utilized in fuel cell vehicles and some private power systems. However, most of the hydrogen fuels currently used are produced through steam methane reforming (Eq (1.2) and Eq (1.3)), accompanying the consumption of fossil fuels and the emission of CO_2 [1].

$$CH_4 + H_2O \rightarrow CO + 3H_2 \quad (1.2)$$

$$CO + H_2O \rightarrow CO_2 + H_2 \quad (1.3)$$

Therefore, in order to utilize hydrogen as an alternative fuel to the conventional fossil fuels, we need to establish more clean and renewable processes for hydrogen productions.

Hence, recently, the hydrogen production through water splitting using the energy of sunlight has been attracting wide attention, since both water and sunlight are ubiquitous and abundant resource that will never be exhausted. In particular, the total amount of the solar energy that reaches to the surface of the earth is estimated to be about 8.5×10^{16} W, which means that only the energy of an hour's irradiation corresponds to the annual energy consumption of the world [2]. Besides, since only oxygen will be emitted as the by-product of the hydrogen production through water splitting, they will never destroy the global environment. For these reasons, water splitting using the solar energy will make the hydrogen fuel a clean and renewable energy resource.

Indeed, water splitting using solar energy has already been accomplished by several different

ways. One is to electrolyze water using the electric power generated by photovoltaic cells. In this manner, about 24 % of solar-to-hydrogen conversion efficiency (STH) have been achieved in a previous study [3]. The second way is to split water directly using a photocatalyst, a compound that works like a catalyst only under the light irradiation. Using such water splitting photocatalysts, it has already succeeded to produce hydrogen at the efficiency more than 1 % of STH [4]. The third one is to split water using a photoelectrode system, which consists of two electrodes that are made of photocatalyst materials suitable to oxidize and reduce water, respectively. In this manner, experimentalists have also achieved overall water splitting at nearly 1 % of STH [5]. Among these methods, water splitting using photocatalyst and photoelectrodes systems are considered to be advantageous in terms of the costs that will be incurred in practical use, since they consist of rather simple systems than the combination of photovoltaic cell and electrolysis apparatus. Hence, the developments of highly efficient photocatalysts and photoelectrode systems are strongly desired in order to realize the mass production of hydrogen fuels utilizing the energy of sunlight.

1-2. Basic process of photocatalyts and photoelectrodes

Generally, both photocatalysts and photoelectrode materials used in water splitting consist of semiconductors. Semiconductors have an energy gap (bandgap: E_g) between their valence band (VB) and conduction band (CB), and thus can absorb photons through the electronic excitation between both bands. The energy of the absorbed light through the inter-band excitation is utilized to split water in both photocatalysts and photoelectrode systems, and thus the basic processes of the water splitting in the two systems are quite similar.

The basic processes of the water splitting reaction using a photocatalyst can be explained as follows (and also depicted in Figure 1-1). First, when a photocatalyst achieved a light irradiation, the electrons in their valence band will be exited to the conduction bands to generate photoexcited electrons with negative charges and residual holes with positive charges. Then, the charged carriers will diffuse in the crystals, and some of them will reach the surface of the photocatalysts. Finally, these carriers will be transferred to the absorbed species such as water molecules and protons at the photocatalyst surface and produce hydrogen and oxygen through the redox reactions (Eq (1.4) and Eq (1.5)).

$$2H^+ + 2e^- \rightarrow H_2 \quad (1.4)$$

$$2H_2O + 4h^+ \rightarrow O_2 + 4H^+ \quad (1.5)$$

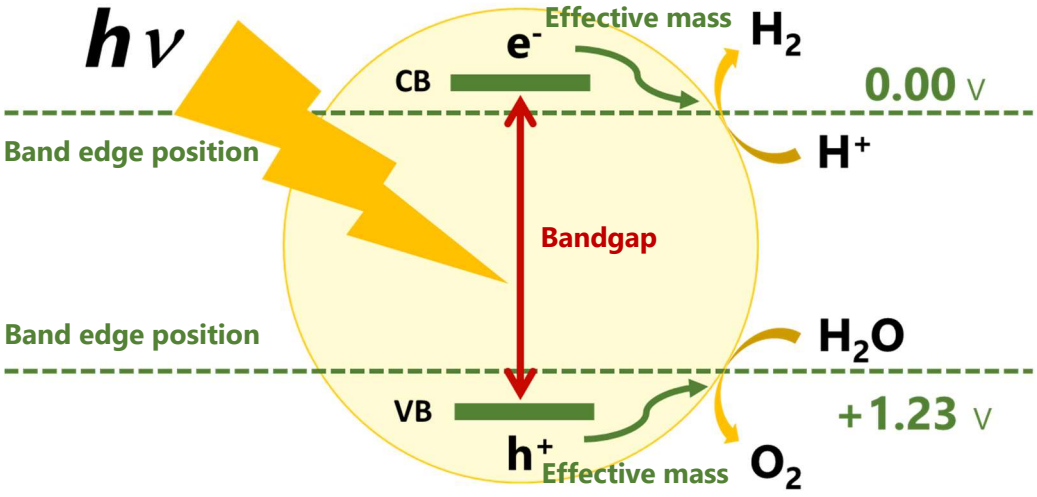

Figure 1-1. The schematic illustration of the basic processes of photocatalytic water splitting.

Usually, the activities of the water splitting photocatalysts are strongly related to the fundamental properties of the constituent semiconductors, as also depicted in Figure 1-1. For instance, the ranges of the wavelengths which can be absorbed by the photocatalysts are determined by the width of their bandgaps. Besides, the degrees of the carrier diffusion are influenced by the carrier effective masses that are related to the extent of their band dispersions, and the abilities to redox water are determined by the position of their band edges relative to the redox potentials (0 V vs. NHE for H_2 evolution and 1.23 V vs. NHE for O_2 evolution). Therefore, it is considered that one can efficiently control the activities of photocatalysts by modifying their fundamental properties.

On the other hand, the basic processes of photoelectrode systems are a little bit more

complicated. As mentioned in the previous section, a water splitting photoelectrode system consists of a photoanode for oxygen evolution and a photocathode for hydrogen evolution, connected to each other by an electric lead (Figure 1-2). Usually, n-type and p-type semiconductors are used as photoanodes and photocathodes, respectively, and the band edge positions (VB maximum: VBM, and CB minimum: CBM) of the former are more positive than those of the latter. Therefore, an upward and a downward band bending occurs in a photoanode and a photocathode, respectively, when they are connected to each other. Here, as the light irradiated to the system, photoexcited electrons in the photocathode and holes in the photoanode will be moved toward the surface and thus hydrogens and oxygens will be produced respectively. On the other hand, the residual holes in the former and photoexcited electrons in the latter will move to the opposite electrode through the electric lead, producing a photocurrent. Hence, the activities of photoelectrode systems are usually evaluated by the degree of their photocurrents.

Generally, the photocurrents of the electrode are strongly influenced by the extent of their band bending, which depends on their electrode potential, and thus the photocurrents also depend on the electrode potentials. Conventionally, the dependence of the photocurrent on the electrode potential is represented by a current density versus potential curve (Figure 1-3), where the intersection of the curve and the voltage axis (the voltage where the photocurrent begins to flow) is called the onset potential. Usually, the curves of the photocathodes are negatively sloped, and those of photoanodes

are positively sloped. In addition, the degrees of photocurrents generated in the two connected electrodes have to be the same, and thus this will be represented by the intersection of the two curves of both electrodes (as depicted in Figure 1-3(c)). Therefore, in order to increase the photocurrent of the photoelectrodes system, one needs to improve the photocurrent of each electrode, or widen the difference between the onset potentials of the electrodes. Since the degree of the photocurrent and the onset potential of each electrode are determined by the positions of its band edges and Fermi energy, modifying these properties will be efficient to improve the activities of photoelectrode systems.

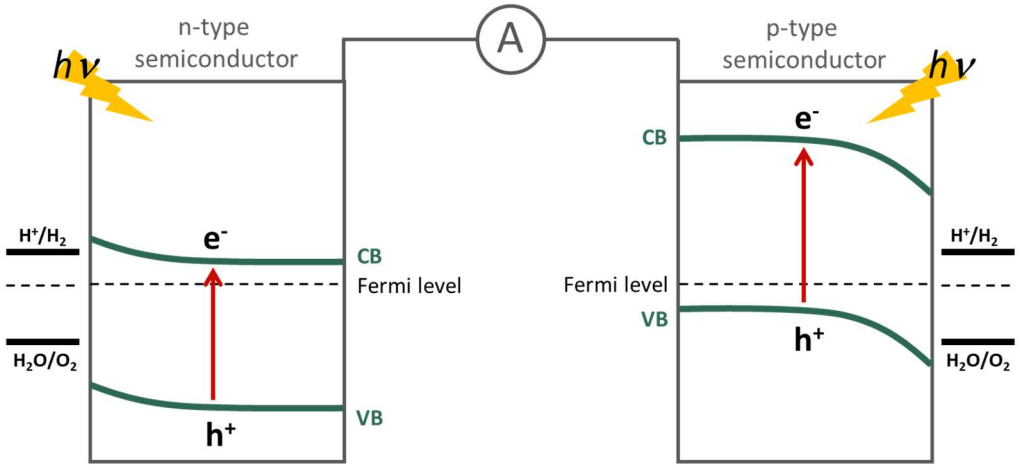

Figure 1-2. The schematic illustration of a photoelectrode system and the basic processes of photoelectric water splitting.

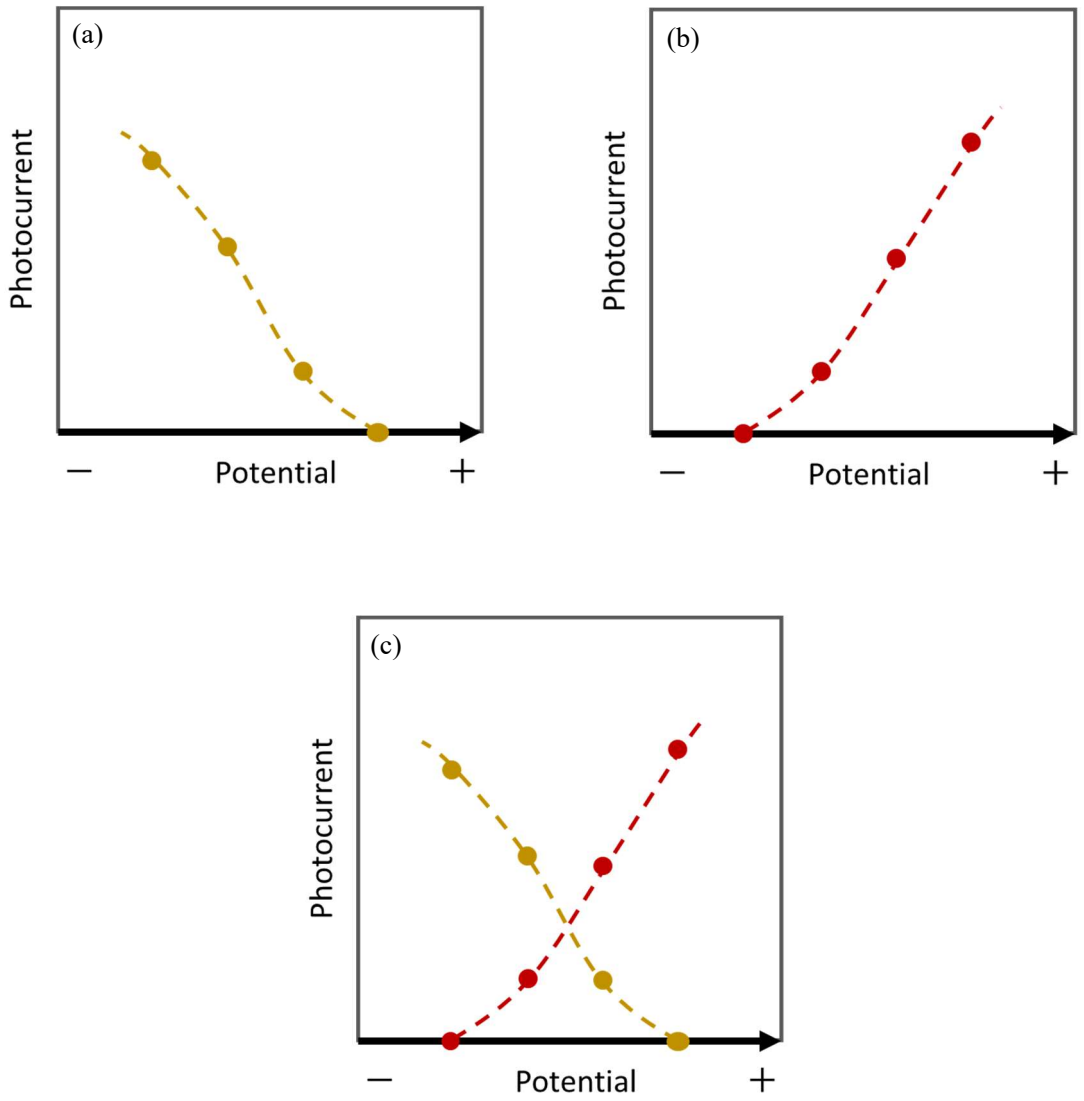

Figure 1-3. The schematic illustration of the current density versus potential curves for (a) photocathodes, (b) photoanodes, and (c) both electrodes superimposed in a single graph.

1-3. Historical overview and present status

The researches on photocatalyst and photoelectrode systems had started with Honda-Fujishima effect [6], which was reported in 1972. They had developed an electrode system consisting of TiO_2 and Pt metal connected in water, and discovered that water molecules were split into oxygens and hydrogens in stoichiometric ratio on the surface of each electrode, respectively, under the irradiation of ultraviolet (UV) light. Here, TiO_2 had functioned as photoanode and Pt metal had functioned as photocathode.

Thereafter, it was revealed that the similar water splitting reactions occur not only in the above photoelectrode system but also on the particle photocatalyst which consists of TiO_2 particle with Pt nanoparticles deposited on its surface [7]. It is considered that the Pt nanoparticles capture the photoexcited electrons to produce hydrogens, and the remaining holes move toward the surface of TiO_2 photocatalyts to produce oxygens. As well as TiO_2, there had been discovered a large number of novel photocatalyst materials such as $SrTiO_3$[8], $K_4Nb_6O_{17}$[9], $BaTi_4O_9$[10], ZrO_2[11], $NaTaO_3$[12], $ZnGa_2O_4$[13], Sr_2SnO_4[14], most of which consists of metal oxides with d^0 or d^{10} electronic state.

However, there was a serious drawback in those metal oxide photocatalysts – their bandgaps are so large that they can only absorb the energy of UV light. Generally, the valence bands of metal oxides consist of O 2p orbitals whose electronic levels are relatively deep, and thus their bandgaps tend to be as large as the energy of UV light ($E_g > 3$ eV). However, UV light dominates only 6 % of

the entire solar spectrum, and most of the remaining part consists of visible-light (52 %) and infrared light (42 %) [15]. Therefore, one needs to collect not only UV light but also visible-light with much longer wavelength in order to utilize the energy of sunlight more efficiently.

In accord with that, a number of visible-light responsive photocatalysts have been developed after 2000's. In particular, Domen *et al.* has succeeded in achieving visible-light responsibility by using nitrides (Ta_3N_5[16]), oxynitrides ($LaTiO_2N$ [17], TaON [18], GaN:ZnO [19], $ATaO_2N$(A=Ba, Sr, Ca) [19]), sulfides ($ZnIn_2S_4$ [20]), and oxysulfides ($LnTi_2S_2O_5$ (Ln = Pr, Nd, Sm, Gd, Tb, Dy, Ho, and Er) [21]) as novel photocatalysts. These photocatalysts have the contribution of N 2p or S 3p orbitals, whose energy levels are more negative than those of O 2p orbitals, in their valence bands, and thus they had realized higher valence band positions and narrower bandgaps which corresponds to the energy of visible-light.

Now, it is well known that N^{3-} and S^{2-} are more susceptible to a self-oxidation reaction than O^{2-}. Hence, nitrides and sulfides are usually inferior in the stabilities to oxides under aqueous environments. On the other hand, oxynitrides and oxysulfides have the properties intermediate between nitrides (or sulfides) and oxides, and this enables them to balance the two competing factors, smaller bandgaps and higher stabilities [22]. Therefore, the mixed anion compounds like oxynitrides and oxysulfides have become the central research area of photocatalysts during these decades.

Furthermore, novel photocatalysts that consist of solid solutions between existing materials

have been newly reported these days. For instance, $LaMg_xTa_{1-x}O_{1+3x}N_{2-3x}$, a solid solution between $LaTaO_2N$ and $LaMg_{2/3}Ta_{1/3}O_3$ have accomplished overall water splitting under visible light irradiation with the wavelength up to 600 nm [23]. There also exists a number of other examples such as $LaSr_xTa_{1-x}O_{1+2x}N_{2-2x}$ [23], $Cu_xAg_yIn_{x+y}Zn_{2(1-x-y)}S_2$[24], $Zn_{1-2x}(CuGa)_xGa_2S_4$ [25], $La_5Ti_2Cu(S_{1-x}Se_x)_5O_7$ [26], and $Na_xLa_{1-x}TaO_{1+2x}N_{2-2x}$ [27] on which photocatalytic activities have been reported. These kind of photocatalysts have a remarkable advantage in possible fine tuning of their band structures by changing their compositions [27- 29]. In other words, solid solution photocatalysts have expanded the controllability of the band structures in a great deal.

A similar trend can also be seen in the researches on photoelectrode materials. Since the discovery of Honda-Fujishima effect, there have been reported a great number of novel materials for photoelectrodes with a transition from simple compounds to complex compounds. For example, a group of typical semiconductors such as InP [30, 31], Si [32], GaP [33], and GaAs [34] have been used as photocathode materials after 1980's, while a kind of mixed cation compounds such as $CuIn_{0.7}Ga_{0.3}Se_2$ (CIGS) are now under investigation as highly effective novel photocathodes [35]. Additionally, Kaneko *et al.* very recently reported that the onset potential of CIGS will be greatly improved in a form of solid solution with ZnSe, and such solid solution is now considered as one of the most promising photocathode materials [5].

Accordingly, in the research field of both photocatalysts and photoelectrode systems, mixed

ion compounds such as oxynitrides, CIGS, and the solid solutions of them have been reported as promising candidates. The most advantageous feature of such compounds is, as previously mentioned, the broad range of controllability of their properties due to the huge variety of their structural features. Therefore, it is expected that such mixed ion compounds will be the central area of this research field in terms of searching, designing, and controlling the materials and their properties.

However, there is a huge barrier to investigate the structural and electronic features of these mixed ion compounds, since their complex structural features make it a challenging task to measure them microscopically or to relate them to their fundamental properties. For instance, the relative position of each ion is often incompletely understood in the materials where more than one cations or anions occupy identical sites such as solid solutions, although their ionic arrangements in the crystals should have strong effects on their properties. As another example, it is still impossible to identify the structures of point defects in solids experimentally with current technologies, although they often play critical roles, especially in semiconductors. Consequently, the relation between microscopic structural features and macroscopic properties in mixed ion compounds have not been fully understood yet, and thus the guidelines to control and enhance the properties of photocatalysts and photoelectrode materials consisting of such compounds are still under exploration.

1-4. Research objectives

In this research, I will tackle such issue by means of first principle calculations. In many cases, first principle calculations are quite suitable to clarify the relation between the structural factors and fundamental properties of a given material, since they are essentialy the methodologies for obtaining the electronic structures of a given system only from the structural imput information. In addition, it has become more feasible to adopt such calculations on large-scale systems owing to a remarkable progress in recent computational technologies. For instance, one can now calculate the electronic structures of the systems consisting of more than hundreds of atoms without any empirical parameters by using density functional theory (detailed in chapter 2), which is one of the most frequently used methods of first principle calculations.

Indeed, first principle calculations have already been used in the research area of photocatalyts. For instance, they are often used to identify the constituent orbitals in valence and conduction bands, or to specify whether their bandgaps are direct or indirect, by calculating the band structures and the DOS (Density of States) plots [36-38]. There also exist a number of examples where the fundamental properties such as carrier effective masses [39,40], band edge positions [41-43], defect formation energies[44-46], and defect levels of the materials [47,48] were theoretically obtained by analyzing the calculated band structures, electronic densities, or the total energies. Additionally, associated with the recent improvement in computational speeds, first principle calculations have also

been adopted to the material search for novel photocatalysts in forms of computational screening for more that thausands of candidate compounds [49-51]. Thus, first principle calculations are now becoming a powerful tool for the researches on photocatalyts and photoelectrode materials.

However, in spite of such progress and popularization of computational technologies, there have been only a few reports on first-principle calculations on mixed ion compounds, mainly due to the difficulties in modeling the structurals and performing the calculations. In many cases, it becomes a puzzling task to prepare the structural models of such compounds with mixed ions since the datails of the ionic arrangements in the crystals are not fully clarified. Furthermore, the structural models of such compounds need a large number of atoms (generally, a “supercell” generated by multiplying a unit cell of the compound is used in the structural modelling) to represent the complex arrangements of the ions in the crystals, and thus the calculation cost becomes significantly large compared to the calculations of simple oxides or pure solids.

Therefore, in this thesis, I challenged to develop appropriate structural models of mixed ion compounds, starting from the elucidations of the characteristics and origins of ionic arrangements, and to subsequently estimate their photocatalytst related properties from first principle, as illustrated in Figure 1-4. In the first half of the thesis, I dealt with rather simple oxynitrides to understand the physical origins and the effects of microscopic structural factors such as the specific arrangements of anions (anion orderings, in chapter 3) and the distortions of bond angles (octahedral-tiltings, in chapter

4). Then, in the second half, I tackled solid solutions like $LaMg_xTa_{1-x}O_{1+3x}N_{2-3x}$ (chapter 5) and $(ZnSe)_x(CuIn_{0.7}Ga_{0.3}Se_2)_{1-x}$ (chapter 6) in order to realize the modelization of more complex mixed ion compounds based on the insights obtained in the previous chapters. Furthermore, by clarifying the relation between the structural features and the fundamental properties in each compound, I aimed not only to give an explanation for the experimental trends, but also to provide the guidelines to control the properties and to enhance photocatalytic or photoelectrochemical activities for water splitting through structural modifications.

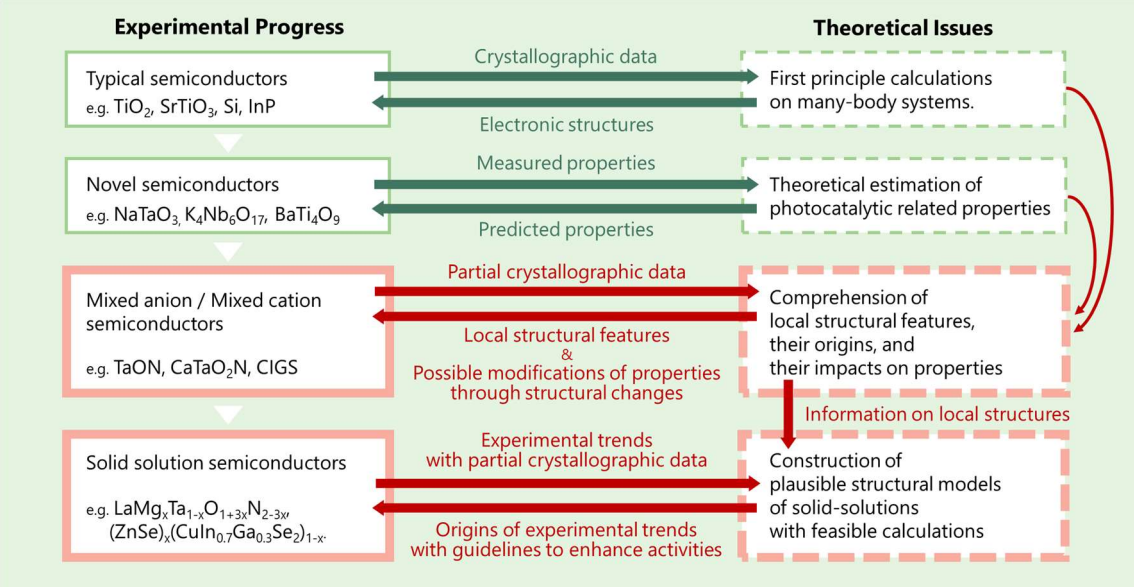

Figure 1-4. A schematic illustration of the research subjects of this thesis (red dotted frames) and their positions compared to the experimental progress and theoretical issues surrounding the research field of photocatalyst and photoelectrode materials.

Bibliography

[1] Kudo, A.; Miseki, Y. Heterogeneous photocatalyst materials for water splitting. *Chem. Soc. Rev.* **2009**, *38*, 253.

[2] Sorensen, B. Renewable energy: A technical overview. *Energy Policy* **1991**, *19*, 386.

[3] Nakamura, A.; Ota, Y.; Koike, K.; Hidaka, Y.; Nishioka, K.; Sugiyama, M.; Fujii. K. A 24.4% solar to hydrogen energy conversion efficiency by combining concentrator photovoltaic modules and electrochemical cells. *Appl. Phys. Express* **2015**, *8(10)*, 107101.

[4] Wang, Q.; Hisatomi, T.; Jia, Q.; Tokudome, H.; Zhong, M.; Wang, C.; Pan, Z.; Takata, T.; Nakabayashi, M.; Shibata, N.; Li, Y.; Sharp, I. D.; Kudo, A.; Yamada, T.; Domen, K. Scalable water splitting on particulate photocatalyst sheets with a solar-to-hydrogen energy conversion efficiency exceeding 1%. *Nat. Mater.* **2016**, *15*, 611.

[5] Kaneko, H.; Minegishi, T.; Nakabayashi, M.; Shibata, N.; Kuang, Y.; Yamada, T.; Domen K. A Novel Photocathode Material for Sunlight-Driven Overall Water Splitting: Solid Solution of ZnSe and $Cu(In,Ga)Se_2$. *Adv. Func. Mater.*, **2016**, *26*, 4570.

[6] Fujishima, A.; Honda K. Electrochemical photolysis of water at a semiconductor electrode. *Nature* **1972**, *238*, 37.

[7] Sato, S.; White J. M. Photodecomposition of water over Pt/TiO_2 catalysts. *Chem. Phys. Lett.* **1980**, *72*, 83.

[8] Domen, K.; Naito, S.; Soma, M.; Onishi, T.; Tamaru K. Photocatalytic decomposition of water vapour on an NiO–$SrTiO_3$ catalyst. *J. Chem. Soc.: Chem. Commun.* **1980**, *12*, 543.

[9] Kudo, A.; Tanaka, A.; Domen, K.; Maruya, K.; Aika K.; Onishi T. Photocatalytic decomposition of water over NiO-$K_4Nb_6O_{17}$ catalyst. *J. Catal.* **1988**, *111*, 67.

[10] Inoue, Y.; Niiyama, T.; Asai Y.; Sato K. Stable Photocatalytic Activity of $BaTi_40_9$ Combined with Ruthenium Oxide for Decomposition of Water. *J. Chem. Soc., Chem. Commun.***1992**, 579.

[11] Sayama, K.; Arakawa H. Effect of carbonate addition on the photocatalytic decomposition of liquid water over a ZrO_2 catalyst. *J. Photochem. Photobiol. A: Chem.* **1996**, *94*, 67.

[12] Kato, H.; Kudo A. Highly efficient decomposition of pure water into H_2 and O_2 over $NaTaO_3$ photocatalysts. *Catal. Lett.* **1999**, *58*, 153.

[13] Ikarashi, K.; Sato, J.; Kobayashi, H.; Saito, N.; Nishiyama, H.; Inoue Y. Photocatalysis for Water Decomposition by RuO_2-Dispersed $ZnGa_2O_4$ with d^{10} Configuration. *J. Phys. Chem. B,* **2002**, *106(35)*, 9048.

[14] Sato, J.; Saito, N.; Nishiyama, H.; Inoue Y. New Photocatalyst Group for Water Decomposition of RuO_2-Loaded p-Block Metal (In, Sn, and Sb) Oxides with d^{10} Configuration. *J. Phys. Chem. B*, **2001**, *105(26)*, 6061.

[15] Schulze, R. Recommendations for the integrated irradiance and the spectral distribution of simulated solar radiation for testing purposes. *Meteorologische Rundschau* **1970**, 23(2), 56. Cited in:

CIE Publication **1972**, *No.20 (TC-2.2)*.

[16] Hitoki, G.; Ishikawa, A.; Takata, T.; Kondo, J. N.; Hara M.; Domen K. Ta_3N_5 as a Novel Visible Light-Driven Photocatalyst (λ < 600nm). *Chem. Lett.*, **2002**, *(7)*, 736.

[17] Kasahara, A.; Nukumizu, K.; Hitoki, G.; Takata, T.; Kondo, J. N.; Hara, M.; Kobayashi, H.; Domen K. Photoreactions on $LaTiO_2N$ under Visible Light Irradiation. *J. Phys. Chem. A* **2002**, *106 (29)*, 6750.

[18] Hitoki, G.; Takata, T.; Kondo, J. N.; Hara, M.; Kobayashi, H.; Domen K. An oxynitride, TaON, as an efficient water oxidation photocatalyst under visible light irradiation (λ < 500nm). *Chem. Commun.* **2002**, *(16)*, 1698.

[18] Maeda, K.; Takata, T.; Hara, M.; Saito, N.; Inoue, Y.; Kobayashi, H.; Domen K. GaN:ZnO Solid Solution as a Photocatalyst for Visible-Light-Driven Overall Water Splitting. *J. Am. Chem. Soc.* **2005**, *127*, 8286.

[19] Yamasita, D.; Takata, T.; Hara, M.; Kondo, J. N.; Domen, K. Recent progress of visible-light-driven heterogeneous photocatalysts for overall water splitting. *Solid State Ionics* **2004**, *172*, 591.

[20] Lei, Z.; You, W.; Liu, M.; Zhou, G.; Takata, T.; Hara, M.; Domen, K.; Li, C. Photocatalytic water reduction under visible light on a novel $ZnIn_2S_4$ catalyst synthesized by hydrothermal method. *Chem.Commun.* **2003**, *0*, 2142.

[21] Ishikawa, A.; Takata, T.; Kondo, J. N.; Hara, M.; Kobayashi, H.; Domen, K. Oxysulfides Ln

$Ti_2S_2O_5$ as stable photocatalysts for water oxidation and reduction under visible-light irradiation. *J. Phys. Chem. B* **2004**, *108*, 2637.

[22] Maeda, K.; Domen, K. Oxynitride materials for solar water splitting. *MRS Bull.* **2011**, *36*, 25.

[23] Pan, C.; Takata, T.; Nakabayashi, M.; Matsumoto, T.; Shibata, N.; Ikuhara, Y.; Domen K. A Complex Perovskite-Type Oxynitride: The First Photocatalyst for Water Splitting Operable at up to 600 nm. *Angew. Chem. Int. Ed.* **2015**, *54*, 2955.

[24] Tsuji, I.; Kato, H.; Kudo A. Visible-Light-Induced H_2 Evolution from an Aqueous Solution Containing Sulfide and Sulfite over a ZnS–$CuInS_2$–$AgInS_2$ Solid-Solution Photocatalyst. *Angew. Chem. Int. Ed.* **2005**, *44(23)*, 3565.

[25] Quintans, C. S.; Kato, H.; Kobayashi, M.; Kaga, H.; Iwase, A.; Kudo, A.; Kakihana M. Improvement of hydrogen evolution under visible light over $Zn_{1-2x}(CuGa)_xGa_2S_4$ photocatalysts by synthesis utilizing a polymerizable complex method. *J. Mater. Chem. A* **2015**, *3*, 14239.

[26] Nandy, S.; Goto, Y.; Hisatomi, T.; Moriya, Y.; Minegishi, T.; Katayama, M.; Domen K. Synthesis and Photocatalytic Activity of $La_5Ti_2Cu(S_{1-x}Se_x)_5O_7$ Solid Solutions for H_2 Production under Visible Light Irradiation. *ChemPhotoChem* **2017**, *1(6)*, 265.

[27] Ueda, K.; Kato, H.; Kobayashi, M.; Hara, M.; Kakihana M. Control of valence band potential and photocatalytic properties of $Na_xLa_{1-x}TaO_{1+2x}N_{2-2x}$ oxynitride solid solutions. *J. Mater. Chem. A* **2013**, *1*, 3667.

[28] Pan, C.; Takata, T.; Kumamoto, K.; Ma, S. S. K.; Ueda, K.; Minegishi, T.; Nakabayashi, M.; Matsumoto, T.; Shibata, N.; Ikuhara, Y.; Domen K. Band engineering of perovskite-type transition metal oxynitrides for photocatalytic overall water splitting. *J. Mater. Chem. A*, **2016**, *4*, 4544.

[29] Takata, T.; Pan, C.; Domen K. Recent progress in oxynitride photocatalysts for visible-light-driven water splitting. *Sci. Technol. Adv. Mater.* **2015**, *16*, 033506.

[30] Heller, A.; Vadimsky, R. G. Efficient Solar to Chemical Conversion: 12% Efficient Photoassisted Electrolysis in the [p-type InP(Ru)]/HCl-KCl/Pt(Rh) Cell. *Phys. Rev. Lett.* **1981**, *46*, 1153.

[31] Aharon-Shalom, E.; Heller, A. Efficient p-InP (Rh-H alloy) and p-InP (Re-H alloy) Hydrogen Evolving Photocathodes. *J. Electrochem. Soc.* **1982**, *129*, 2865.

[32] Bookbinder, D. C.; Bruce, J. A.; Dominey, R. N.; Lewis, N. S.; Wrighton M. S. Synthesis and characterization of a photosensitive interface for hydrogen generation: Chemically modified p-type semiconducting silicon photocathodes. **1980**, *77(11)*, 6280.

[33] Nakato, Y.; Tonomura, S.; Tsubomura H. The catalytic effect of electrodeposited metals on the photo-reduction of water at p-type semiconductors. *Ber. Bunsenges. Phys. Chem.* **1976**, *80*, 1289.

[34] Gerischer, H.; Müller, N.; Haas O. On the mechanism of hydrogen evolution at GaAs electrodes. *J. Electroanal. Chem. Interfacial Electrochem.* **1981**, 119(1), 41.

[35] Kumagai, H.; Minegishi, T.; Sato, N.; Yamada, T.; Kubota, J.; Domen K. Efficient Solar Hydrogen Production from Neutral Electrolytes Using Surface-Modified Cu(In,Ga)Se_2 Photocahodes. *J. Mater.*

Chem. A **2015**, *3*, 8300.

[36] Liu, H.; Dong, H.; Meng, X.; Wu, F. First-principles study on strontium titanate for visible photocatalysis. *Chem. Phys. Lett.* **2013**, *555*, 141.

[37] Liu, P.; Nisar, J.; Pathak, B.; Ahuja, R. Hybrid density functional study on $SrTiO_3$ for visible light photocatalysis. *Int. J. Hydrog. Energy.* **2012**, *37*, 11611.

[38] Shi, W.-J.; Xiong, S.-J. Ab initio study on band-gap narrowing in $SrTiO_3$ with Nb-C-Nb cooping. *Phys. Rev. B* **2011**, *84*, 205210.

[39] Kehoe, A. B.; Scanlon, D. O.; Watson, G. W. The electronic structure of sulvanite structured semiconductors Cu_3MCh_4 (M = V, Nb, Ta; Ch = S, Se, Te): prospects for optoelectronic applications. *J.Mater. Chem. C* **2015**, *3*, 12236.

[40] Giorgi, G.; Fujisawa, J.-I.; Segawa, H.; Yamashita, K. Small Photocarrier Effective Masses Featuring Ambipolar Transport in Methylammonium Lead Iodide Perovskite: A Density Functional Analysis. *J. Phys. Chem. Lett.* **2013**, *4*, 4213.

[41] Toroker, M. C.; Kanan, D. K.; Alidoust, N.; Isseroff, L. Y.; Liao, P.; Carter, E. A. First principles scheme to evaluate band edge positions in potential transition metal oxide photocatalysts and photoelectrodes. *Phys. Chem. Chem. Phys.* **2011**, *13*, 16644.

[42] Huang, W. L. First-principles determination of the absolute band-edge positions of BiOX (X = F, Cl, Br, I). *Comput. Mater. Sci.* **2012**, *55*, 166.

[43] Zhou, Z.; Shi, J.; Wu, P.; Li, M.; Guo, L. First principles study on absolute band edge positions for II-VI semiconductors at (1 1 0) surface. *Chem. Phys. Lett.* **2011**, *513*, 72.

[44] Freysoldt, C.; Grabowski, B.; Hickel, T.; Neugebauer, J.; Kresse, G.; Janotti, A.; Van de Walle, C. G. First-principles calculations for point defects in solids. *Rev. Mod. Phys.* **2014**, *86*, 253.

[45] Persson, C.; Zhao, Y.-J.; Lany, S.; Zunger, A. n-type doping of $CuInSe_2$ and $CuGaSe_2$. *Phys. Rev. B* **2005**, *2*, 035211.

[46] Van de Walle, C. G.; Laks, D. B.; Neumark, G. F.; Pantelides, S. T. Solubilities, defect reactions and doping limits in ZnSe. *J. Crystal Growth* **1992**, *117*, 704.

[47] Janotti, A.; Varley, J. B.; Rinke, P.; Umezawa, N.; Kresse, G.; Van de Walle, C. G. Hybrid functional studies of the oxygen vacancy in TiO_2. *Phys. Rev. B* **2010**, *81*, 085212.

[48] Mattioli, G.; Alippi, P.; Filippone, F.; Caminiti, R.; Bonapasta, A. A. Deep versus Shallow Behavior of Intrinsic Defects in Rutile and Anatase TiO_2 Polymorphs. *J. Phys. Chem. C* **2010**, *114*, 21694.

[49] Castelli, I. E.; Olsen, T.; Datta, S. Landis, D. D.; Dahl, S.; Thygesen K. S.; Jacobsen, K. W. Computational screening of perovskite metal oxides for optimal solar light capture. *Energy Environ. Sci.* **2012**, *5*, 5814.

[50] Wu, Y.; Lazic, P.; Hautier, G.; Persson, K.; Ceder, G. First principles high throughput screening of oxynitrides for water-splitting photocatalysts. *Energy Environ. Sci*. **2013**, *6*, 157.

[51] Emery, A. A.; Wolverton, C. High-throughput DFT calculations of formation energy, stability and oxygen vacancy formation energy of ABO_3 perovskites. *Sci. Data* **2017**, 4, 170153.

Chapter 2.
First Principle Approaches to the Electronic Structure of Solids

2-1. Schrodinger equation and basic quantum mechanics

2-1-1. The particle and the wave nature of the electron

Since the discovery of Maxell equation, light is considered to be a kind of wave over a period of time. However, light was also revealed to be a kind of particle in the photon hypothesis [1] proposed by Einstein in 1905. Based on such insights, de Broglie substituted the speed of light $c = \nu\lambda$ (ν and λ represent the frequency and the wavelength of light, respectively) and the mass of light $m = 0$ for c and m in the equation that describes the mass-energy equivalence which was discovered by Einstein in the special relativity theory [2],

$$E = \sqrt{(pc)^2 + (mc^2)^2} \tag{2.1}$$

where p represents the momentum of the particle, and consequently obtained the following equation.

$$E = p\lambda\nu \tag{2.2}$$

Then, comparing this to an energy-frequency relation proved in the photon hypothesis,

$$E = h\nu \tag{2.3}$$

where h is Planck's constant, he derived the equation which is called de Broglie relation [3],

$$\lambda = \frac{h}{p} \tag{2.4}$$

where λ, which represents the wave nature, and p, which represents the particle nature, was proved to be related via Planck's constant. By this relation, it was also strongly indicated that electrons should have wave nature as well as particle nature, as in the case with the light, which was subsequently demonstrated by experiments.

Here, Eq (2.2) and Eq (2.3) can be deformed using the relations for the wave number k and angular momentum ω of the light,

$$k = \frac{2\pi}{\lambda} \tag{2.5}$$

$$\omega = 2\pi\nu \tag{2.6}$$

into the following relations,

$$E = \hbar\omega \tag{2.7}$$

$$p = \hbar k \tag{2.8}$$

where $\hbar$ is a Dirac constant, which equals Planck's constant h divided by 2π.

$$\hbar = \frac{h}{2\pi} \tag{2.9}$$

2-1-2. Schrödinger equation

2-1-2-1. Schrödinger equation of free electrons

Based on the insights from the de Broglie relation, electrons were also described using a wave function. The definition of a wave is a physical quantity which propagates spatially and temporally, and thus, a wave function is generally described as a function of time t and position x as follows,

$$\Psi(x,t) = A\sin(kx - \omega t) \tag{2.10}$$

or

$$\Psi(x,t) = A\cos(kx - \omega t) \tag{2.11}$$

where A represents the amplitude of the wave.

Here, Schrödinger [4] had expanded the wave function to the complex one,

$$\Psi(x,t) = A\exp\{i(kx - \omega t)\} \tag{2.12}$$

and subsequently derived the following wave function of electrons by substituting Eq (2.7) and Eq (2.8) for k and ω in Eq (2.12).

$$\Psi(x,t) = A\exp\left\{i(\frac{p}{\hbar}x - \frac{E}{\hbar}t)\right\} = A\exp\left(i\frac{p}{\hbar}x\right)\exp\left(-i\frac{E}{\hbar}t\right) \tag{2.13}$$

This formula can be deformed to

$$-\frac{\hbar^2}{2m}\frac{\partial^2\Psi(x,t)}{\partial x^2} = \frac{p^2}{2m}\Psi(x,t) \tag{2.14}$$

using its second order derivative with respect to x with its both sides multiplied by $-\hbar^2/2m$.

On the other hand, Eq (2.13) can also be deformed to

$$i\hbar\frac{\partial\Psi(x,t)}{\partial t} = E\Psi(x,t) \tag{2.15}$$

using its first order derivative with respect to t with its both sides multiplied by $i\hbar$. Here, Since the momentum p and the energy E are related by

$$E = \frac{p^2}{2m} \tag{2.16}$$

the right sides of Eq (2.14) and Eq (2.15) are equal. Thus, an equation

$$i\hbar\frac{\partial\Psi(x,t)}{\partial t} = -\frac{\hbar^2}{2m}\frac{\partial^2\Psi(x,t)}{\partial x^2} \tag{2.17}$$

can be derived, which is called a Schrödinger equation for a one-dimensional free electron.

From Eq (2.14) and Eq (2.15), one can obtain the following relations between the physical quantities and the operators,

$$E \rightarrow i\hbar\frac{\partial}{\partial t} \tag{2.18}$$

$$p \rightarrow -i\hbar\frac{\partial}{\partial x} \tag{2.19}$$

Additionally, one can also obtain the Schrödinger equation for a three-dimensional free electron, by substituting the variable x with a three-dimensional positional vector $\boldsymbol{r} = (x, y, z)$, and the variable p with a three-dimensional momentum vector $\boldsymbol{p} = (p_x, p_y, p_z)$. Since according to Eq (2.19) each element in the momentum vector can be related to the corresponding operator as follows,

$$p_x \rightarrow -i\hbar\frac{\partial}{\partial x} \tag{2.20}$$

$$p_y \rightarrow -i\hbar\frac{\partial}{\partial y} \tag{2.21}$$

$$p_z \rightarrow -i\hbar\frac{\partial}{\partial z} \tag{2.22}$$

the Schrödinger equation for a three-dimensional free electron can be written as,

$$i\hbar\frac{\partial\Psi(\boldsymbol{r},t)}{\partial t} = -\frac{\hbar^2}{2m}\left(\frac{\partial^2}{\partial x^2}+\frac{\partial^2}{\partial y^2}+\frac{\partial^2}{\partial z^2}\right)\Psi(\boldsymbol{r},t) = -\frac{\hbar^2}{2m}\nabla^2\Psi(\boldsymbol{r},t) \tag{2.23}$$

and the wave functions of free electrons in the three-dimensional space can be obtained by solving this equation.

Here, it is widely considered that the wave functions represent the existence probability of the particles, as proposed in Born's rule [5], where the probability density function for the observation of the particle at a position $\boldsymbol{r}$ at a time t, $P(\boldsymbol{r},t)$, will be given by

$$P(\boldsymbol{r},t) = |\Psi(\boldsymbol{r},t)|^2 \tag{2.24}$$

2-1-2-2. Schrödinger equation of electrons in external potential

In the previous section, the Schrödinger equation for a three-dimensional free electron was derived. However, the electrons in real atoms, molecules, and crystals usually move in the potential fields generated by the atomic nuclei and the other electrons. Therefore, in this section, the Schrödinger equation for the electrons in a certain potential $V(\boldsymbol{r},t)$ will be derived. Such Schrödinger equation can be obtained by adding a potential energy term $V(\boldsymbol{r},t)$ to the kinetic energy operator in Eq (2.23).

$$i\hbar\frac{\partial\Psi(\boldsymbol{r},t)}{\partial t} = \left\{-\frac{\hbar^2}{2m}\nabla^2 + V(\boldsymbol{r},t)\right\}\Psi(\boldsymbol{r},t) \tag{2.25}$$

Here, the operators in the right side are called Hamiltonian, since it corresponds to the Hamiltonian

function ($H = T + V$, where T and V are the kinetic and the potential energy, respectively) that appears in classical analytical mechanics.

$$H(\boldsymbol{r}, t) = -\frac{\hbar^2}{2m}\nabla^2 + V(\boldsymbol{r}, t) \tag{2.26}$$

Using this term, the Schrödinger equation can be rewritten as,

$$i\hbar\frac{\partial\Psi(\boldsymbol{r}, t)}{\partial t} = H(\boldsymbol{r}, t)\Psi(\boldsymbol{r}, t) \tag{2.27}$$

2-1-2-3. Time-independent Schrödinger equation

In Eq (2.25), the external potential was considered as a function of time t and position $\boldsymbol{r}$. However, the potentials generated in real substances are usually independent on the time in their equilibrium state. Therefore, in this section, the Schrödinger equation for the electron which moves in the time-independent potential $V(\boldsymbol{r})$ will be derived.

Here, the wave function of the electron is described as a product between its spatial part $\psi(\boldsymbol{r})$ and temporary part $f(t)$.

$$\Psi(\boldsymbol{r}, t) = \psi(\boldsymbol{r})f(t) \tag{2.28}$$

Then, by plugging this wave function $\Psi(\boldsymbol{r}, t)$ and the potential $V(\boldsymbol{r})$ in the Schrödinger equation described in Eq (2.25), one will obtain the deformed equation where the variables $\boldsymbol{r}$ and t are separated.

$$\frac{i\hbar}{f(t)}\frac{df(t)}{dt} = \frac{1}{\psi(\boldsymbol{r})}\left\{-\frac{\hbar^2}{2m}\nabla^2\psi(\boldsymbol{r}) + V(\boldsymbol{r})\psi(\boldsymbol{r})\right\} = const. \tag{2.29}$$

By rewriting the constant as E', the equation,

$$i\hbar\frac{df(t)}{dt} = E'f(t) \tag{2.30}$$

will be derived from the left side, and the temporary part of the wave function,

$$f(t) = C\exp\left(-\frac{iE't}{\hbar}\right) \tag{2.31}$$

will be obtained as the solution of the equation Eq (2.30). Further, by comparing Eq (2.31) to the temporary part of Eq (2.13),

$$\exp\left(-i\frac{E}{\hbar}t\right) \tag{2.32}$$

one can easily notice that the constant E' indeed corresponds to the energy E.

On the other hand, the equation for the spatial part of the wave function

$$\left\{-\frac{\hbar^2}{2m}\nabla^2 + V(\boldsymbol{r})\right\}\psi(\boldsymbol{r}) = E'\psi(\boldsymbol{r}) \tag{2.33}$$

will be obtained from the right hand of Eq (2.29). This can be rewritten also using $E' = E$ and the expression for the Hamiltonian Eq (2.26) to

$$H(\boldsymbol{r})\psi(\boldsymbol{r}) = E\psi(\boldsymbol{r}) \tag{2.34}$$

which is called a time-independent Schrödinger equation. The wave functions of the electrons in the time-independent potentials such as those in atoms or molecules can be obtained from solving Eq (2.34). Here, the total energy of the system,E, will be given as an eigenvalue of this differential equation, which can be obtained as an expectation of the Hamiltonian as follows,

$$E = \int d\tau\, \psi^* H\psi \left(= \int d\tau\, \psi^* E\psi = E\int d\tau\, \psi^*\psi\right) \tag{2.35}$$

where ψ^* is a complex conjugate of ψ. Besides, it has also been proved that the eigen functions of the Schrödinger equation are orthogonal to each other as described in Eq (2.36),

$$\int d\tau \, {\psi_i}^* \psi_j = \delta_{i,j} \tag{2.36}$$

given that all the wave functions above are normalized,

$$\int d\tau \, \psi^* \psi = 1 \tag{2.37}$$

and the wave functions that satisfy both Eq (2.36) and Eq (2.37) are generally called orthonormal functions.

Hereafter, the frequently used integrals like Eq (2.35) and Eq (2.36) will be described using Dirac's notation as Eq (2.38) and Eq (2.39) for the simplicity.

$$\int d\tau \, \psi^* H \psi \equiv \langle \psi | H | \psi \rangle \tag{2.38}$$

$$\int d\tau \, \psi^* \psi \equiv \langle \psi | \psi \rangle \tag{2.39}$$

2-1-3. Variational principle

The wave function ψ_0, which corresponds to the minimum eigen value E_0 of the Hamiltonian, is called the wave function of the ground state. And here, it has been proved that any expected value of energy of the Hamiltonian for the arbitrary wave function ψ cannot be lower than E_0, as described Eq (2.40), which is called a variational principle.

$$E_0 = \langle\psi_0|H|\psi_0\rangle \leq \langle\psi|H|\psi\rangle = E \tag{2.40}$$

According the variational principle, one can obtain the eigen value and the eigen function of the ground state for the Schrödinger equation by minimizing the energy expectation Eq (2.35) under the normalization condition Eq (2.37). This can be achieved by using Lagrange's method of undetermined multipliers where the value I,

$$I \equiv \langle\psi_0|H|\psi_0\rangle - \langle\psi|\psi\rangle \tag{2.41}$$

is minimized with respect to ψ.

2-2. Hartree-Fock Approximation

2-2-1. Schrödinger equation for many body systems

Using the Schrödinger equations introduced in the previous section, in principle, one can obtain the wave functions of the electrons moving in the potentials generated by the atomic nuclei of molecules and solids. In other words, the electronic densities and total energies of any substances can be obtained by solving such Schrödinger equation. Here, the Hamiltonian for a system with more than one electrons can be described as Eq (2.42) (note that the atomic units are used hereafter),

$$H(\boldsymbol{r}) = \sum_{i=1}^{N}\left\{-\frac{1}{2}\nabla_i^2\right\} + \sum_{i=1}^{N}\left\{\sum_{i=1}^{N}\sum_{A=1}^{M} V_{Ne}(\boldsymbol{r_{iA}})\right\} + \frac{1}{2}\sum_{i,j}^{N} V_{ee}(\boldsymbol{r_i}, \boldsymbol{r_j}) \qquad (2.42)$$

where each term corresponds to the sum of the kinetic energy of each electron, the sum of the potential energies between each electron and atomic nucleus, and the sum of the potential energies between two different electrons. The detailed formulation of each potential in Eq (2.42) is as follows,

$$V_{Ne}(\boldsymbol{r_{iA}}) = -\frac{Z_A}{|\boldsymbol{r_{iA}}|} \qquad (2.43)$$

$$V_{ee}(\boldsymbol{r_i}, \boldsymbol{r_j}) = \frac{1}{|\boldsymbol{r_i} - \boldsymbol{r_j}|} \qquad (2.44)$$

However, it has been known that the Schrödinger equations for more than three electrons cannot be solved analytically (three-body problem). Therefore, to get the electronic structures of the real substances, one need to apply some approximation.

2-2-2. Hartree approximation using one-electron wavefunction

Thus, the Hartree approximation, where the many-electron wavefunction $\Psi(\boldsymbol{r_1}, \boldsymbol{r_2}, \dots, \boldsymbol{r_N})$ is described as a product of the one-electron wavefunctions $\psi_i(\boldsymbol{r_i})(i = 1, 2, \dots, \mathrm{N})$, had been proposed [6-8].

$$\Psi(\boldsymbol{r_1}, \boldsymbol{r_2}, \dots, \boldsymbol{r_N}) = \psi_1(\boldsymbol{r_1})\psi_2(\boldsymbol{r_2}) \dots \psi_N(\boldsymbol{r_N}) \tag{2.45}$$

Additionally, the term corresponding to the potential energies between the electrons in the Hamiltonian Eq (2.42) was approximated to the set of effective potentials $V_{eff}(\boldsymbol{r_i})$, where the interactions between each electron were ignored, and alternatively it was assumed that each electron moves in the averaged potential field generated by the other electrons, as follows.

$$V_{eff}(\boldsymbol{r_i}) = \sum_{j \neq i} \int \boldsymbol{d}^3\boldsymbol{r}_j \frac{|\psi_j(\boldsymbol{r_j})|^2}{|\boldsymbol{r_i} - \boldsymbol{r_j}|} \tag{2.46}$$

Due to such approximation, the many-electron Hamiltonian Eq (2.42) can be rewritten as a summation of Hamiltonians for each single electron,

$$H(\boldsymbol{r}) = -\sum_{i=1}^{N} \frac{1}{2}\nabla_i^2 + \sum_{i=1}^{N}\sum_{A=1}^{M} V_{Ne}(\boldsymbol{r_{iA}}) + \sum_{i=1}^{N} V_{eff}(\boldsymbol{r_i}) = \sum_{i=1}^{N} h(\boldsymbol{r_i}) \tag{2.47}$$

where,

$$h(\boldsymbol{r_i}) = \frac{1}{2}\nabla_i^2 + V_{Ne}(\boldsymbol{r_{iA}}) + V_{eff}(\boldsymbol{r_i}) \tag{2.48}$$

Here, one can obtain the energy expectation E of the Hamiltonian in Eq (2.47) with the approximated wave function Eq (2.45) as Eq (2.49), according to the orthonormal condition of each one-electron wave function $\psi_i(\boldsymbol{r_i})$.

$$E = \langle \Psi | H | \Psi \rangle = \sum_{i=1}^{N} \langle \psi_i | h | \psi_i \rangle \tag{2.49}$$

Subsequently, by adopting the variational principle, the set of one-elecron wave functions that minimizes the above expectation value will be obtained as the solutions of the following one-electron equations.

$$h(\boldsymbol{r_i})\psi_i(\boldsymbol{r_i}) = \varepsilon_i \psi_i(\boldsymbol{r_i}) \tag{2.50}$$

Then, since the Schrödinger equations for the whole system can be deformed as

$$H(\boldsymbol{r})\, \Psi(\boldsymbol{r_1}, \boldsymbol{r_2}, \dots, \boldsymbol{r_N}) = \sum_{i}^{N} h(\boldsymbol{r_i})\, \psi_1(\boldsymbol{r_1})\psi_2(\boldsymbol{r_2}) \dots \psi_N(\boldsymbol{r_N})$$
$$= \sum_{i}^{N} \varepsilon_i\, \psi_1(\boldsymbol{r_1})\psi_2(\boldsymbol{r_2}) \dots \psi_N(\boldsymbol{r_N}) = E\Psi(\boldsymbol{r_1}, \boldsymbol{r_2}, \dots, \boldsymbol{r_N}) \tag{2.51}$$

the total energy E cam be obtained as the sum of each eigenvalue of Eq (2.50).

$$E = \sum_{i}^{N} \varepsilon_i \tag{2.52}$$

2-2-3. Hartree-Fock approximation using Slater determinant

Nevertheless, there still remains a critical problem in the Hartree approximation described in the previous section – the antisymmetricity, that is, the sign reversal of the wave function associated with a permutation of two electrons Eq (2.53), had not been included in the approximation.

$$\Psi(\boldsymbol{r_1}, \boldsymbol{r_2}, \dots, \boldsymbol{r_i}, \dots, \boldsymbol{r_j}, \dots, \boldsymbol{r_N}) = -\Psi(\boldsymbol{r_1}, \boldsymbol{r_2}, \dots, \boldsymbol{r_j}, \dots, \boldsymbol{r_i}, \dots, \boldsymbol{r_N}) \tag{2.53}$$

Hence, Slater proposed to describe a multi-electron wave function using a determinant whose elements consist of one-electron wave functions [9],

$$\Psi(\boldsymbol{\xi_1}, \boldsymbol{\xi_2}, \dots, \boldsymbol{\xi_N}) = \frac{1}{N!}\begin{vmatrix} \chi_1(\boldsymbol{\xi_1}) & \cdots & \chi_1(\boldsymbol{\xi_N}) \\ \vdots & \ddots & \vdots \\ \chi_N(\boldsymbol{\xi_1}) & \cdots & \chi_N(\boldsymbol{\xi_N}) \end{vmatrix}$$

$$\equiv \frac{1}{N!}\det\{\chi_1(\boldsymbol{\xi_1}), \dots, \chi_N(\boldsymbol{\xi_N})\} \tag{2.54}$$

where

$$\chi_i(\boldsymbol{\xi_i}) = \psi_i(\boldsymbol{r_i})\alpha(\sigma) \tag{2.55}$$

Here, the antisymmetricity of the electrons are inherently described due the basic characteristics of determinants. Note that each one-electron wave function was described as a product of a spatial orbital $\psi_i(\boldsymbol{r_i})$ and a spin orbital $\alpha(\sigma)$ with spin coordinates $\boldsymbol{\xi_j}$, so that the difference in the interactions depending on spins will be taken into account.

Then, the many-body Hamiltonian in Eq (2.42) was divided into two parts, one for the single-electron operators, and the other for the two-electron operators.

$$H(\boldsymbol{r}) = \sum_{i=1}^{N}\left\{-\frac{1}{2}\nabla_i^2 + \sum_{A=1}^{M} V_{Ne}(\boldsymbol{r_{iA}})\right\} + \frac{1}{2}\sum_{i,j}^{N} V_{ee}(\boldsymbol{r_i}, \boldsymbol{r_j})$$

$$= \sum_{i=1}^{N} h(\boldsymbol{r_i}) + \frac{1}{2}\sum_{i,j}^{N} V_{ee}(\boldsymbol{r_i}, \boldsymbol{r_j}) \tag{2.56}$$

where,

$$h(\boldsymbol{r_i}) \equiv -\frac{1}{2}\nabla_i^2 + \sum_{A=1}^{M} V_{Ne}(\boldsymbol{r_{iA}}) \tag{2.57}$$

Subsequently, the energy expectation will be obtained using the Slater determinant Eq (2.54) and the Hamiltonian Eq (2.56) as follows,

$$E = \langle \Psi | H | \Psi \rangle$$

$$= \sum_{i=1}^{N} \langle \chi_i | h | \chi_i \rangle + \frac{1}{2}\langle \chi_i \chi_j | V_{ee}(\boldsymbol{r_i}, \boldsymbol{r_j}) | \chi_i \chi_j \rangle - \frac{1}{2}\langle \chi_i \chi_j | V_{ee}(\boldsymbol{r_i}, \boldsymbol{r_j}) | \chi_j \chi_i \rangle \tag{2.58}$$

Finally, by adopting the variational principle for Eq (2.58) with Lagrange's method of undetermined multipliers as Eq (2.40), the set of one-electron wave functions $\{\chi_i(\boldsymbol{\xi_i})\}$ that minimizes the energy expectation will be obtained as the solutions of the following equations,

$$h(\boldsymbol{r_i})\chi_i(\boldsymbol{\xi_i}) + \sum_{j=1}^{N} \int d\xi_j \chi_j^*(\boldsymbol{\xi_j}) V_{ee}(\boldsymbol{r_i}, \boldsymbol{r_j}) \chi_j(\boldsymbol{\xi_j})\, \chi_i(\boldsymbol{\xi_i})$$

$$-\sum_{j=1}^{N} \int d\xi_j \chi_j^*(\boldsymbol{\xi_j}) V_{ee}(\boldsymbol{r_i}, \boldsymbol{r_j}) \chi_i(\boldsymbol{\xi_j}) \chi_j(\boldsymbol{\xi_i}) = \varepsilon_i \chi_i(\boldsymbol{\xi_i}) \tag{2.59}$$

which can also be deformed to the equation for the set of one-electron orbitals $\psi_i(\boldsymbol{r_i})$ by eliminating the spin orbitals $\alpha(\sigma)$ by integrating Eq (2.59) with respect to σ in accordance with the orthonormal condition. Thus, one will obtain

$$h(\boldsymbol{r_i})\psi_i(\boldsymbol{r_i}) + \sum_{j=1}^{N} \int d\boldsymbol{r_j} \psi_j^*(\boldsymbol{r_j}) V_{ee}(\boldsymbol{r_i}, \boldsymbol{r_j}) \psi_j(\boldsymbol{r_j})\, \psi_i(\boldsymbol{r_i})$$

$$- \sum_{j=1}^{N} \int d\boldsymbol{r_j} \psi_j^*(\boldsymbol{r_j}) V_{ee}(\boldsymbol{r_i}, \boldsymbol{r_j}) \psi_i(\boldsymbol{r_j}) \psi_j(\boldsymbol{r_i}) = \varepsilon_i \psi_i(\boldsymbol{r_i}) \tag{2.60}$$

where the third term only accounts for the electrons with parallel spins.

Here, Eq (2.60) can be rewritten by using the operators $J_j(\boldsymbol{r_i})$ and $K_j(\boldsymbol{r_i})$ defined as,

$$\int d\boldsymbol{r_j} \psi_j^*(\boldsymbol{r_j}) V_{ee}(\boldsymbol{r_i}, \boldsymbol{r_j}) \psi_j(\boldsymbol{r_j})\, \psi_i(\boldsymbol{r_i}) \equiv J_j(\boldsymbol{r_i}) \psi_i(\boldsymbol{r_i}) \tag{2.61}$$

$$\int d\boldsymbol{r_j} \psi_j^*(\boldsymbol{r_j}) V_{ee}(\boldsymbol{r_i}, \boldsymbol{r_j}) \psi_i(\boldsymbol{r_j}) \psi_j(\boldsymbol{r_i}) \equiv K_j(\boldsymbol{r_i}) \psi_i(\boldsymbol{r_i}) \tag{2.62}$$

to

$$F(\boldsymbol{r_i})\psi_i(\boldsymbol{r_i}) = \varepsilon_i \psi_i(\boldsymbol{r_i}) \tag{2.63}$$

where

$$F(\boldsymbol{r_i}) = h(\boldsymbol{r_i}) + \sum_{j=1}^{N} J_j(\boldsymbol{r_i}) - \sum_{j=1}^{N} K_j(\boldsymbol{r_i}) \tag{2.64}$$

like one-electron equations derived in the Hartree approximation in the previous section. Eq (2.63) is called a Hartree-Fock equation [10], and the wave function and the energy of a many-electron system can be obtained by solving this equation.

It should be noted that $J_j(\boldsymbol{r_i})$ corresponds to the electrostatic potential between the electrons according to the analogy with the potential term appeared in the Hartree approximation in Eq (2.46). On the other hand, $K_j(\boldsymbol{r_i})$ corresponds to a quantum mechanical interaction between the electrons with parallel spins that arises from the Pauli exclusion principle. $K_j(\boldsymbol{r_i})$ is widely called an

exchange potential, and is always negative since the electrostatic repulsion between the two electrons with parallel spins will be reduced due the Pauli repulsion.

2-3. Density Functional Theory

2-3-1. The Thomas-Fermi approximations

As explained in the previous section, the procedure to obtain the many-electron wave function using a set of differential equations for one-electron wave functions had been established as Hartree-Fock approximation. Nevertheless, it still remains a laborious task to perform such procedure, since the integral terms involving the operators defined in Eq (2.61) and Eq (2.62) include two orbitals for different electrons (= two-electron integral), and thus the computational cost gets significantly expensive. Hence, Hartree-Fock approximation is not suitable to a system that contains a large number of electrons, such as solids.

Therefore, unlike with Hartree-Fock approximation, there had been proposed another method to obtain the electronic structure of a many-electron system, by formulating its Hamiltonian using the potentials that are described as the functionals of its electron density n. Consequently, Thomas and Fermi had derived the kinetic energy term as a functional of the electron density n using homogeneous electron gas model [11,12].

$$T^{TF}[n] = \frac{3}{10}(3\pi^2)^{2/3}\int d^3\boldsymbol{r} n(\boldsymbol{r})^{\frac{5}{3}} \tag{2.65}$$

Additionally, they had also described the electrostatic interaction term as the functional of the electron density in accordance with classical electromagnetics, and obtained the energy functional as follows,

$$E^{TF}[n]$$

$$= \frac{3}{10}(3\pi^2)^{2/3}\int d^3\boldsymbol{r} n(\boldsymbol{r})^{\frac{5}{3}} + \int d^3\boldsymbol{r} V_{ext}(\boldsymbol{r})n(\boldsymbol{r}) + \frac{1}{2}\int d^3\boldsymbol{r} d^3\boldsymbol{r}' \frac{n(\boldsymbol{r})n(\boldsymbol{r}')}{|\boldsymbol{r}-\boldsymbol{r}'|} \quad (2.66)$$

where the second and the third term corresponds to the electron-nuclei interaction and the electron-electron interaction, respectively.

Afterward, Dirac had also derived the functional for the exchange energy, which had been originally discovered in Hartree-Fock approximation, using homogeneous electron gas model [13].

$$E_X^D[n] = -\frac{3}{4}\left(\frac{3}{\pi}\right)^{\frac{1}{3}}\int d^3\boldsymbol{r} n(\boldsymbol{r})^{\frac{4}{3}} \quad (2.67)$$

This functional is called a local density approximation (LDA) functional, since it only depends on the local electron density. This is indeed the only form of the exact LDA exchange functional.

On the other hand, Weizsäcker had proposed the correction term of kinetic energy as the functional of both electron density n and its gradient ∇n [14].

$$T^W[n, \nabla n] = \frac{1}{8}\int d^3\boldsymbol{r} \frac{|\nabla n(\boldsymbol{r})|^2}{n(\boldsymbol{r})} \quad (2.68)$$

This functional is considered as the first generalized gradient approximation (GGA) functional, which is explained in the later section.

Finally, the total energy and the electron density of a many-electron system in its ground state will be obtained by minimizing the energy functional with respect to n, within the constraint of

$$\int d^3\boldsymbol{r} n(\boldsymbol{r}) = N \quad (2.69)$$

where the number of the electrons must be a constant. Here, since the energy functional only takes the

electron density n, which is a function of only three variables, as its argument, one can perform the calculation with less computational cost compared to Hartree-Fock approximation where the two-electron integrals have been involved.

2-3-2. The Hohenberg-Kohn Theorems

Despite the groundbreaking idea proposed in the previous section, there still remained a critical issue to apply such method to the calculations of electronic structures – the validity of describing the energy as the functional of the electron density had not been theoretically confirmed.

To solve such issue, Hohenberg and Kohn had theoretically proved the existence of the energy functional of electron density, by disclosing the relationship between the electron density and the external potential. To be more precise, they had proved the following two theorems as the Hohenberg-Kohn theorems [15].

Theorem 1. The external potential $V(\boldsymbol{r})_{ext}$ of a system can be uniquely specified by its ground-state electron density.

Theorem 2. The exact ground-state electron density gives the global minimum of the energy functional.

The proof of each theorem is described below.

The proof of theorem 1:

Suppose that there exist two distinct Hamiltonians $H^{(1)}$ and $H^{(2)}$ whose external

potentials $V(\boldsymbol{r})_{ext}^{(1)}$ and $V(\boldsymbol{r})_{ext}^{(2)}$ differ by more than a constant, while giving the same electron density $n_0(\boldsymbol{r})$. Here, the difference between the two Hamiltonians can be written as,

$$H^{(1)} - H^{(2)} = V(\boldsymbol{r})_{ext}^{(1)} - V(\boldsymbol{r})_{ext}^{(2)} \tag{2.70}$$

Then, given that $\Psi^{(1)}$ and $\Psi^{(2)}$ are the ground-state wave functions of $H^{(1)}$ and $H^{(2)}$, respectively, the following inequality holds according to the variational principle (see section 2-1-3).

$$E^{(1)} = \langle \Psi^{(1)} | H^{(1)} | \Psi^{(1)} \rangle < \langle \Psi^{(2)} | H^{(1)} | \Psi^{(2)} \rangle \tag{2.71}$$

Now, since the last term can be deformed as

$$\begin{aligned} \langle \Psi^{(2)} | H^{(1)} | \Psi^{(2)} \rangle &= \langle \Psi^{(2)} | H^{(2)} | \Psi^{(2)} \rangle + \int d^3\boldsymbol{r} \left[V(\boldsymbol{r})_{ext}^{(1)} - V(\boldsymbol{r})_{ext}^{(2)} \right] n_0(\boldsymbol{r}) \\ &= E^{(2)} + \int d^3\boldsymbol{r} \left[V(\boldsymbol{r})_{ext}^{(1)} - V(\boldsymbol{r})_{ext}^{(2)} \right] n_0(\boldsymbol{r}) \end{aligned} \tag{2.72}$$

the inequality Eq (2.71) can be rewritten as

$$E^{(1)} < E^{(2)} + \int d^3\boldsymbol{r} \left[V(\boldsymbol{r})_{ext}^{(1)} - V(\boldsymbol{r})_{ext}^{(2)} \right] n_0(\boldsymbol{r}) \tag{2.73}$$

In a similar way, the following inequality

$$E^{(2)} < E^{(1)} - \int d^3\boldsymbol{r} \left[V(\boldsymbol{r})_{ext}^{(1)} - V(\boldsymbol{r})_{ext}^{(2)} \right] n_0(\boldsymbol{r}) \tag{2.74}$$

can also be obtained. However, by adding Eq (2.73) and Eq (2.74), a contradicting inequality

$$E^{(1)} + E^{(2)} < E^{(1)} + E^{(2)} \tag{2.75}$$

will be obtained. This proves that there is a false in the initial assumption, where the two distinct external potentials differing by more than a constant give the same ground-state electron density $n_0(\boldsymbol{r})$. In other words, by *reductio ad absurdum*, the theorem 1 has been proven.

The proof of theorem 2:

Suppose that the total energy of any system can be described as $E^{HK}[n]$, which is a functional of the electron density. Also, suppose that the ground-state electron density which corresponds to the external potential $V_{ext}(\boldsymbol{r})$ is given by $n^{(1)}$, and any other different electron density is given by $n^{(2)}$. Here, $E^{HK}[n^{(1)}]$ is equal to the expectation value of the Hamiltonian $H^{(1)}$ that corresponds to $V_{ext}(\boldsymbol{r})$ with its ground-state wave function $\Psi^{(1)}$, as described as,

$$E^{HK}[n^{(1)}] = \langle \Psi^{(1)} | H^{(1)} | \Psi^{(1)} \rangle \tag{2.76}$$

On the other hand, $E^{HK}[n^{(2)}]$ is equal to the expectation value of the same Hamiltonian with the wave function $\Psi^{(2)}$ that corresponds to $n^{(2)}$.

$$E^{HK}[n^{(2)}] = \langle \Psi^{(2)} | H^{(1)} | \Psi^{(2)} \rangle \tag{2.77}$$

Now, according to the variational principle, the following inequality holds between Eq(2.76) and Eq(2.77).

$$E^{HK}[n^{(1)}] = \langle \Psi^{(1)} | H^{(1)} | \Psi^{(1)} \rangle < \langle \Psi^{(2)} | H^{(1)} | \Psi^{(2)} \rangle = E^{HK}[n^{(2)}] \tag{2.78}$$

Thus, the energy functional has been proven to be variational to the electron density.

Here, it should be noted that the Hamiltonian of a system can be fully formulated when its external potential was identified, and thus the wave functions of the system can also be fully obtained. Therefore, the theorem 1 has proved that the property of the system can be described as the functional

of the ground-state electron density $n_0(\boldsymbol{r})$ since the density uniquely specifies the external potential of the system. Additionally, by theorem 2, it has also been proved that one can obtain the energy and the electron density of the ground-state by minimizing the energy functional with respect to $n(\boldsymbol{r})$ due to the variational principle.

2-3-3. The Kohn-Sham equations

By the Hohenberg-Kohn theorems introduced in the previous section, the validity of describing the energy of many-electron system as functional of electron density had been proven. Nevertheless, the specific formulation of the energy functional had not been given in those theoretical frameworks, and thus the procedures to obtain the energy and electron density of the ground-state of a system had not been established.

Hence, Kohn and Sham subsequently derived the formulations to obtain the ground-state energy and the electron density of many-electron systems based on the Hohenberg-Kohn theorems [16]. First, they assumed an auxiliary system consisting of N non-interacting electrons, instead of the real N-electron system where the electrons interact to each other [16]. It was supposed that the electron density of the auxiliary system is exactly the same as that of the interacting system. Here, the Hamiltonian for the independent electrons in the auxiliary system can be written as,

$$H_{aux}^{\sigma} = -\frac{1}{2}\nabla^2 + V^{\sigma}(\boldsymbol{r}) \tag{2.79}$$

where the first and the second term corresponds to the kinetic and the potential energy of each electron, respectively, and the index σ corresponds to its spin. Then, the set of wave functions of such auxiliary system $\{\psi_{\mathrm{i}}^{\sigma}(\boldsymbol{r})\}$ was given as the ground-state wave functions of this one-electron Hamiltonian, and thus the electron density of the system was given as,

$$n(\boldsymbol{r}) = \sum_{\sigma} n^{\sigma}(\boldsymbol{r}) = \frac{1}{2}\sum_{\sigma}\sum_{i=1}^{N^{\sigma}} |\psi_i^{\sigma}(\boldsymbol{r})|^2 \tag{2.80}$$

where the index i runs over the number of electrons.

Subsequently, Kohn and Sham formulated the total kinetic energy of the auxiliary system using the set of its wave functions $\{\psi_i^\sigma(\boldsymbol{r})\}$ as follows,

$$T_s = -\frac{1}{2}\sum_\sigma \sum_{i=1}^{N^\sigma} \langle \psi_i^\sigma(\boldsymbol{r})|\nabla^2|\psi_i^\sigma(\boldsymbol{r})\rangle = -\frac{1}{2}\sum_\sigma \sum_{i=1}^{N^\sigma} \int d^3\boldsymbol{r}|\nabla\psi_i^\sigma(\boldsymbol{r})|^2 \qquad (2.81)$$

while the electrostatic interactions were described using the electron density defined in Eq (2.80), as

$$E_{ee}[n] = \frac{1}{2}\int\int d^3\boldsymbol{r}d^3\boldsymbol{r}'\frac{n(\boldsymbol{r})n(\boldsymbol{r}')}{|\boldsymbol{r}-\boldsymbol{r}'|} \qquad (2.82)$$

for the electron-electron interactions, and as

$$E_{Ne}[n] = \int d^3\boldsymbol{r}V_{ext}(\boldsymbol{r})n(\boldsymbol{r}) \qquad (2.83)$$

for the nucleus-electron interactions. Then, using the above terms and two additional terms $E_{XC}[n]$ (exchange-correlation term that will be explained below), E_{II} (electrostatic interactions between nuclei that will be given as a constant), the energy functional of the auxiliary system was formulated as follows.

$$E^{KS}[n] = T_s[n] + E_{ee}[n] + E_{Ne}[n] + E_{XC}[n] + E_{II} \qquad (2.84)$$

Note, that the forth term $E_{XC}[n]$ corresponds to the exchange-correlation energy, where all the many-body effects that had not been described in Eq (2.81) and Eq (2.82) have been included. In other words, $E_{XC}[n]$ can be defined by the following formulas,

$$E_{XC}[n] = T[n] - T_s[n] + E_{int}[n] - E_{ee}[n] \qquad (2.85)$$

where $T[n]$ is the kinetic energy of the interacting system and $E_{int}[n]$ is the electron-electron

interaction in the interacting system.

Then, finally, the energy functional Eq (2.84) were minimized according to the variational principle proven in the Hohenberg-Kohn theorem 2, within the constraint of

$$\langle \psi_i^\sigma | \psi_i^\sigma \rangle = 1 \tag{2.86}$$

where the wave functions of the auxiliary system had been normalized. Subsequently, the ground-state energy and the ground-state electron density of the auxiliary system were obtained by the following stationary condition,

$$\frac{\delta}{\delta \psi_i^{\sigma*}(\boldsymbol{r})}\left[E^{KS}[n] - \sum_{\sigma'}\sum_{i=1}^{N^\sigma} \varepsilon_j^{\sigma'}\{\langle \psi_i^{\sigma'} | \psi_i^{\sigma'} \rangle - 1\}\right]$$
$$= \frac{\delta T_s[n]}{\delta \psi_i^{\sigma*}(\boldsymbol{r})} + \frac{\delta n^\sigma(\boldsymbol{r})}{\delta \psi_i^{\sigma*}(\boldsymbol{r})}\left[\int d^3\boldsymbol{r}' \frac{n(\boldsymbol{r}')}{|\boldsymbol{r}-\boldsymbol{r}'|} + V_{ext}(r) + \frac{\delta E_{XC}[n]}{\delta n^\sigma(\boldsymbol{r})}\right] - \varepsilon_i^\sigma \psi_i^\sigma(\boldsymbol{r}) = 0 \tag{2.87}$$

where the derivatives of T_s and $n^\sigma(\boldsymbol{r})$ can be deformed to

$$\frac{\delta T_s[n]}{\delta \psi_i^{\sigma*}(\boldsymbol{r})} = -\frac{1}{2}\nabla^2 \psi_i^\sigma(\boldsymbol{r}) \tag{2.88}$$

$$\frac{\delta n^\sigma(\boldsymbol{r})}{\delta \psi_i^{\sigma*}(\boldsymbol{r})} = \psi_i^\sigma(\boldsymbol{r}) \tag{2.89}$$

according to Eq (2.80) and Eq (2.81). Thus, the differential equation Eq (2.87) can be rewritten as,

$$H^{KS,\sigma}(r)\psi_i^\sigma(\boldsymbol{r}) = \varepsilon_i^\sigma \psi_i^\sigma(\boldsymbol{r}) \tag{2.90}$$

where

$$H^{KS,\sigma}(r) \equiv -\frac{1}{2}\nabla^2 + \int d^3\boldsymbol{r}' \frac{n(\boldsymbol{r}')}{|\boldsymbol{r}-\boldsymbol{r}'|} + V_{ext}(r) + \frac{\delta E_{XC}[n]}{\delta n^\sigma(\boldsymbol{r})} \tag{2.91}$$

whose form is similar to the one-electron equation derived in the Hartree-Fock approximation.

Thus, Kohn and Sham had succeeded to formalize of the energy functional predicted in the

Hohenberg-Kohn theorems, and to establish the procedure to obtain the electronic structures of many-electron systems from the energy functional with respect to the electron density as its argument.

2-3-4. The classification of exchange-correlation functionals

Although the feasible procedures to obtain the energy and the electron density of many-electron systems based on the Hohenberg-Kohn theorem had been established as the Kohn-Sham equations, there also remains an important issue to be solved – the formalism of $E_{XC}[n]$, the exchange-correlation functional, was not yet obtained. Indeed, $E_{XC}[n]$ is the only term that cannot be exactly formalized among the terms appeared in the Kohn-Sham equations, and thus a kind of approximations is needed to obtain its formalism. Therefore, there have been proposed a great number of approximative exchange-correlation functionals since the establishment of the Kohn-Sham equations. Here, in this section, the formalisms of the exchange-correlation functionals which are used in this thesis will be introduced.

2-3-4-1. LDA functionals

One of the representative examples of the exchange-correlation functional is the localized density approximation (LDA) functionals, where the local exchange-correlation energy ε_{XC} is assumed to be dependent only on the electronic density at each position $\boldsymbol{r}$.

$$E_{XC}^{LDA}[n] = \int d\boldsymbol{r} n(\boldsymbol{r}) \varepsilon_{XC}([n], \boldsymbol{r}) \tag{2.92}$$

Such approximation is based on the consideration that the term $E_{XC}[n]$ can be regarded as a local one since it was defined as the residual part of the energy of the many-electron system from which the

non-local terms such as the kinetic energy and the electrostatic energy had been subtracted as shown in Eq (2.85).

Here, the exchange part of $E_{XC}^{LDA}[n]$ consists of the formalization described in Eq (2.67) which is derived by Dirac, since it is the only exchange functional that is theoretically exact. On the other hand, the correlation part of $E_{XC}^{LDA}[n]$ is usually obtained by the parameter fitting to the numerically calculated correlation energies using the Monte Carlo methods on homogeneous electron gas systems. One of these examples is a PW-LDA correlation functional [17], which is used in chapter 6 of this thesis, as described as,

$$E_C^{PW-L}\ [n] = -2\mathrm{a}\int d^3\boldsymbol{r}n(1-\alpha r_s)ln\left[1+\frac{1}{2a\left(\beta_1 r_s^{\frac{1}{2}}+\beta_2 r_s+\beta_3 r_s^{\frac{3}{2}}+\beta_4 r_s^2\right)}\right] \quad (2.93)$$

where a = 0.031097, α = 0.21370, β_1 = 7.5957, β_2 = 3.5876, β_3 = 1.6382, β_4 = 0.49294, and r_s is the Wigner-Seitz radius that is defined as,

$$\frac{4}{3}\pi r_s^2 = \frac{1}{n} \quad (2.94)$$

2-3-4-2. GGA functionals

Next, the generalized gradient approximation (GGA) functionals, which are also representative as well as LDA functionals, will be explained. Within the generalized gradient approximation, the exchange-correlation energy is described as the functional of both electron density

$n(\boldsymbol{r})$ and its gradient $\nabla n(\boldsymbol{r})$. The general formalism of a GGA functional is as follows.

$$E_{XC}^{GGA}[n] = \int d\boldsymbol{r} n(\boldsymbol{r}) \varepsilon_{XC}(n(\boldsymbol{r}), \nabla n(\boldsymbol{r}), \boldsymbol{r}) \tag{2.95}$$

Here, the exchange part of $E_{XC}^{GGA}[n]$ is usually formulated as,

$$E_X^{GGA}[n] = -\frac{1}{2}\sum_{\sigma} \int d^3\boldsymbol{r} n_\sigma^{4/3} K_\sigma \tag{2.96}$$

where K_σ is described using a following dimensionless parameter x_σ.

$$x_\sigma = \frac{|\nabla n_\sigma|}{n_\sigma^{4/3}} \tag{2.97}$$

For instance, in the PBE (Perdew–Burke-Ernzerhof) functional [18], one of the most widely used GGA functionals as also was the case in chapter 3 to chapter 5, K_σ in the exchange part is given as,

$$K_\sigma^{PBE} = K_\sigma^{LDA}\left[1 + \kappa - \frac{\kappa}{1 + \mu s_\sigma^2/(48\pi^2)^{2/3}\kappa}\right] \tag{2.98}$$

$$K_\sigma^{LDA} = 3\left(\frac{3}{4\pi}\right)^{1/3} \tag{2.99}$$

where μ = 0.21951 and κ = 0.804.

On the other hand, the correlation part of $E_{XC}^{GGA}[n]$ is usually obtained by adding a GGA correction term to the corresponding LDA correlation functional. In the case for PBE, the correlation functional is given as,

$$E_C^{PBE}[n, \zeta, t] = E_C^{PW-}\quad[n] + \int d^3\boldsymbol{r} n(r) H[n, \zeta, t] \tag{2.100}$$

$$H[n, \zeta, t] = \gamma\phi^3 ln\left[1 + \frac{\beta}{\gamma} t'^2 \left(\frac{1 + At'^2}{1 + At'^2 + A^2 t'^4}\right)\right] \tag{2.101}$$

$$A = \frac{\beta}{\gamma}\left[\exp\left(-\frac{\bar{E}_C^{PW-}\quad[n]}{\gamma\phi^2 n}\right) - 1\right]^{-1} \tag{2.102}$$

$$\phi = \frac{1}{2}\left[(1+\zeta)^{2/3} + (1-\zeta)^{2/3}\right] \tag{2.103}$$

where $\gamma = \frac{1-ln2}{\pi^2} = 0.031091$ and $\beta = 0.066725$.

2-3-4-2. Hybrid functionals

On a final note, the hybrid functionals, which were used in estimating the bandgaps in chapter 3 to chapter 5, will be introduced. The Hybrid functional is the one whose exchange functional is modified by incorporating a portion of the exact exchange energy obtained in the Hartree-Fock approximation. Such modification is based on the consideration that there inevitably arise non-negligible self-interaction errors, which correspond to the unphysical electrostatic interaction between the electron and the electronic potential generated by the electron itself, in the derivation of the energy functionals (see Eq (2.82) and Eq (2.84)), while such self-interaction errors are fully cancelled in the formulation of the Hartree-Fock approximation by the exchange energy term (see Eq (2.60) to Eq (2.62)). In other words, the unphysical self-interaction errors are intended to be canceled by incorporating a portion of Hartree-Fock exchange energy term in the exchange functional used in the Kohn-Sham equations.

As for the HSE (Heyd-Scuseria-Ernzerhof) hybrid functional, which was used in this thesis, the Hartree-Fock exchange energy term is divided into two parts, a short-range part $E_X^{SR-HF}(\omega)$ and a long-range part $E_X^{SR-HF}(\omega)$, with respect to the parameter ω controlling the short-rangeness of the interaction, and only the former part is incorporated in the exchange functional [19]. Then, using the

mixing parameter a, the HSE exchange functional is given as,

$$E_X^{HSE} = aE_X^{SR-H}\ (\omega) + (1 - \mathrm{a})E_X^{PBE}(\omega) + E_X^{PBE}(\omega) \qquad (2.104)$$

where a = 0.25 and ω = 0.2 in case for HSE06. Such dividing of the Hartree-Fock exchange energy was proposed since the long-range part of the exchange energy had been empirically known to overestimate the bandgap energy, and thus the HSE functionals are considered to be superior in calculating bandgaps.

Bibliography

[1] Einstein, A. Uber einen die Erzeugung und Verwandlung des Lichtes betreffenden heuristischen Gesichtspunkt. *Annalen der Physik* **1905**, *17(6)* 132.

[2] Einstein, A. Ist die Trägheit eines Körpers von seinem Energieinhalt abhängig? *Annalen der Physik* **1905**, *323(13)* 639.

[3] de Broglie, L. Recherches sur la théorie des Quanta. *Ann. Phys.* **1925**, *10(3)*, 22.

[4] Schrödinger, E.; Quantisierung als Eigenwertproblem; von Erwin Schrödinger. *Annalen der Physik.* **1926**, *384*, 361.

[5] Born, M. Zur Quantenmechanik der Stoßvorgänge *Zeitschrift für Physik* **1926**, *37*, 863.

[6] Hartree, D. R. The Wave Mechanics of an Atom with a Non-Coulomb Central Field. Part I. Theory and Methods. *Math. Proc. Camb. Phil. Cos.* **1928**, *24*, 89.

[7] Hartree, D. R. The Wave Mechanics of an Atom with a Non-Coulomb Central Field. Part II. Some Results and Discussion. *Math. Proc. Camb. Phil. Cos.* **1928**, *24*, 111.

[8] Hartree, D. R. The wave mechanics of an atom with a non-Coulomb central field. part iii. Term values and intensities in series in optical spectra. *Math. Proc. Camb. Phil. Cos.* **1928**, *24*, 426.

[9] Slater, J. C. The Theory of Complex Spectra. *Phys. Rev.* **1929**, 34, 1923.

[10] Fock, V. Näherungsmethode zur Lösung des quantenmechanischen Mehrkörperproblems. *Z. Phys.* **1930**, 61, 126.

[11] Thomas, L. H. The calculation of atomic fields. *Proc. Cam. Phyl. Soc.* **1927**, *23*, 542.

[12] Fermi, E. Eine statistische Methode zur Bestimmung einiger Eigenschaften des Atoms und ihre Anwendung auf die Theorie des periodischen Systems der Elemente. *Z. Phys.* **1928**, *48*, 73.

[13] Dirac, P. A. M. Note on Exchange Phenomena in the Thomas Atom. *Camb. Phil. Soc.* **1930**, *26*, 376.

[14] Weizsäcker, C. F. On the theory of nuclear masses. *Z. Phys* **1935**, *96*, 431.

[15] Hohenberg, P.; Kohn. W. Inhomogeneous Electron Gas. *Phys. Rev. B*, **1964**, 136, 864.

[16] Kohn, W.; Sham, L. J. Self-Consistent Equations Including Exchange and Correlation Effects. *Phys. Rev. A* **1965**, *140*, 1133.

[17] Perdew, J. P.; Wang, Y. Accurate and simple analytic representation of the electron-gas correlation energy. *Phys. Rev. B* **1992**, *45*, 13244.

[18] Perdew, J. P.; Burke, K.; Ernzerhof, M. Generalized Gradient Approximation Made Simple. *Phys. Rev. Lett.* **1996**, *77*, 3865.

[19] Heyd, J.; Scuseria, G. E.; Ernzerhof, M. *J. Chem. Phys.* **2003**, *118*, 8207.

Chapter 3.
Effects of Anion Ordering in Perovskite Oxynitride: A Demonstration on $CaTaO_2N$

3-1. Introduction to anion ordering in perovskite oxynitrides

3-1-1. Perovskite oxynitride photocatalysts

During these decades, a wide range of water-splitting photocatalysts [1-9] have been discovered from a class of compounds with perovskite structure. “Perovskite” is originally the name of $CaTiO_3$ mineral, and the compounds that have the same type of crystal structures as $CaTiO_3$ are classified to perovskite compounds. Generally, perovskite compounds have ABX_3 chemical formulas like $CaTiO_3$, with anions X coordinating to cations B to shape BX_6 octahedral-units, sharing their apices forming a 3D network, and cations A (which is called A site cations) filling the gaps between the BX_6 octahedral-units (Figure 3-1). For many years, the class of perovskite compounds, in both their fully inorganic and hybrid organic−inorganic [10,11] structures, has been investigated for its ferroelectric features [12], the superconductivity [13], the colossal magnetoresistance effects [14], the recently observed superior features in photovoltaic applications [15-18], the low thermal conductive properties [19], as well as water-splitting photocatalysts, and thus they are considered to be one of the central research areas for functional materials.

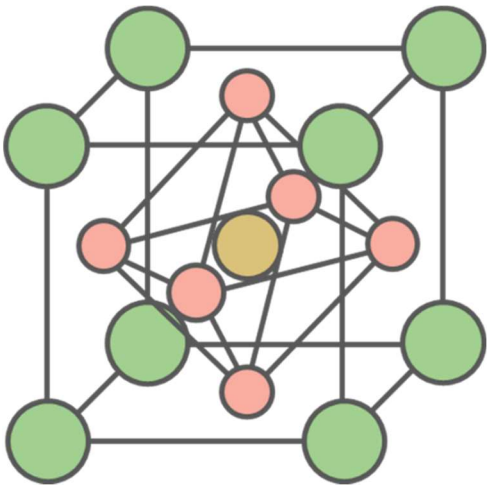

Figure 3-1. Schematic illustration of perovskite structure with ABX_3 chemical formula. Green, yellow, and pink are A, B, and X, respectively.

Among perovskite compounds, there also have been reported a lot of visible light-responsive oxynitride photocatalyts, such as $BaTaO_2N$ [7], $SrTaO_2N$ [7], $CaTaO_2N$ [6,7], $LaTiO_2N$ [8]. Very recently, overall water splitting under visible light irradiation has been achieved on $CaTaO_2N$ [6], although its activity is still low. $BaTaO_2N$ has also succeeded in producing hydrogen and oxygen independently from sacrificial aqueous solutions in the form of solid solution with $BaZrO_3$[20] under visible light. As explained in the chapter 1, these oxynitride photocatalyts have the valence bands that consist of O 2p and N 2p orbitals, and this makes the bandgaps narrow enough to utilize the energy of visible light. Therefore, perovskite oxynitrides are nowadays considered the most promising candidates for the water splitting photocatalysis process [21].

3-1-2. Anion ordering in perovskite oxynitrides

In the crystal of perovskite oxynitrides, O^{2-} and N^{3-} occupies X sites to coordinate to the transition metal cation center. Surprisingly, their anion arrangements of in the crystals (anion ordering, hereafter also called *aor*) have been found to be partially specific. For example, it is well known that N^{3-} coordinate to the cation center in *cis* configuration. Furthermore, Neutron [22-25] and electron [26] diffraction analyses have already shown specific anion distributions in the crystals of some perovskite oxynitrides.

Such ordered motifs are considered responsible for piezoelectricity [27] and ferroelectricity [28], as a consequence of the local distortion induced in the crystals of perovskite oxynitrides [29]. Subsequently, due to the nature of perovskite oxynitride VB, that, as said, mainly consists of O 2p and N 2p orbitals, it is evident that an impact of *aor* on the band structure of the final system exists. They are similarly reported to be controllable, leading to a further “tailorability” of the perovskite oxynitride electronic features [30], either by tuning temperature conditions [25] or via the cooling rate after the calcination [31], making the *aor* a potentially powerful factor for modifying the optical and electronic features of such compounds.

However, it is still difficult to clarify the details of anion ordering in oxynitride crystals, since only the O/N occupation on each site can be experimentally measured by the state of art method. There also exists some controversial data indicating the nature of one-dimensional (1D) [22], two-

dimensional (2D) [25], and three-dimensional (3D) ordering [32] have been reported from different experimental groups. Besides, it is also a challenging task to synthesize perovskite oxynitrides with a specific anion arrangement, and such limitations makes the investigation on anion ordering a puzzling issue. Therefore, the band structure variation ascribed to the change in *aors* is still unclear, and thus the relation between *aor*s and their electronic properties has not been fully analyzed yet. In addition, to the best of our knowledge, no data have been reported focusing on possible improvements of the photocatalytic activity as a function of the *aor* motif.

3-1-3. Objective of this work

To overcome these issues, a theoretical, unbiased understanding of the relation between *aor*s and the electronic structure of this class of materials is mandatory. Thus, in this research, by means of first-principles calculations, I aim to clarify the relation between the *aor* (structural features) and perovskite oxynitride band structures (electronic features). In particular, our analysis will mainly focus on $CaTaO_2N$, a material whose ability to split water under visible light irradiation is well documented [6,7]. I aim to demonstrate the tunability of the band structure by controlling its anion ordering, thus providing a guideline to possibly improve the photocatalytic properties of $CaTaO_2N$.

3-2. Computational details

Several initial guesses of $CaTaO_2N$ were prepared with different *aor*s following the available neutron diffraction data [22], relaxing them by means of a density functional theory (DFT) based approach, as implemented in the VASP code [33-36]. The projector augmented wave (PAW) method [37,38] with the GGA-PBE exchange-correlation functional [39] was used with a cutoff energy of 500 eV. All the structures were optimized using a 10 × 7 × 10 Γ-centered *k*-point sampling of the Brillouin zone (BZ) until the forces on all atoms were smaller than 0.01 eV/Å.

According to the available data [22], $CaTaO_2N$ has a unit cell with space group *Pnma*, and the O/N ratio is about 1:1 on the axial sites and 3:1 on the equatorial sites. It is well-known that more electronegative anions in the octahedral (O_h) units of perovskites usually have a *cis* configuration with respect to the central metal cation, as mentioned in the previous section [40]. Neglecting the tilting of the TaO_4N_2 O_h unit (octahedral-tilting [41]), six N^{3-} arrangements within the *cis* configuration are possible, which satisfy the mentioned O/N occupations, as shown in the first column of Figure 3-2. On the other hand, including the tilting, it was finally able to model 13 different *aor*s (structures on the right side of Figure 3-2). Since N^{3-} are arranged in a 2D fashion in A−D and in a 3D one in E−F, the former will be called “two-dimensional (or 2D) *aor*s” and the latter will be called “three-dimensional (or 3D) *aor*s”.

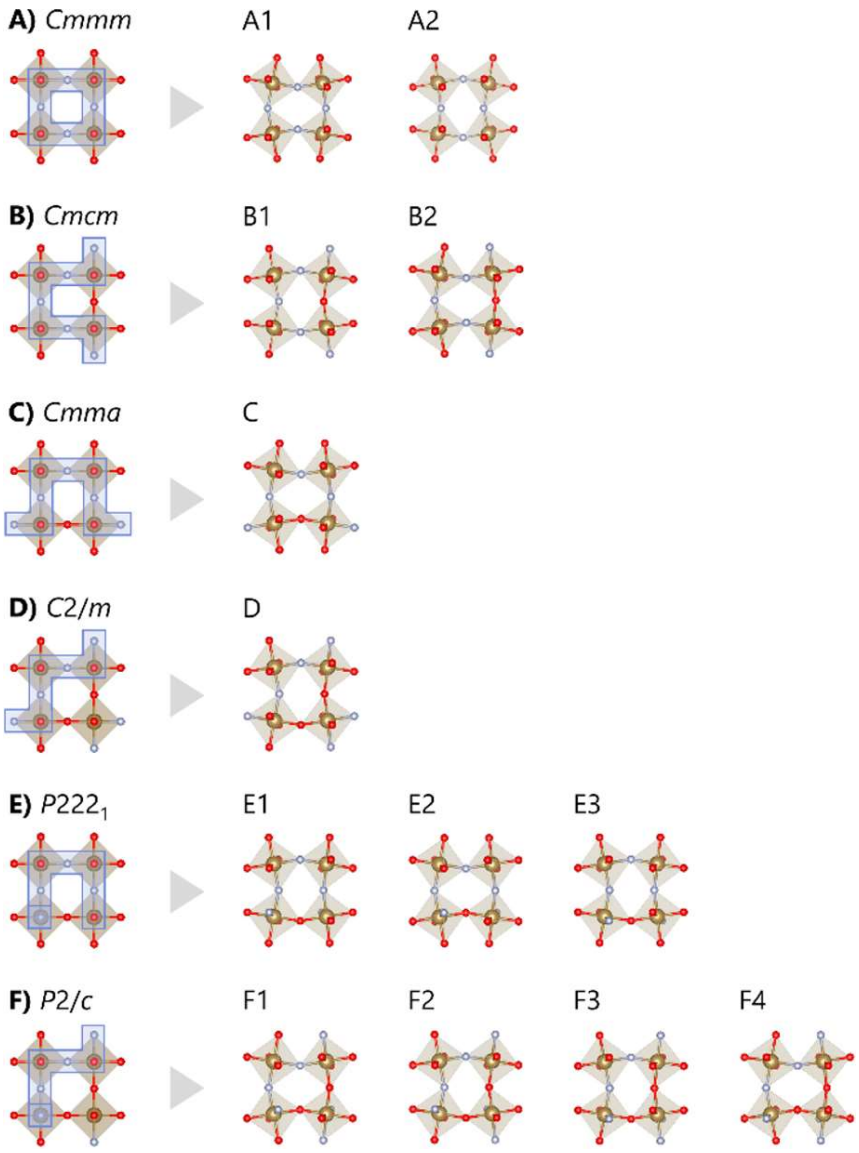

Figure 3-2. Initial structure of each anion ordering, without (left) and with (right) O_h tilting considered [brown, red, and blue are Ta, O, and N atoms, respectively]. Ca atoms are omitted. These had derived from an exhaustive arrangement of O/N according the experimentally obtained occupation ratio at each site, and consequently $2^2 \times 4^2 = 64$ different O/N arrangements was obtained (where 2^2 and 4^2 are the number of possible outcomes at axial and equatorial sites, respectively). Then, since some of them are essentially the same ones due to their symmetries, they are reduced to 13 anion arrangements.

The electronic properties were calculated by means of a 12 × 9 × 12 Γ-centered *k*-point sampling of the BZ. At variance with the hybrid organic−inorganic halide perovskites for which the relativistic effect impact on the final electronic features is massive [16,17], the different nature of the band edges makes the same inclusion in our systems ineffective, with the final bandgaps that remain unaltered.

According to the parabolic approximation, the effective masses of holes (m_h*) and of electrons (m_e*) were estimated as result of the fit of the dispersion relation described in Eq (3.1). Starting from the CBM (VBM), the curvature of the bands was calculated within a *k*-point range of ± 0.05 $Å^{-1}$. In order to include the anisotropic effects of the dispersion in the BZ, the effective masses calculated from the band edges along the direction toward the other seven high symmetry points were averaged as their harmonic mean (see Eq (3.2)). Tables 3-1 (a) and (b) list the effective masses calculated for the directions considered.

$$m^* = \hbar^2 \left[\frac{\partial^2 \varepsilon(k)}{\partial k^2} \right]^{-1} \tag{3.1}$$

$$\frac{1}{m_{ave}^*} = \frac{1}{N} \sum_{i=1}^{N} \frac{1}{m_i^*} \tag{3.2}$$

Here $\varepsilon(k)$ are the band edge eigenvalues, k is the wavevector, m_i^* is the effective mass along each direction, i, and m_{ave}^* is the averaged effective mass.

Band edge positions are calculated as orbital energies referred to the vacuum level [42]. In detail, both vacuum level and orbital energies are calculated by means of slab models whose bulk and

Table 3-1. (a) Hole effective mass along each direction. B2 and C have their VBMs on U point.

(Γ = 0.0, 0.0, 0.0; X = 0.5, 0.0, 0.0; Y = 0.0, 0.5, 0.0; Z = 0.0, 0.0, 0.5; S = 0.5, 0.5, 0.0;

T = 0.0, 0.5, 0.5; U = 0.5, 0.0, 0.5; R = 0.5, 0.5, 0.5).

	T→Γ	T→R	T→S	T→U	T→X	T→Y	T → Z	**Ave**
A1	1.72	4.44	0.88	5.25	1.07	1.24	7.24	**1.74**
A2	1.43	4.69	2.45	1.41	1.51	4.67	0.59	**1.52**
B1	3.14	1.94	1.30	2.07	1.45	3.86	2.14	**2.00**
D	0.51	1.35	0.80	0.55	0.41	1.50	0.78	**0.69**
E1	1.65	1.89	195	1.71	11.1	1.52	1.31	**2.16**
E2	-7.5	2.66	6.14	2.04	17.1	13.8	1.38	**3.99**
E3	1.35	3.12	3.41	1.32	1.73	3.76	0.61	**1.52**
F1	1.25	1.64	1.85	0.77	0.98	2.06	0.83	**1.17**
F2	4.85	0.92	1.17	0.86	1.80	1.56	0.75	**1.20**
F3	1.26	1.65	1.86	3.29	2.32	2.06	0.82	**1.60**
F4	5.72	1.92	1.81	1.30	3.19	1.65	0.76	**1.65**
	U→Γ	U→R	U→S	U→T	U→X	U→Y	U→Z	**Ave**
B2	7.34	1.43	2.02	2.69	2.47	4.05	4.61	**2.72**
C	1.19	51.2	2.41	3.57	2.27	1.32	2.69	**2.24**

Table 3-1. (b) Electron effective mass along each direction.

(BZ special point coordinates as in Table 3-1 (a))

	Γ→R	Γ→S	Γ→T	Γ→U	Γ→X	Γ→Y	Γ→Z	**Ave**
A1	0.63	0.63	0.68	0.62	0.62	0.68	0.68	**0.65**
A2	0.51	0.65	0.71	0.52	0.76	0.51	0.88	**0.62**
B1	0.45	0.58	0.57	0.46	0.79	0.39	0.75	**0.54**
B2	0.50	0.67	0.57	0.55	1.07	0.38	0.75	**0.59**
C	0.98	1.75	1.01	0.86	1.54	0.91	1.12	**1.10**
D	0.50	0.67	0.60	0.53	0.90	0.45	0.77	**0.60**
E1	0.55	0.60	0.76	0.55	0.69	0.52	0.87	**0.63**
E2	0.95	0.69	1.11	0.94	0.74	0.62	1.08	**0.84**
E3	0.83	0.75	0.77	1.09	0.85	0.61	1.26	**0.83**
F1	0.63	0.77	0.61	0.69	1.05	0.40	0.86	**0.66**
F2	0.73	0.66	0.72	0.76	0.70	0.62	0.75	**0.70**
F3	1.00	0.61	0.61	2.11	1.05	0.40	0.85	**0.74**
F4	0.90	0.74	0.75	1.14	1.03	0.49	0.94	**0.80**

vacuum regions are thick enough to minimize the quantum confinement effects and to avoid spurious effects among replicas of the slabs along the direction normal to the surface. It is straightforward that such a method does not apply to the slab models which have a net dipole vertical to their surface planes [42,43]. Since, in $CaTaO_2N$, Ta−N and Ta−O bonds have different charge distributions (dipoles), only the slab models assembled from certain *aor*s, which expose specific facets that are suitable for calculating the vacuum level. Furthermore, it remains quite cumbersome to discuss the difference of the band edge positions among different *aor*s, due to the strong dependence of the calculated vacuum levels on the slab surface structures [44]. Accordingly, to better assess our results, I have considered only one type of slab model, i.e. that for which the difference between the potential in the bulk region of the slab model ($V_{\mathrm{bulk-slab}}$) and that of the bulk (V_{bulk}) is minimized [45].

First, the potentials in both the vacuum ($V_{\mathrm{vac-slab}}$) and bulk regions ($V_{\mathrm{bulk-slab}}$) and the energies of the CBM ($\varepsilon_{\mathrm{CBM-slab}}$) and the VBM ($\varepsilon_{\mathrm{VBM-slab}}$) were calculated by using the nonpolar, symmetric, and thermodynamically more stable slab (E_{surf} as in Eq (3.3), where E_{slab} is the total energy of the slab model, n is the number of the bulk unit cells in the slab, E_{bulk} the energy of the bulk per unit formula, and A is the superficial area of the slab).

$$E_{\mathrm{surf}} = \frac{E_{\mathrm{slab}} - n \times E_{\mathrm{bulk}}}{2A} \tag{3.3}$$

Second, the potential in the bulk model (V_{bulk}) and its band edge energies ($\varepsilon_{\mathrm{CBM}}$, $\varepsilon_{\mathrm{VBM}}$) were calculated by using the bulk models of each *aor*, respectively. In addition, their bandgaps have

also estimated by using the hybrid functional HSE06 [46-48] in order to compensate the underestimation of the pure DFT calculated bandgaps and compare the band edge positions to the water redox potentials.

Finally, assuming that the two bulk potentials coincide ($V_{\mathrm{bulk-slab}} \cong V_{\mathrm{bulk}}$), hypothetical vacuum potentials (V'_{vac}) were calculated for each *aor* as in Eq (3.4). Then their band edge positions were determined and corrected as in Eq (3.5) and Eq (3.6), provided that the calculated bandgap is that of Kohn−Sham, as in our case, and assuming the fact that conventional DFT can reproduce theoretically the exact position of the band gap center [49].

$$V'_{\mathrm{vac}} = V_{\mathrm{bulk}} + (V_{\mathrm{vac-slab}} - V_{\mathrm{bulk-slab}}) \tag{3.4}$$

$$E_{\mathrm{CBM(VBM)}} = \varepsilon_{\mathrm{CBM(VBM)}} - V'_{\mathrm{vac}} \tag{3.5}$$

$$E_{\mathrm{CBM(VBM)}} \rightarrow E_{\mathrm{CBM(VBM)}} \pm \frac{1}{2}\{E_{\mathrm{g}} - (\varepsilon_{\mathrm{CBM}} - \varepsilon_{\mathrm{VBM}})\} \tag{3.6}$$

I have thus prepared six initial models (shown in Figure 3-3) and compared their surface energies. All the slab models are 32 Å long (6-unit layers) along the direction normal to the surface plane plus an 18 Å vacuum region along the same direction. As a result, E2(001)_O rich, a slab model of the pristine E2 bulk *aor*, whose surface consists of an oxygen-terminated (001) facet, have been selected.

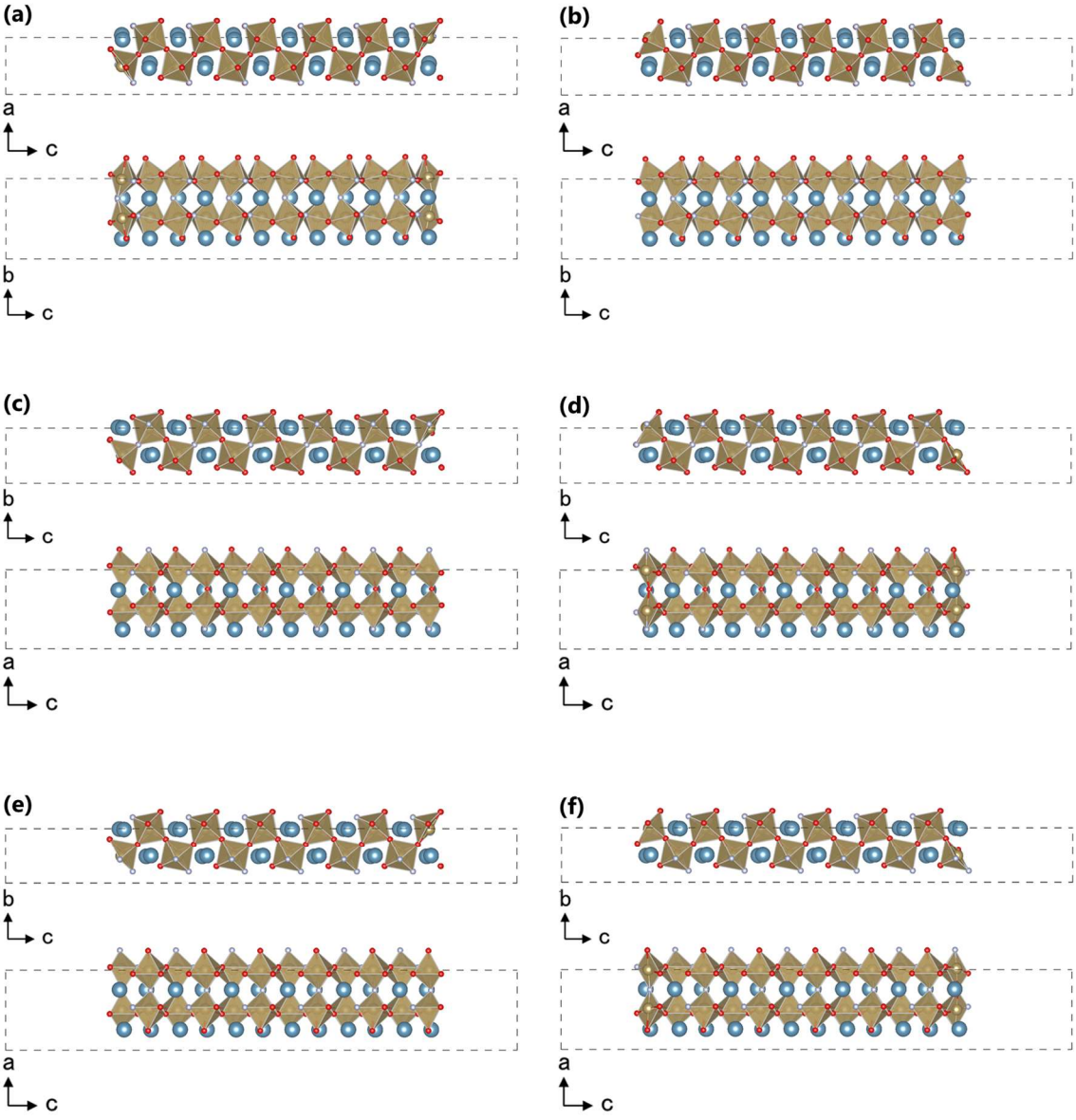

Figure 3-3. Lateral views of the three nonpolar slab models considered (Brown: Ta; red: O; light blue: N; blue: Ca). (a, b) E2 with (001) surface, (c, d) F2 with (100) surface, and (e, f) F4 with (100). Right: N-rich surface slabs. Left: corresponding O-rich surface slabs.

Starting from the very well converged structure (vide supra) of the bulk, for the slab models the convergence is achieved using reduced sampling (compared to the bulk case) of the BZ. In this case, it was sufficient to relax the slab ionic positions using a 4 × 4 × 1 Γ-centered *k*-point sampling until the forces were smaller than 0.05 eV/Å. On the optimized structures, their electronic properties were calculated until their total energies were converged within 10^{-4} eV, using a 4 × 6 × 1 Γ-centered mesh.

For all the considered slab models, the bandgap in the bulk regions (E_g(slab)) minimizes the difference with that of the corresponding bulk models (E_g) ($\Delta E_g \leq 0.13$ eV). Table 3-2 reports the surface energies and bandgaps of each slab model here investigated.

Table 3-2 Surface energies and bandgaps of each slab model.

	E_{surf} [mJ/m^2]	E_g (slab) [eV]	E_g [eV]
E2(001)_Orich	983.1	1.95	1.84
E2(001)_Nrich	1261.5	1.86	1.84
F2(100)_Orich	1002.6	2.14	2.01
F2(100)_Nrich	1429.1	2.06	2.01
F4(100)_Orich	1077.7	2.15	2.07
F4(100)_Nrich	1337.7	2.15	2.07

3-3. Impacts of anion orderings on photocatalyst related properties

I start discussing the impact of the *aor* motif on the bandgaps. Figure 3-4 shows the bandgap vs formation energy trend. Interestingly, the formation energy range of all the considered structures almost coincides with the thermal energy at room temperature (26 meV), indicating that various *aor*s can coexist in $CaTaO_2N$ crystals.

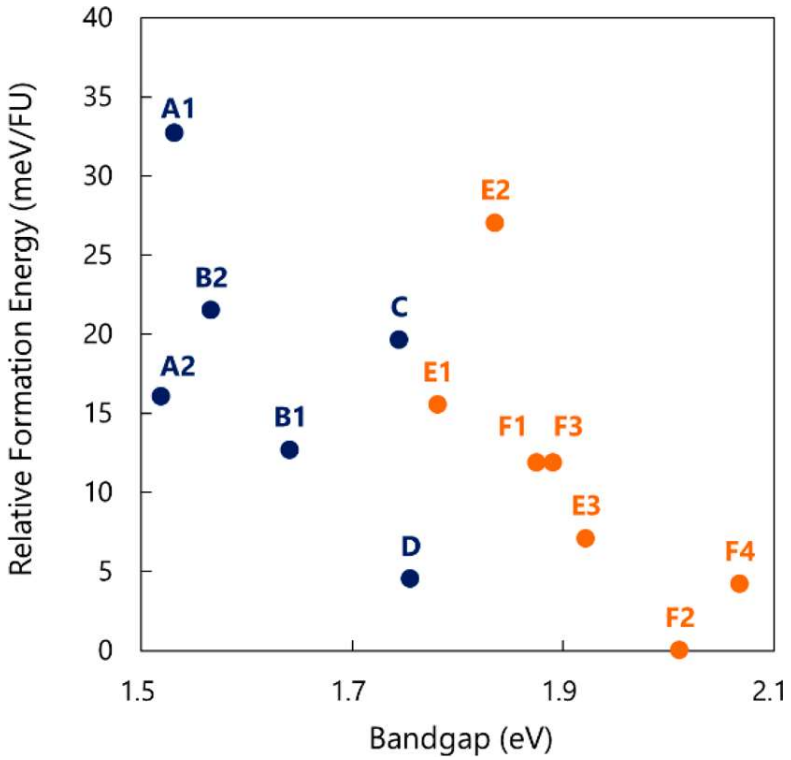

Figure 3-4. Bandgaps vs formation energy of each anion ordering. Zero on the y axis is the energy of the most stable anion ordering. Blue: 2D *aor*s, Red: 3D *aor*s.

Concerning the bandgap, marked differences among/the considered *aor*s, up to 0.5 eV, can be observed with the 3D motifs (E−F) characterized by larger values of the gap. It is thus likely that the absorption wavelength of $CaTaO_2N$ can be tuned by changing the *aor*. Still, Figure 3-4 suggests that the more stable the *aor*, the larger the bandgap, supporting the idea of the VBM stabilization for 3D motifs.

In Figure 3-5 I report both the electron (m_e*) and hole (m_h*) effective mass change as a function of the *aor*. Interestingly enough, the variation range of the hole effective mass is about 5 times that of the electron, indicating the hole mobility, and thus oxygen evolution reaction (OER), is more likely to be affected by the nature of the *aor*. Changes in valence band structures are observed as well in the different anisotropies of the carrier effective mass (Tables 3-1) and bandplots (Figure 3-6): m_e* is the minimum along the direction of Γ→ Y in almost all *aor*s, while m_h* has a more heterogeneous trend. To further confirm it, Figure 3-6 clearly shows that the CB shapes are similar in each *aor*, while those of the VB are quite different.

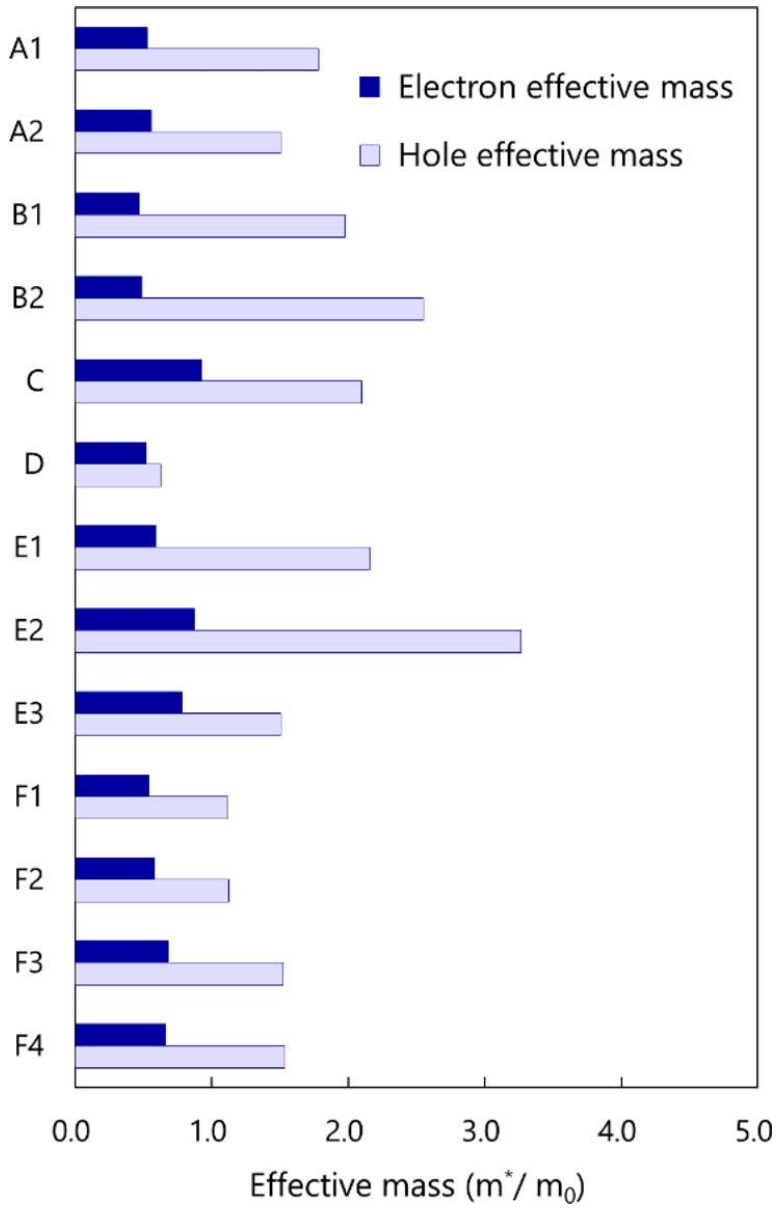

Figure 3-5. Carrier effective masses for each anion ordering

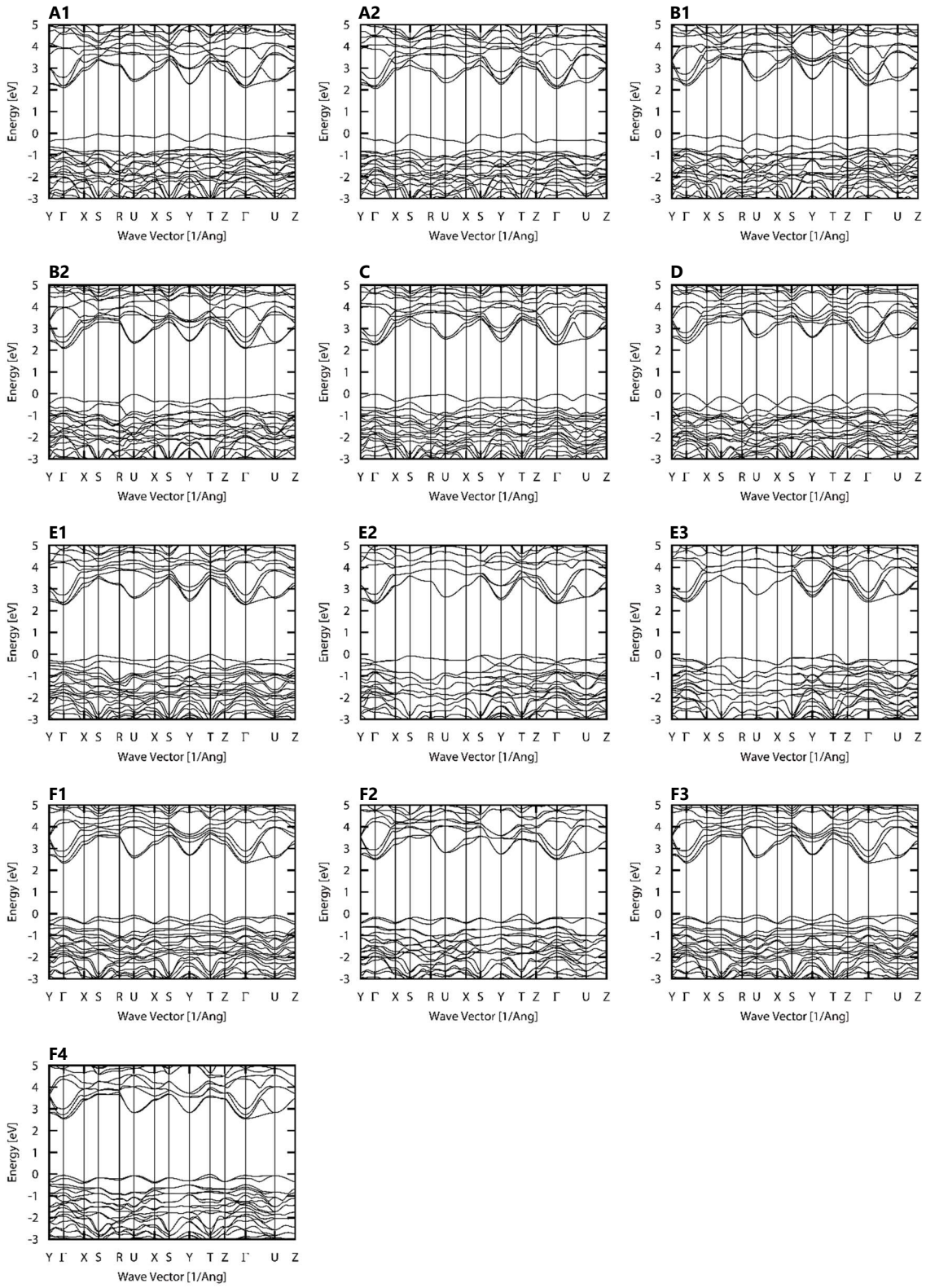

Figure 3-6. Bandplots of each anion ordering (BZ special point path coordinates as in Table 3-1.)

Finally, the variation of the band edge positions and its relation with the *aor* were analyzed. From Figure 3-7, the VBM positions vary within the range 1.14 to 1.66 V (vs NHE), while CBM remains almost unaltered.

Furthermore, 3D *aor*s have a more positive VBM than 2D ones, indicating additional stabilization of the valence bands for the former motifs. In all cases, CBM positions largely exceed the H_2O reduction potential, indicating the high potentiality to produce hydrogen, while VBM positions only appeared near the oxygen evolution potential, confirming previous experimental and theoretical findings [6,50]. Since all the 3D *aor*s have VBM positions positive enough for water oxidation, I conclude that $CaTaO_2N$ OER performances will be highly improved by the three-dimensional motif of the atomic ordering.

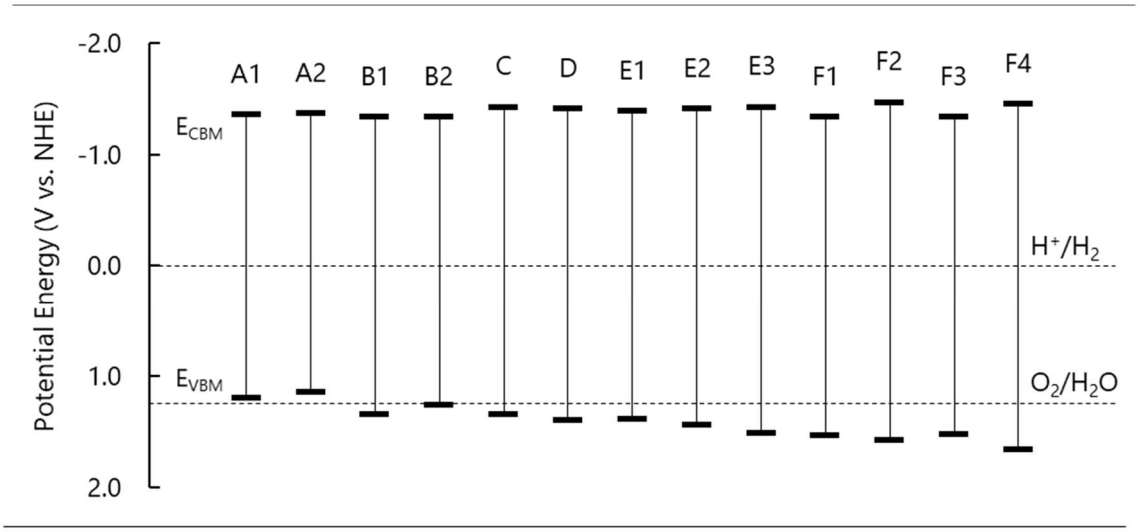

Figure 3-7. Band edge positions of each anion ordering. The potentials were referenced to the normal hydrogen electrode (NHE).

3-4. Origin of the different nature of electronic structures

In order to disclose the origin of the different nature of valence band structures and the relative maximum positions among *aor*s, the band edges electronic composition were analyzed. The Density of States (DOS) and Projected Density of States (PDOS) are shown in Figure 3-8.

As expected, in all *aor*s, the VB mainly consists of X (= O, N) 2p orbitals, while the CB mainly of Ta 5d ones. However, while the CB DOS shape is very similar for all the systems taken into account, that of the VB is quite different. A consequence associated with this finding is the different lifetimes of the hole that increase (decrease) as the VB DOS values are small (large) below the VBM. There is indeed a straight relation between DOS shape and the number of carrier relaxation paths that induce longer/shorter carrier lifetimes [18, 51-53]. In the PDOS near the VBM, only the contributions of both N 2p and O 2p orbitals are observed in 2D *aor*s, while an additional contribution of the Ta 5d orbital exists in 3D motifs, indicating orbital overlap among N 2p, O 2p, and Ta 5d orbitals in the latter ones.

I have similarly compared several optimized structural parameters (reported in Table 3-3) to find out what type of interactions occur among these orbitals and checked the influence of *aor* dimensionality on such interactions. Comparing the ∠Ta−O−Ta and ∠Ta−N−Ta angles, the latter clearly is larger in all *aor*s. In addition, the Ta−N bond lengths ($r_{\mathrm{Ta-N}}$) are shorter than the Ta−O ($r_{\mathrm{Ta-O}}$) ones, in contrast with the ionic radius based expected trend (N^{3-}: 1.46 Å; O^{2-}: 1.38 Å [12]),

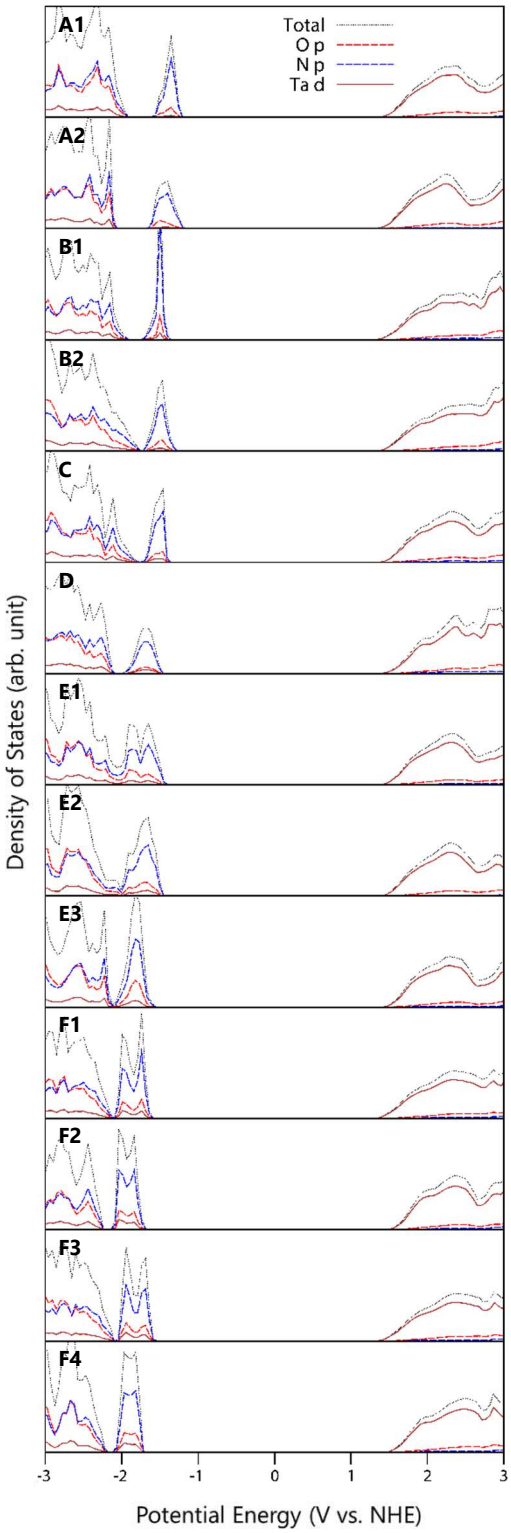

Figure 3-8. DOS and PDOS of each *aor,* calculated with the HSE06 level. The energies were referenced to the NHE.

suggesting further possible interactions, other than ionic, between Ta and X (=O, N). It is indeed well-known that anions with reduced electronegativity (N in our case) tend to more easily form covalent bonds. Previous NMR analysis supports our finding, reporting the covalent character of Ta−N bonds in $ATaO_2N$ (A = Ca, Sr, Ba [55]). Such a covalent character can clearly take into account the larger ∠ Ta−N−Ta angles and the shorter $r_{\mathrm{Ta-N}}$ bond lengths in $CaTaO_2N$. More in detail, the two bonds formed from X (=O, N) toward two adjacent Ta cations have different lengths (see Figure 3-9(a)): such asymmetry can be similarly ascribed to covalent interactions between X 2p and Ta 5d, as depicted in Figure 3-9(b) for the case of X = N ($d-p\pi$ interaction [24, 25, 40, 55]). These features are also shown in the VBM wave function (See Figure 3-9(c)).

Table 3-3. Optimized structural parameters of each anion ordering.

	Lattice parameters (Å)			Bond angles (deg)		Bondlength (Å)		Bondlength difference (Å)	
	a	b	c	∠Ta-O-Ta	∠Ta-N-Ta	$r_{\mathrm{Ta-O}}$	$r_{\mathrm{Ta-N}}$	$\Delta r_{\mathrm{Ta-O}}$	$\Delta r_{\mathrm{Ta-N}}$
A1	5.66	7.95	5.56	150.4	155.1	2.08	1.99	0.03	0.01
A2	5.66	7.94	5.57	150.6	155.8	2.08	1.98	0.06	0.03
B1	5.68	7.95	5.57	150.8	154.7	2.09	1.98	0.07	0.05
B2	5.65	7.97	5.57	149.3	156.7	2.08	1.98	0.08	0.04
C	5.66	7.97	5.56	150.0	156.1	2.08	1.99	0.07	0.09
D	5.66	8.00	5.57	148.8	157.7	2.09	1.98	0.14	0.14
E1	5.65	7.97	5.55	150.6	155.2	2.08	1.98	0.04	0.04
E2	5.65	7.98	5.55	150.6	155.2	2.08	1.98	0.06	0.07
E3	5.66	7.96	5.56	150.1	156.4	2.08	1.98	0.09	0.07
F1	5.66	7.98	5.56	150.3	156.2	2.09	1.98	0.09	0.05
F2	5.67	8.00	5.56	150.0	155.6	2.10	1.97	0.13	0.12
F3	5.66	7.98	5.56	150.3	156.3	2.09	1.98	0.09	0.05
F4	5.65	8.01	5.56	148.6	158.5	2.09	1.98	0.14	0.12
ave	**5.65**	**7.97**	**5.56**	**150.0**	**156.1**	**2.08**	**1.98**	**0.08**	**0.07**

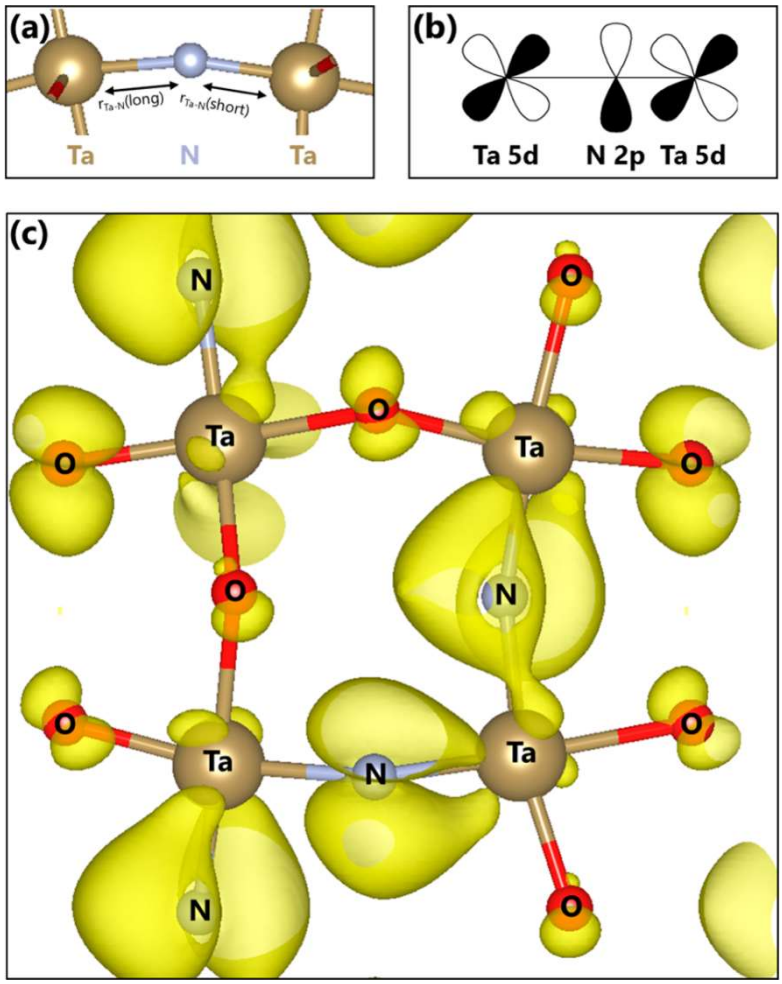

Figure 3-9. (a) Asymmetry bond length around nitrogen. (b) $d-p\pi$ interaction. (c) Decomposed charge density at the VBM of F2.

To further shed light on this feature, the asymmetry ($\Delta r_{\mathrm{Ta-N}}$) of the bond lengths among the anion orderings, i.e. the difference between the long and the short Ta−X bond length, have also been compared. From Table 3-3, 3D *aor*s have larger asymmetry than 2D ones, indicating the increased covalent character in the former ones. Furthermore, more asymmetric *aor*s have lower VBM positions (Figure 3-10), showing the relation between the VBM position and the degree of covalence between Ta and X. Noticeably, in 3D motifs, the much larger Ta−X $d-p\pi$ interactions induce the stabilization and thus the lowering of their VBM.

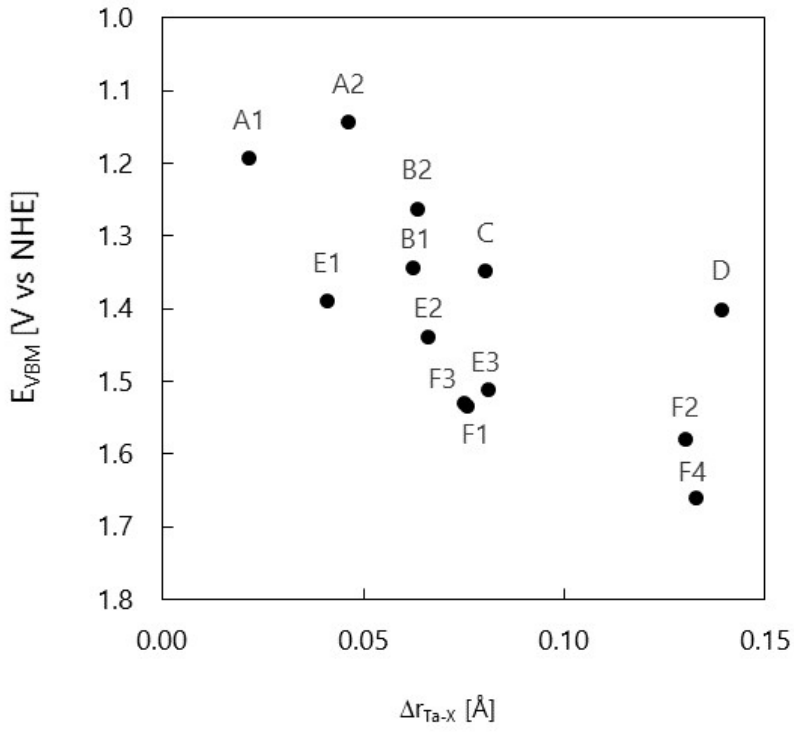

Figure 3-10. Bond asymmetry and VBM positions of each anion ordering. $\Delta r_{\mathrm{Ta-X}}$ represents the average of the bond difference between two bonds from N or O to Ta (= (2 × $\Delta r_{\mathrm{Ta-O}}$ + $\Delta r_{\mathrm{Ta-N}}$)/3).

Finally, the origin of the different magnitudes of the $d-p\pi$ interactions will be discussed. In 2D *aor*s, both N 2p orbitals and Ta 5d orbitals lie in the same plane, and thus, such symmetry does not allow their optimal overlap. On the other hand, the symmetry of the N 2p bands lowers in the VB of 3D *aor*s, since the nitrogen and tantalum atoms are not in the same plane: stronger stabilizing $d-p\pi$ interactions will originate as a consequence of the less hindered overlap between the N 2p and Ta 5d bands. Importantly, due to the fact that in all our systems Ca bands are very deep (high) in the valence (conduction) region (not shown here), these findings can be extended to all the perovskite oxynitrides of formula $ATaO_2N$ and analogous symmetry.

3-5. Conclusion

Aiming to provide viable paths to improve its photocatalytic activity, I have investigated the relation between anion orderings and electronic properties in $CaTaO_2N$. For several models assembled according to the available experimental data, I have focused on the photocatalytic oriented properties, comparing them among the different anion orderings here considered. I observed noticeable variations depending on the anion ordering: bandgaps become “tunable” in quite a wide range by controlling the structural motif. Carrier effective masses similarly vary among different anion orderings mainly for the hole, indicating that the oxygen evolution ability is significantly affected by the positions of the nitrogen and oxygen atoms in the crystal. Band edge positions vary as well, mainly in the valence region. Since three-dimensional anion orderings are associated with a more positive valence band maximum than two-dimensional ones, they are expected to be characterized by improved performances in the oxygen evolution reaction process. Therefore, through the optimization of its synthetic route, i.e. keeping either high temperature processing or slow cooling regime conditions, both reported to favor the three-dimensional anion ordering formation, $CaTaO_2N$ performances in photocatalysis will be highly improved.

Bibliography

[1] Yoneyama, H.; Koizumi, M.; Tamura, H. Photolysis of Water on Illuminated Strontium Titanium Trioxide. *Bull. Chem. Soc. Jpn.* **1979**, *52*, 3449.

[2] Domen, K.; Naito, S.; Onishi, T.; Tamaru, K. Study of the Photocatalytic Decomposition of Water Vapor over a NiO-$SrTiO_3$ Catalyst. *J. Phys. Chem.* **1982**, *86*, 3657.

[3] Kato, H.; Kudo, A. New tantalate photocatalysts for water decomposition into H_2 and O_2. *Chem. Phys. Lett.* **1998**, *295*, 487.

[4] Kato, H.; Asakura, K.; Kudo, A. Highly Efficient Water Splitting into H_2 and O_2 over Lanthanum-Doped $NaTaO_3$ Photocatalysts with High Crystallinity and Surface Nanostructure. *J. Am. Chem. Soc.* **2003**, *125*, 3082.

[5] Pan, C.; Takata, T.; Nakabayashi, M.; Matsumoto, T.; Shibata, N.; Ikuhara, Y.; Domen, K. A Complex Perovskite-Type Oxynitride: The First Photocatalyst for Water Splitting Operable at up to 600 nm. *Angew. Chem. Int. Ed.* **2015**, *54*, 2955.

[6] Xu, J.; Pan, C.; Takata, T.; Domen, K. Photocatalytic overall water splitting on the perovskite-type transition metal oxynitride $CaTaO_2N$ under visible light irradiation. *Chem. Commun.* **2015**, *51*, 7191.

[7] Yamasita, D.; Takata, T.; Hara, M.; Kondo, J. N.; Domen, K. Recent progress of visible-light-driven heterogeneous photocatalysts for overall water splitting. *Solid State Ionics* **2004**, *172*, 591.

[8] Kasahara, A.; Nukumizu, K.; Hitoki, G.; Takata, T.; Kondo, J. N.; Hara, M.; Kobayashi, H.; Domen,

K. Photoreactions on $LaTiO_2N$ under Visible Light Irradiation. *J. Phys. Chem. A* **2002**, *106*, 6750.

[9] Liu, M.; You, W.; Lei, Z.; Takata, T.; Domen, K.; Li, C. Photocatalytic Water Splitting to Hydrogen over a Visible Light Driven $LaTaON_2$ Catalyst. *Chin. J. Catal*. **2006**, *27*, 556.

[10] Weber, D. $CH_3NH_3SnBr_xI_{3-x}$ (x = 0−3), a Sn(II)-System with Cubic Perovskite Structure. *Z. Naturforsch*. **1978**, *33b*, 862.

[11] Weber, D. $CH_3NH_3PbX_3$, a Pb(II)-System with Cubic Perovskite Structure. *Z. Naturforsch*. **1978**, *33b*, 1443.

[12] Kim, Y.-I.; Woodward, P. M.; Baba-Kishi, K. Z.; Tai, C. W. Characterization of the Structural, Optical, and Dielectric Properties of Oxynitride Perovskites AMO_2N (A = Ba, Sr, Ca; M = Ta, Nb). *Chem. Mater.* **2004**, *16*, 1267.

[13] Maeno, Y.; Hashimoto, H.; Yoshida, K.; Nishizaki, S.; Fujita, T.; Bednorz, J. G.; Lichtenberg, F. Superconductivity in a layered perovskite without copper. *Nature* **1994**, *372*, 532.

[14] Uehara, M.; Mori, S.; Chen, C. H.; Cheong, S.-W. Percolative phase separation underlies colossal magnetoresistance in mixed-valent manganites. *Nature* **1999**, *399*, 560.

[15] Kojima, A.; Teshima, K.; Shirai, Y.; Miyasaka, T. Organometal Halide Perovskites as Visible-Light Sensitizers for Photovoltaic Cells. *J. Am. Chem. Soc*. **2009**, *131*, 6050.

[16] Giorgi, G.; Fujisawa, J.-I.; Segawa, H.; Yamashita, K. Small Photocarrier Effective Masses Featuring Ambipolar Transport in Methylammonium Lead Iodide Perovskite: A Density Functional

Analysis. *J. Phys. Chem. Lett*. **2013**, *4*, 4213.

[17] Even, J.; Pedesseau, L.; Jancu, J.-M.; Katan, C. Importance of Spin−Orbit Coupling in Hybrid Organic/Inorganic Perovskites for Photovoltaic Applications. *J. Phys. Chem. Lett.* **2013**, *4*, 2999.

[18] Kawai, H.; Giorgi, G.; Marini, A.; Yamashita, K. The Mechanism of Slow Hot-Hole Cooling in Lead-Iodide Perovskite: First-Principles Calculation on Carrier Lifetime from Electron−Phonon Interaction. *Nano Lett*. **2015**, *15*, 3103.

[19] Hata, T.; Giorgi, G.; Yamashita, K. The Effects of the Organic− Inorganic Interactions on the Thermal Transport Properties of $CH_3NH_3PbI_3$. *Nano Lett*. **2016**, *16*, 2749.

[20] K. Maeda, K. Domen. Preparation of $BaZrO_3$-$BaTaO_2N$ solid solutions and the photocatalytic activities for water reduction and oxidation under visible light. *J. Catal.* **2014**, *310*, 67.

[21] Maeda, K.; Domen, K. Photocatalytic Water Splitting: Recent Progress and Future Challenges. *J. Phys. Chem. Lett.* **2010**, *1*, 2655.

[22] Günther, E.; Hagenmayer, R.; Jansen, M. Structural Investigations on the Oxidenitrides $SrTaO_2N$, $CaTaO_2N$ and $LaTaON_2$ by Neutron and X-ray Powder Diffraction. *Z. Anorg. Allg. Chem.* **2000**, *626*, 1519.

[23] Logvinovich, D.; Bocher, L.; Sheptyakov, D.; Figi, R.; Ebbinghaus, S. G.; Aguiar, R.; Aguirre, M. H.; Reller, A.; Weidenkaff, A. Microstructure, surface composition and chemical stability of partly ordered $LaTiO_2N$. Solid State Sci. **2009**, *11*, 1513.

[24] Clark, L.; Oró-Solé, J.; Knight, K. S.; Fuertes, A.; Attfield, J. P. Thermally Robust Anion-Chain Order in Oxynitride Perovskites. *Chem. Mater*. **2013**, *25*, 5004.

[25] Yang, M.; Oró-Solé, J.; Rodgers, J. A.; Jorge, A. B.; Fuertes, A.; Attfield, J. P. Anion order in perovskite oxynitrides. *Nat. Chem.* **2011**, *3*, 47.

[26] Porter, S. H.; Huang, Z.; Cheng, Z.; Avdeev, M.; Chen, Z.; Dou, S.; Woodward, P. M. Structural and magnetic properties of $RTiNO_2$ (R = Ce, Pr, Nd) perovskite nitride oxides. *J. Solid State Chem*. **2015**, *226*, 279.

[27] Caracas, R.; Cohen, R. E. Prediction of polar ordered oxynitride perovskites. *Appl. Phys. Lett*. **2007**, *91*, 1.

[28] Hinuma, Y.; Moriwake, H.; Zhang, Y.-R.; Motohashi, T.; Kikkawa, S.; Tanaka, I. First-Principles Study on Relaxor-Type Ferroelectric Behavior without Chemical Inhomogeneity in $BaTaO_2N$ and $SrTaO_2N$. *Chem. Mater*. **2012**, *24*, 4343.

[29] Fuertes, A. Chemistry and applications of oxynitride perovskites. *J. Mater. Chem.* **2012**, *22*, 3293.

[30] Attfield, J. P. Principles and Applications of Anion Order in Solid Oxynitrides. *Cryst. Growth Des.* **2013**, *13*, 4623.

[31] Ebbinghaus, S. G.; Abicht, H.-P.; Dronskowski, R.; Müller, T.; Reller, A.; Weidenkaff, A. Perovskite-related oxynitrides - Recent developments in synthesis, characterisation and investigations of physical properties. *Prog. Solid State Chem.* **2009**, *37*, 173.

[32] Clarke, S. J.; Hardstone, K. A.; Michie, C. W.; Rosseinsky, M. J. High-Temperature Synthesis and Structures of Perovskite and n =1 Ruddlesden-Popper Tantalum Oxynitrides. *Chem. Mater*. **2002**, *14*, 2664.

[33] Kresse, G.; Hafner, J. Ab. initio molecular dynamics for liquid metals. *Phys. Rev. B: Condens. Matter Mater. Phys.* **1993**, *47*, 558.

[34] Kresse, G.; Hafner, J. Ab initio molecular-dynamics simulation of the liquid-metal−amorphous-semiconductor transition in germanium. *Phys. Rev. B: Condens. Matter Mater. Phys.* **1994**, *49*, 14251.

[35] Kresse, G.; Furthmüller, J. Efficiency of ab-initio total energy calculations for metals and semiconductors using a plane-wave basis set. *Comput. Mater. Sci*. **1996**, *6*, 15.

[36] Kresse, G.; Furthmüller, J. Efficient iterative schemes for ab initio total-energy calculations using a plane-wave basis set. *Phys. Rev. B: Condens. Matter Mater. Phys.* **1996**, *54*, 11169.

[37] Blöchl, P. E. Projector augmented-wave method. *Phys. Rev. B: Condens. Matter Mater. Phys.* **1994**, *50*, 17953.

[38] Kresse, G.; Joubert, D. From ultrasoft pseudopotentials to the projector augmented-wave method. *Phys. Rev. B: Condens. Matter Mater. Phys.* **1999**, *59*, 1758.

[39] Perdew, J. P.; Burke, K.; Ernzerhof, M. Generalized Gradient Approximation Made Simple. *Phys. Rev. Lett.* **1996**, *77*, 3865.

[40] Porter, S. H.; Huang, Z.; Woodward, P. M. Study of Anion Order/Disorder in $RTaN_2O$ (R = La,

Ce, Pr) Perovskite Nitride Oxides. *Cryst. Growth Des.* **2014**, *14*, 117.

[41] Glazer, A. M. The Classification of Tilted Octahedra in Perovskites. *Acta Crystallogr., Sect. B: Struct. Crystallogr. Cryst. Chem.* **1972**, *B28*, 3384.

[42] Toroker, M. C.; Kanan, D. K.; Alidoust, N.; Isseroff, L. Y.; Liao, P.; Carter, E. A. First principles scheme to evaluate band edge positions in potential transition metal oxide photocatalysts and photoelectrodes. *Phys. Chem. Chem. Phys.* **2011**, *13*, 16644.

[43] Tasker, P. W. The stability of ionic crystal surfaces. *J. Phys. C: Solid State Phys.* **1979**, *12*, 4977.

[44] Huang, W. L. First-principles determination of the absolute band-edge positions of BiOX (X = F, Cl, Br, I). *Comput. Mater. Sci.* **2012**, *55*, 166.

[45] Ping, Y.; Rocca, D.; Galli, G. Electronic excitations in light absorbers for photoelectrochemical energy conversion: first principles calculations based on many body perturbation theory. *Chem. Soc. Rev.* **2013**, *42*, 2437.

[46] Heyd, J.; Scuseria, G. E.; Ernzerhof, M. Hybrid functionals based on a screened Coulomb potential. *J. Chem. Phys*. **2003**, *118*, 8207.

[47] Heyd, J.; Scuseria, G. E.; Ernzerhof, M. Erratum: "Hybrid functionals based on a screened Coulomb potential." *J. Chem. Phys*. **2006**, *124*, 219906.

[48] Paier, J.; Marsman, M.; Hummer, K.; Kresse, G.; Gerber, I. C.; Angyan, J. G. Screened hybrid density functionals applied to solids. *J. Chem. Phys*. **2006**, *125*, 249901.

[49] Perdew, J. P.; Levy, M. Physical Content of the Exact Kohn-Sham Orbital Energies: Band Gaps and Derivative Discontinuities. *Phys. Rev. Lett*. **1983**, *51*, 1884.

[50] Balaz, S.; Porter, S. H.; Woodward, P. M. Electronic Structure of Tantalum Oxynitride Perovskite Photocatalysts. *Chem. Mater.* **2013**, *25*, 3337.

[51] Restrepo, O. D.; Varga, K.; Pantelides, S. T. First-principles calculations of electron mobilities in silicon: Phonon and Coulomb scattering. *Appl. Phys. Lett*. **2009**, *94*, 212103.

[52] Bernardi, M.; Vigil-Fowler, D.; Lischner, J.; Neaton, J. B.; Louie, S. G. Ab Initio Study of Hot Carriers in the First Picosecond after Sunlight Absorption in Silicon. *Phys. Rev. Lett.* **2014**, *112*, 257402.

[53] Lautenschlager, P.; Allen, P. B.; Cardona, M. Phonon-induced lifetime broadenings of electronic states and critical points in Si and Ge. *Phys. Rev. B: Condens. Matter Mater. Phys.* **1986**, *33*, 5501.

[54] Kim, Y.-I.; Paik, Y. Bond covalency in perovskite oxynitrides $ATaO_2N$ (A = Ca, Sr, Ba) studied by ^{14}NMR spectroscopy. *Solid State Sci*. **2012**, *14*, 580.

[55] Fuertes, A. Metal oxynitrides as emerging materials with photocatalytic and electronic properties. *Mater. Horiz.* **2015**, *2*, 453.

Chapter 4.
Effects of Octahedral-Tilting and Crystal Polymorphism: A Demonstration on $MgTaO_2N$

4-1. Revisiting the structural model of $MgTaO_2N$: a theoretically predicted photocatalyt

4-1-1. Computational material search in the research area of photocatalyts

Recently, with the impressively enhanced availability of computational resources, computational screening of novel materials of technological relevance has become an extremely powerful procedure to predict the possible existence of yet unexplored materials. For instance, Ceder *el al.* succeeded in finding a novel compound that can be used as a cathode material for lithium batteries with a superior voltage and a lower cost, using first-principle calculations on several possible candidates [1]. There also exist other cases for high stability alloys [2], piezoelectrics [3], organic photovoltaics [4, 5] and inorganic scintillator materials [6], all of which demonstrate the benefits of recent computational material search.

Such studies using computational screenings have also been adopted to the material search for photocatalysts [7-9]. For perovskite-type oxynitrides of formula ABO_2N, a screening procedure on thermodynamic and electronic properties (bandgap and band edge position) initially involving 2704

compounds has revealed four well established and investigated materials, $CaTaO_2N$ [10,11], $SrTaO_2N$ [10], $BaTaO_2N$ [10,12,13], $LaTiO_2N$ [14] and a new one, *i.e.* $MgTaO_2N$, as promising candidates for photocatalysis [9].

4-1-2. Possible octahedral-tilting and crystal polymorphism in $MgTaO_2N$

However, with the enormous computational cost in mind, modeling of the compounds just in terms of thermodynamic stability and band edge positions may result not sufficient and a more detailed analysis is mandatory in order to shed light on the photocatalytic features of such materials.

The first issue, indeed, is the oversimplified structural model used in the screening procedure: perovskite oxynitrides denoted by ABO_2N were all considered in their cubic polymorph whose unit cell consists of only five atoms, and thus structural features, such as rotation of the octahedral unit TaO_4N_2 (octahedral-tilting [15], as illustrated in Figure 4-1) and characteristic anionic distribution (anion ordering [16], as explained in chapter 3) in the perovskite crystals were not taken into account. These structural factors are known to impact on the structures of both conduction [17,18] and valence bands [19], respectively, and thus they need to be considered in modeling and calculating the properties of $MgTaO_2N$.

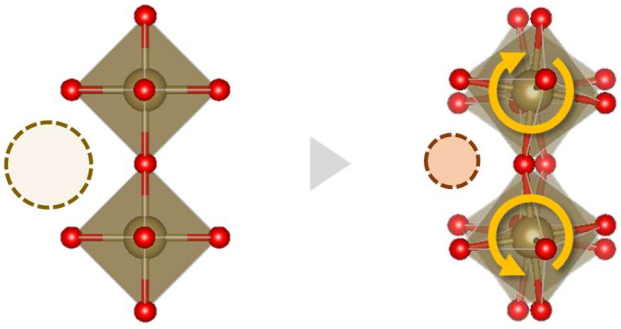

Figure 4-1. Schematic illustration of the octahedral-tilting in perovskites where the dashed circles correspond to A-site cations.

The second issue is that only perovskite-type $MgTaO_2N$ was structurally modeled and other polymorphs have not been considered. Generally, a compound with the chemical formula ABX_3 assumes the perovskite structure only when its tolerance factor *t* (reported in Eq (4.1)) is close to one [20,21].

$$t = \frac{r_A + r_X}{\sqrt{2}(r_B + r_X)} \quad (4.1)$$

where r_i (i = A, B, X) is the ionic radius of the three species. However, compared to the A site cation of previously reported tantalum oxynitrides such as Ca^{2+}, Sr^{2+}, and Ba^{2+}, the ionic radius of Mg^{2+} is clearly smaller and thus $MgTaO_2N$ is characterized by crystal structures other than perovskite [22]. Since the ionic radii of the $MgTaO_2N$ constituents (Ta^{5+}: 0.64 Å, O^{2-}: 1.38 Å, N^{3-}: 1.46 Å [23]) are quite similar to those of $MgTiO_3$ [24, 25] (Ti^{4+}: 0.605 Å, O^{2-}: 1.38 Å [26]) which has ilmenite structure, $MgTaO_2N$ is expected to have the same crystal structure. To confirm such idea, using the following ionic radii, *i.e.* for O^{2-} 1.38, for N^{3-} 1.46, for Mg^{2+} 0.72, and for $Ti^{4.5+}$ 0.66 Å (in this case the algebraic average between +4 and +5 oxidation number of Ta was considered), value for t = 0.73 was obtained, which further supports the stability of the ilmenite–like polymorph for $MgTaO_2N$. Therefore, not only perovskite but also ilmenite has to be taken into account in order to fully predict the photocatalytic properties of $MgTaO_2N$ from first principles.

4-1-3. Objective of this work

Here, in this study, I aim to disclose the properties of $MgTaO_2N$ considering octahedral-tilting, anion ordering, and the interplay between perovskite and ilmenite polymorphs, and thereby discussing its applicability as material for photocatalysis. In particular, photocatalyst related properties such as bandgaps, band edge positions, and carrier effective masses of $MgTaO_2N$ will be calculated from first principles. Then, a brief outline for $MgTaO_2N$ material design as a novel photocatalyst will be provided by identifying the factors that impact on each property.

4-2. Computational details

4-2-1. Structural models

The initial structure of perovskite-type $MgTaO_2N$ (hereafter also *p*-$MgTaO_2N$) is modeled by imposing the crystal coordinates of $CaTaO_2N$ [27], whose unit cell has the space group *Pnma*, replacing Ca atoms with Mg ones. Since $CaTaO_2N$ already has intrinsic octahedral-tilting of TaO_4N_2, that of $MgTaO_2N$ was successfully modeled by imposing the former coordinates as the initial ones for the latter structure. For *p*-$MgTaO_2N$, 13 different anion orderings (hereafter also *aor*s) were prepared, from A1 to F4 as shown in Figure 3-1. in chapter 3, similarly to our previous analysis on the *aor*s of $CaTaO_2N$ [19].

The initial structure of ilmenite-type $MgTaO_2N$ (hereafter also *i*-$MgTaO_2N$) derives from the rhombohedral unit cell of $MgTiO_3$ with space group $R\bar{3}$ [24], initially modeled replacing Ti atoms with Ta ones and one third of O atoms with N ones. Also, two different anion distributions, *cis* and *trans* (see Figure 4-2), were modeled in order to relate the electronic properties with its anion ordering.

Density functional theory, as implemented in the VASP code [28-31], was employed in order to geometrically relax the initial structures. On top of the optimized geometries the electronic properties were calculated. The convergence was considered achieved once the forces on individual atoms were smaller than 0.01 eV/Å. The Brillouin Zone (BZ) was sampled with a 10 × 7 × 10 *Γ*-centered mesh for *p*-$MgTaO_2N$ and with a 11 × 11 × 4 one for *i*-$MgTaO_2N$. In particular, the GGA-

PBE exchange correlation functional [32] and the projected augmented wave (PAW) method [33, 34] were employed, along with an energy cutoff for the plane wave of 500 eV.

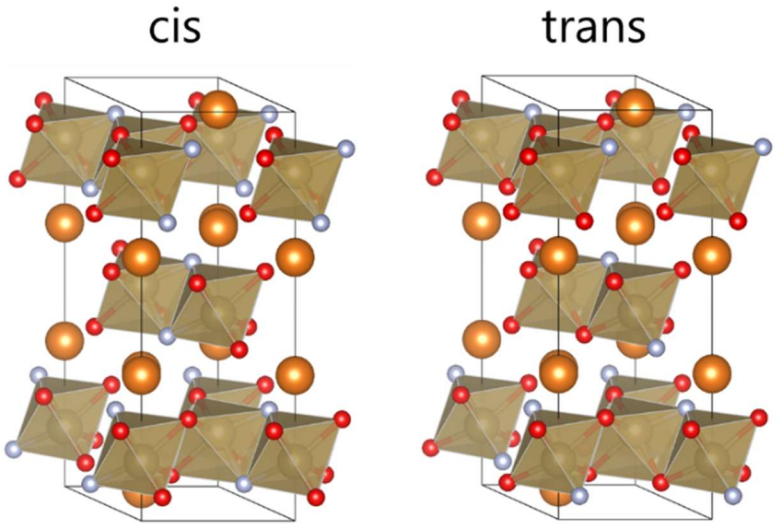

Figure 4-2. Initial structures of *i*-$MgTaO_2N$ with two anion distributions. Brown: tantalum, red: oxygen, blue: nitrogen, orange: magnesium.

4-2-2. Calculation conditions

In order to discuss the fundamental photocatalytic properties of both *p*-$MgTaO_2N$ and *i*-$MgTaO_2N$, I have calculated bandgaps (E_g), carrier effective masses, and band edge positions. Electronic properties were calculated on the optimized structures of both polymorphs, with a 12 × 9 × 12 (*p*-$MgTaO_2N$) and a 13 × 13 × 5 (*i*-$MgTaO_2N$) mesh of the BZ, until the difference in the total free energy between two consecutive steps was lower than 10^{-5} eV. Besides, HSE06 hybrid functional [35] was also applied to compensate the methodological underestimation of the electronic properties in the pure-DFT calculations.

Bandgaps were approximated as the Kohn-Sham ones, and carrier effective masses were estimated using band dispersions (see Eq (3.1) and (3.2) in chapter 3). Band edge positions were estimated as the orbital energies referenced to the vacuum potential [36] that was calculated by means of a slab approach. As already pointed in the previous studies, the calculated value of the vacuum potential strongly depends on the surface structure of the slab model [37]. Therefore, similarly to our previous study on $CaTaO_2N$, only one slab model was used to calculate the vacuum potential and define the “effective” vacuum potentials of the other anion orders by assuming that the potential of the bulk model equals that of the bulk region of the slab model [19] (see also Eq. (3.4) to (3.6) in chapter 3).

To calculate the vacuum potential, a slab model with zero net dipole along the normal to the

slab surface was used. The thickness of the vacuum region was set to 19 Å on all slab models in order to prevent Coulomb interactions among replicas of the slab along the same direction [36, 38], while the thickness of the slabs was set to 30 Å (= six-unit layers) on *p*-$MgTaO_2N$ and 42 Å (= three-unit layers) on *i*-$MgTaO_2N$. I have considered six slab models for *p*-$MgTaO_2N$ (Figure 4-3) and two slab models for *i*-$MgTaO_2N$ (Figure 4-4) and adopted that with the smallest surface energy as calculated from Eq (3.3) in chapter 3. All the ionic positions of each slab were fully relaxed with a 4 × 4 × 1 Γ–centered sampling of the BZ until the forces on single atoms were smaller than 0.05 eV/Å. On the optimized structures, electronic calculations were performed with a 4 × 6 × 1 Γ-centered sampling of the BZ on the slab models of *p*-$MgTaO_2N$ and a 6 × 6 × 1 Γ-centered sampling of the BZ for *i*-$MgTaO_2N$ with a total free energy convergence criterion of 10^{-4} eV. For all the slab models the potential of the vacuum region was converged and the bandgaps at the bulk regions reproduced those of the corresponding bulk models within 0.12 eV. The surface energies and the bandgaps of each slab model are listed on Table 4-1.

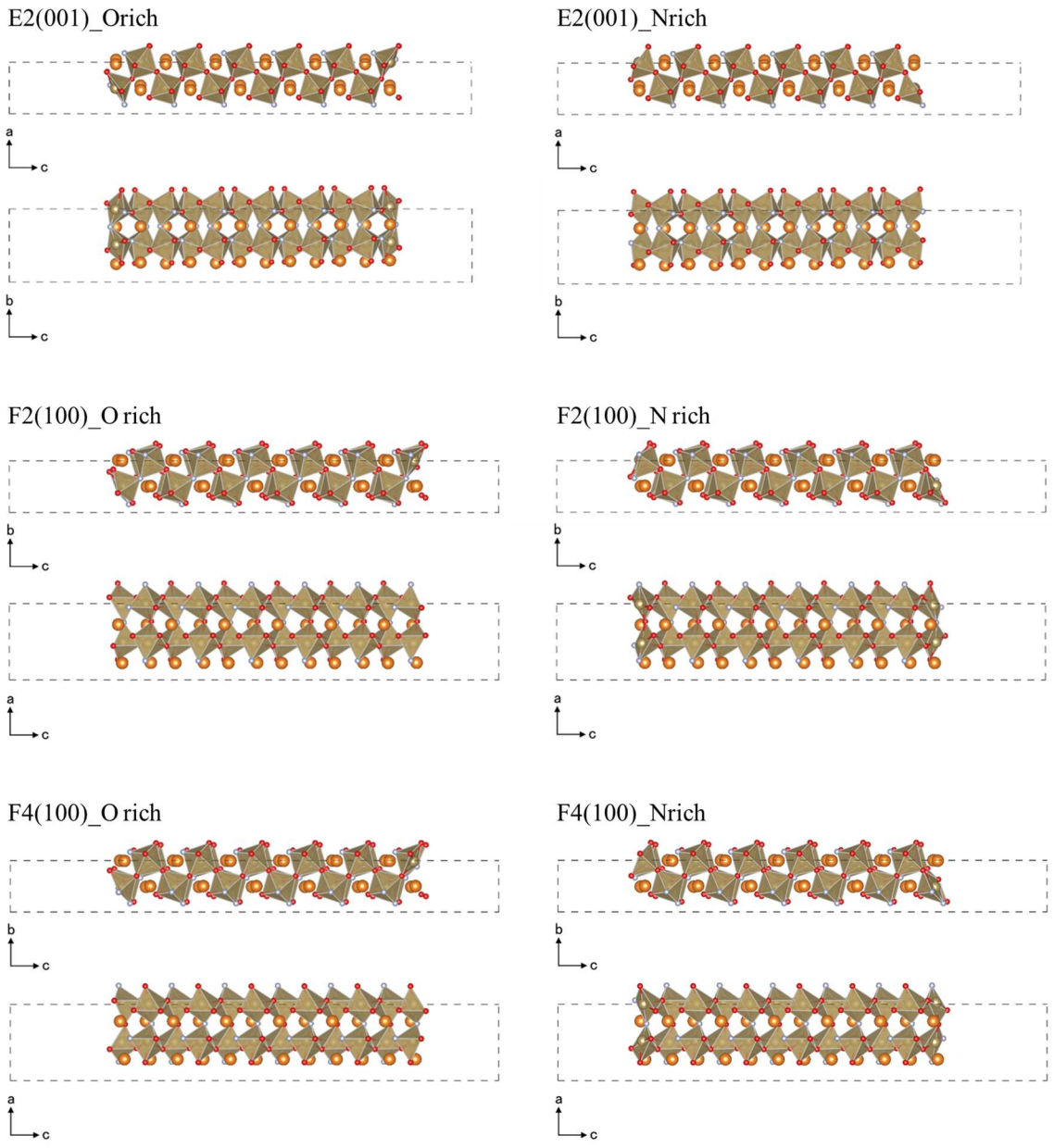

Figure 4-3. Unit cells of each slab models for *p*-$MgTaO_2N$. Three-types of slab models E2(001), F2(100), F4(100) were prepared as non-polar ones. O-rich and N-rich surface were considered on each slab model: 6 slab models were used. Accordingly, F2(100) with O-rich surface (the smallest surface energy) was adopted in the vacuum level calculation.

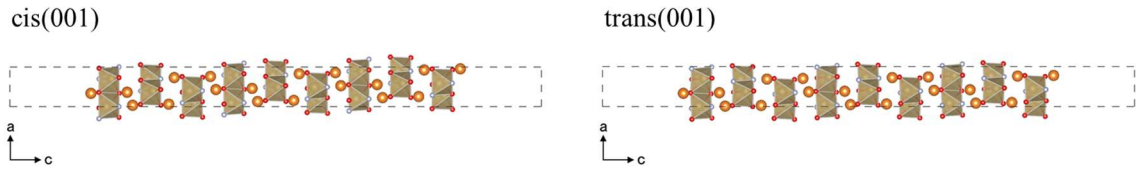

Figure 4-4. Unit cells of each slab models for *i*-$MgTaO_2N$, two slab models, *cis*- and *trans*-(001), were prepared as non-polar ones, adopting the former in the vacuum level calculation.

Table 4-1. Surface energies and bandgaps calculated using each slab model. All the bandgaps in this table are calculated at DFT-PBE level of theory.

	E_{surf} [mJ/m^2]	E_g (slab) [eV]	E_g [eV]
***p*-$MgTaO_2N$**			
E2(001)_Orich	1055.7	2.37	2.25
E2(001)_Nrich	1250.9	2.29	2.25
F2(100)_Orich	1030.5	2.78	2.66
F2(100)_Nrich	1491.8	2.68	2.66
F4(100)_Orich	1180.6	2.95	2.95
F4(100)_Nrich	1406.6	3.02	2.95
***i*-$MgTaO_2N$**			
cis(001)	839.5	3.13	3.05
trans(001)	846.2	2.95	3.02

4-3. Impacts of octahedral-tilting

Structural parameters, bandgaps, and carrier effective masses of each *p*-$MgTaO_2N$ *aor*s are listed in Table 4-2. Compared to the initial structures *i.e.*, those of $CaTaO_2N$, as previously mentioned, lattice parameters are shorter by ~1-5 %, while bond angles ∠Ta-X-Ta (X = O, N) are narrower by ~12-15°. On the other hand, their bond lengths $r_{\mathrm{Ta-N}}$ and $r_{\mathrm{Ta-O}}$ remain almost unaltered, proving that the octahedral-tilting increases in *p*-$MgTaO_2N$, compared to $CaTaO_2N$.

Bond angles ∠Ta-X-Ta (X = O, N) of *p*-$MgTaO_2N$ also vary among different *aor*s: they differ up to 2.2°, proving that the magnitude of octahedral-tilting also depends on the *aor*s. Bond angles ∠Ta-X-Ta of A~B2, E2, and E3 are smaller than the average bond angles of all *aor*s (137.7°), while those of the remaining ones, *i.e.,* C, D, E1, F1~F4 are larger than the same average value. Thus, I will refer to the former *aor*s as "*less-tilted*" and to the latter as "*more-tilted*".

For all *aor*s, average bond angles ∠Ta-N-Ta are always larger than ∠Ta-O-Ta ones, while average bond lengths $r_{\mathrm{Ta-N}}$ are always shorter than $r_{\mathrm{Ta-O}}$ ones, in clear contrast with the order of the ionic radius of N^{3-} and O^{2-}. Additionally, most of the adjacent Ta-X bonds, *i.e.,* Ta-X-Ta (X=O, N) differ by ~0.1 Å in average, as illustrated in Figure 4-5. Such structural characteristics can be explained by assuming the existence of a partial covalent nature of the Ta-X bond mainly associated with a *d-p* π interaction [39-42]. Nitrogen reduced electronegativity – compared to oxygen –enhances the covalent nature of the Ta-N bond *vs* Ta-O bond, also resulting in bond angle opening and shortening

Table 4-2. Structural parameters, bandgaps, and carrier effective masses of each *p*-$MgTaO_2N$ *aor*s.

	Lattice parameters (Ang)			Bond angles (deg)			Bond length (Ang)						
	a	b	c	∠Ta-X-Ta	∠Ta-O-Ta	∠Ta-N-Ta	$r_{Ta\text{-}O}$	$r_{Ta\text{-}N}$	$\Delta r_{Ta\text{-}O}$	$\Delta r_{Ta\text{-}N}$	E_g (eV)	m_e^*	m_h^*
A1	5.46	7.74	5.28	138.5	137.5	140.5	2.08	1.98	0.01	0.01	3.20	0.87	1.10
A2	5.47	7.73	5.30	138.5	137.1	141.4	2.09	1.97	0.04	0.02	2.61	0.68	0.82
B1	5.47	7.74	5.29	138.4	138.1	139.0	2.09	1.96	0.05	0.03	3.10	0.66	1.38
B2	5.45	7.75	5.29	138.6	135.7	144.3	2.08	1.98	0.08	0.02	3.11	0.73	1.31
C	5.43	7.79	5.27	137.1	135.4	140.4	2.09	1.99	0.12	0.10	3.70	2.87	2.08
D	5.44	7.80	5.28	136.9	134.8	141.1	2.10	1.99	0.16	0.15	3.64	1.44	0.84
E1	5.43	7.78	5.27	137.0	135.5	140.0	2.09	1.99	0.12	0.10	3.65	1.18	1.99
E2	5.45	7.75	5.28	138.4	137.1	140.9	2.08	1.98	0.04	0.05	3.31	0.93	1.53
E3	5.47	7.73	5.29	138.5	136.6	142.4	2.08	1.98	0.07	0.05	3.26	0.85	1.35
F1	5.46	7.77	5.28	137.6	136.7	139.3	2.10	1.98	0.16	0.11	3.63	2.24	1.30
F2	5.44	7.80	5.28	137.1	135.8	139.6	2.10	1.98	0.17	0.11	3.80	1.07	1.20
F3	5.46	7.77	5.28	137.6	136.7	139.4	2.09	1.98	0.15	0.11	3.62	1.19	1.42
F4	5.43	7.80	5.27	136.4	133.8	141.6	2.10	1.99	0.16	0.18	4.13	1.79	1.84
Ave	**5.45**	**7.77**	**5.28**	**137.7**	**136.2**	**140.8**	**2.09**	**1.98**	**0.10**	**0.08**	**3.44**	**1.27**	**1.40**
Initial	**5.62**	**7.90**	**5.55**		**153.9 (average)**			**2.03 (average)**		--	--	--	--

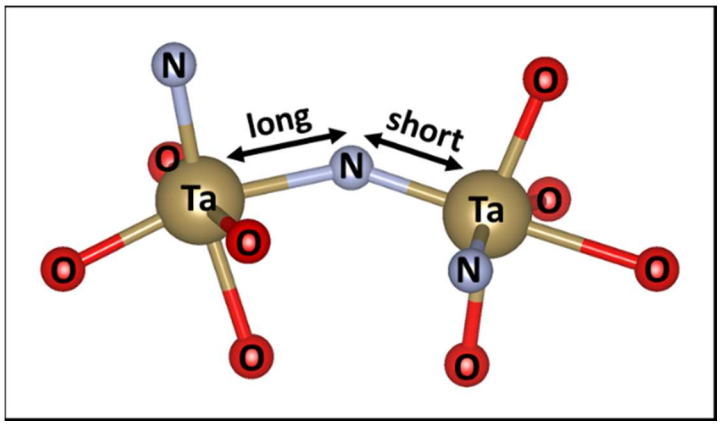

Figure 4-5. Asymmetric bond lengths between the consecutive Ta-N bonds.

the bond lengths.

The magnitude of *d-p* π interaction can be described as the difference between the two bond lengths that connect X anion and Ta, *i.e.*, $\Delta r_{\mathrm{Ta-O}}$ and $\Delta r_{\mathrm{Ta-N}}$. These values differ among the *aor*s and interestingly correlate with the bond angles ∠Ta-X-Ta (see Figure 4-6) showing that the more tilted the octahedron the larger the Ta-X *d-p* π interaction.

The octahedral-tilting also impacts on bandgaps. Those of *p*-$MgTaO_2N$ are more open, ranging from 2.6 eV to 4.1 eV, than those of analogous oxynitrides such as $BaTaO_2N$ (2.0 eV), $SrTaO_2N$ (2.1 eV), and $CaTaO_2N$ (2.5 eV) [9] whose octahedral-tilting is rather small. Besides, in our case *more-tilted aor*s shows much larger bandgaps. Both trends suggest the non-negligible positive correlation between bandgaps and octahedral-tilting.

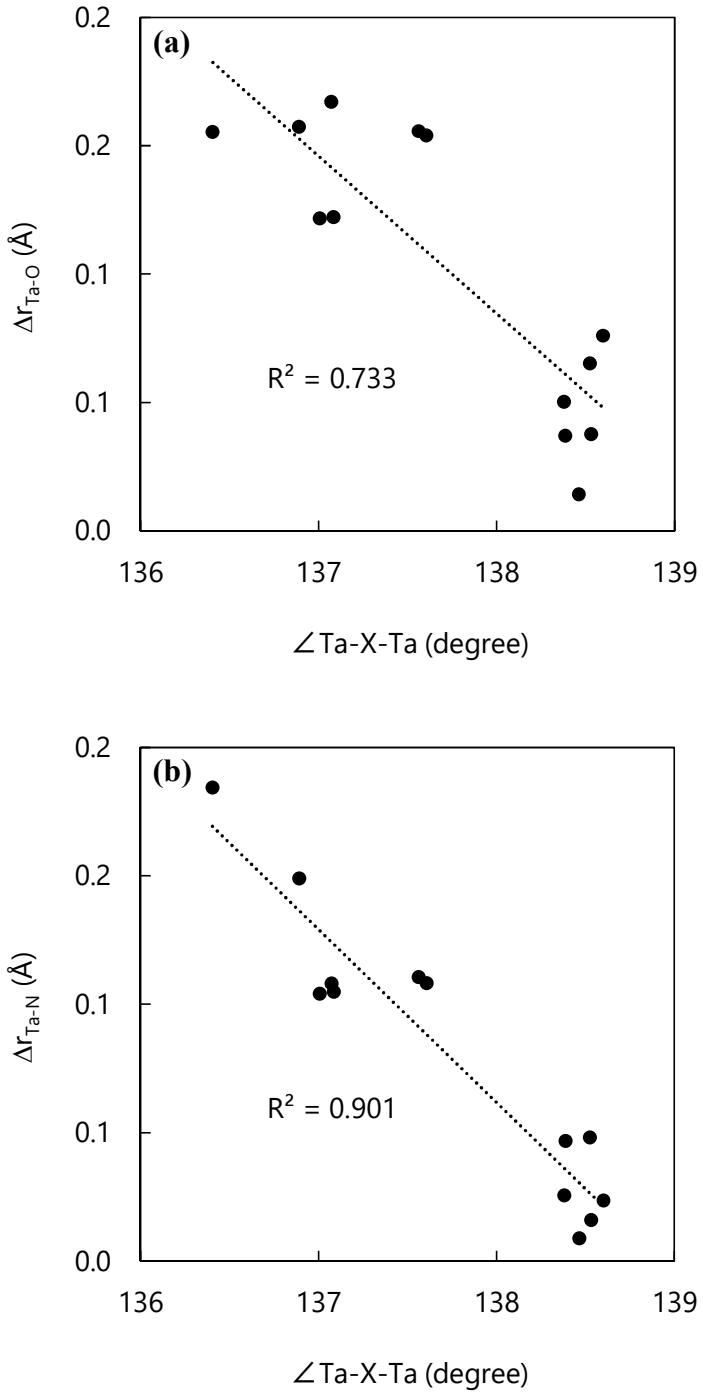

Figure 4-6. Correlation between bond angles (∠Ta-X-Ta) and bond lengths differences in (a) Ta-O bond ($\Delta r_{\mathrm{Ta-O}}$) and (b) Ta-N bond ($\Delta r_{\mathrm{Ta-N}}$). $\Delta r_{\mathrm{Ta-O}}$ and $\Delta r_{\mathrm{Ta-N}}$ shows the larger value when ∠Ta-X-Ta is rather small, indicating the increase of the covalent interaction.

The calculated carrier effective mass of *p*-$MgTaO_2N$ also indicates the strong relation between octahedral-tilting and the band dispersion, especially in the conduction region. For *p*-$MgTaO_2N$, electron effective mass of m_e^* range between 0.66 to 2.87 m_0 (1.27 m_0 in average) while the hole effective mass m_h^* between 0.82 and 2.08 m_0 (1.40 m_0 in average). Electron and hole effective masses of *p*-$MgTaO_2N$ compared to those of $CaTaO_2N$ are shown in Figure 4-7 and 4-8, respectively. Compared to the effective mass of $CaTaO_2N$ (m_e^*: 0.63 m_0 in average, m_h^*: 1.75 m_0 in average) [19], electron effective masses of *p*-$MgTaO_2N$ are quite larger, while its hole effective masses are rather similar. In addition, the bond angles ∠Ta-X-Ta (X = O, N) of *p*-$MgTaO_2N$ strongly correlate with the electron effective mass, while negligible correlation is observed with the hole effective mass, as shown in Figure 4-9. Thus, the picture that emerges from our analysis is that the octahedral-tilting mainly impacts on the structures of conduction bands (CBs).

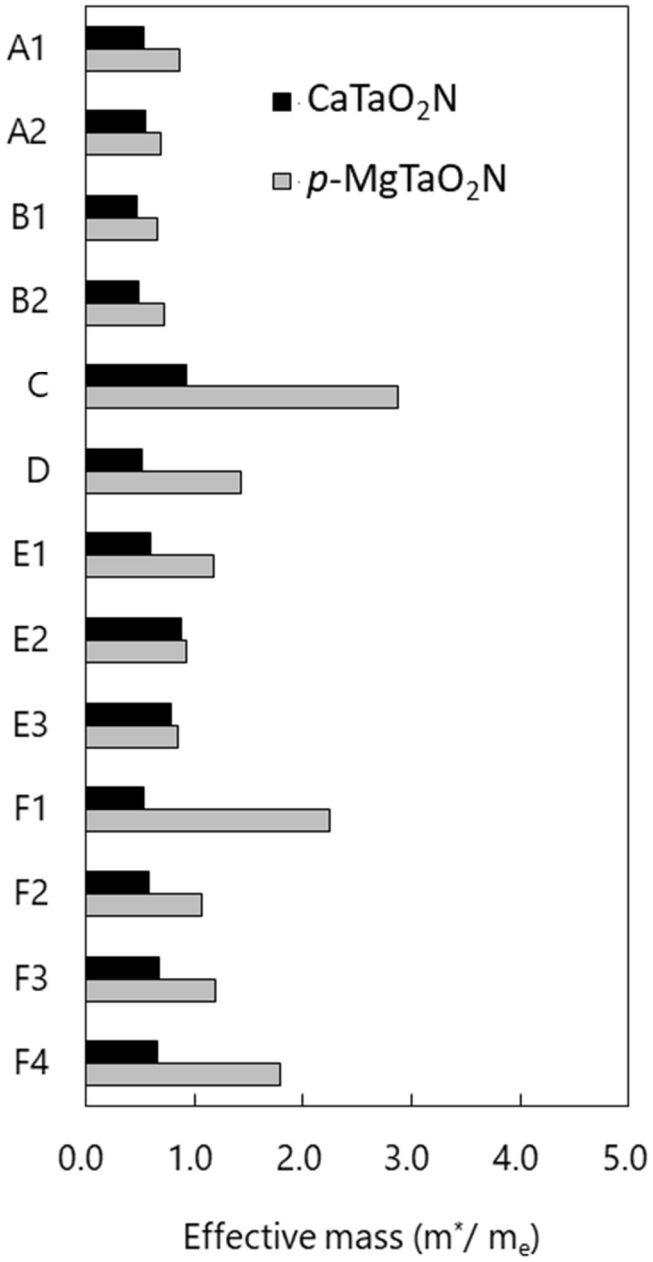

Figure 4-7. Electron effective masses of *p*-$MgTaO_2N$ compared to $CaTaO_2N$.

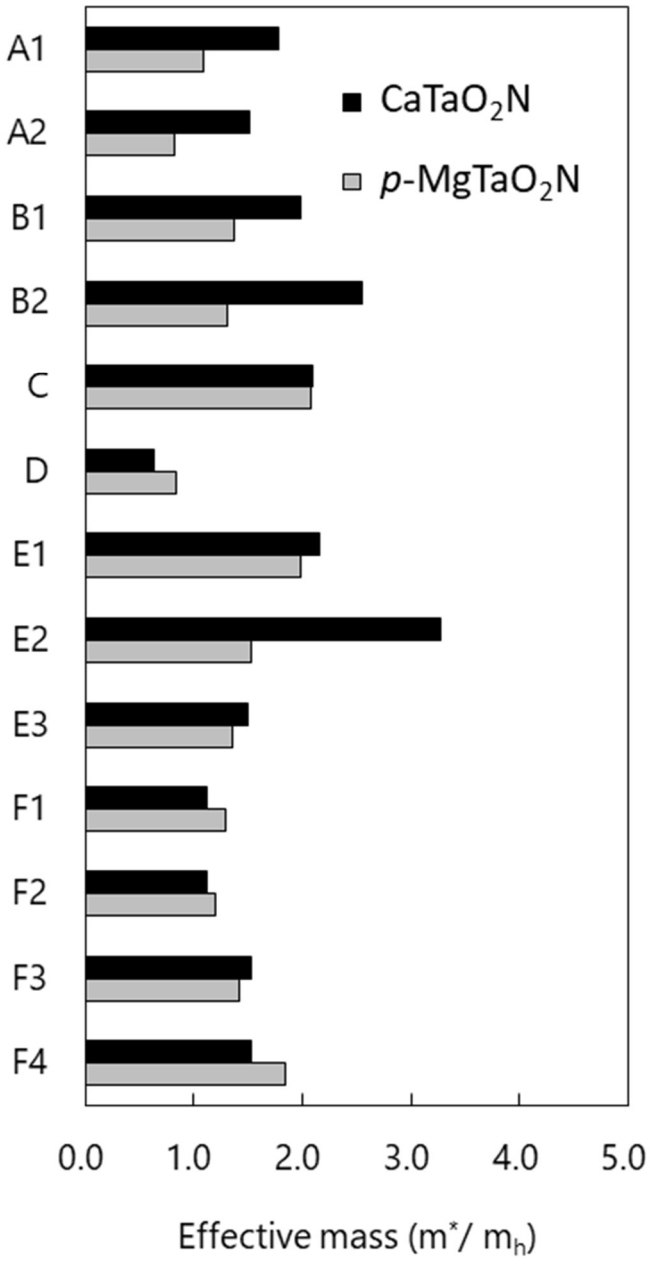

Figure 4-8. Hole effective masses of *p*-$MgTaO_2N$ compared to $CaTaO_2N$.

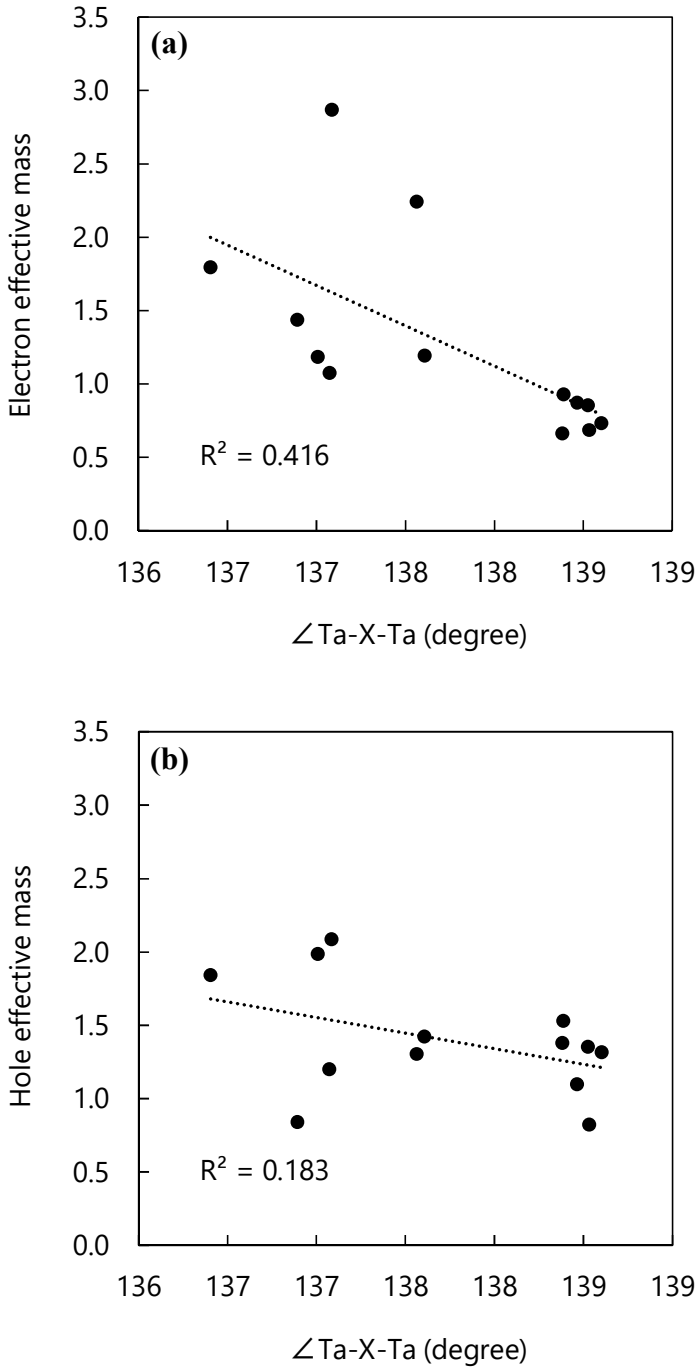

Figure 4-9. Correlation between bond angles (∠Ta-X-Ta) and carrier effective mass of (a) electrons and (b) holes.

The correlation between octahedral-tilting and the CB structures are also confirmed by the *p*-$MgTaO_2N$ band edge positions reported in Figure 4-10 for different *aor*s, with VBMs lying between +1.16 V_{NHE} and +2.10 V_{NHE}, while CBMs between -1.45 V_{NHE} and -2.04 V_{NHE}, most of which straddle the water redox potentials. As shown in Figures 4-11 (a) and (b), CBM positions are strongly correlated with the ∠Ta-X-Ta bond angles, while VBM positions only slightly do it. All these results show that the octahedral-tilting is the main factor for the different CBM positions among the *aor*s.

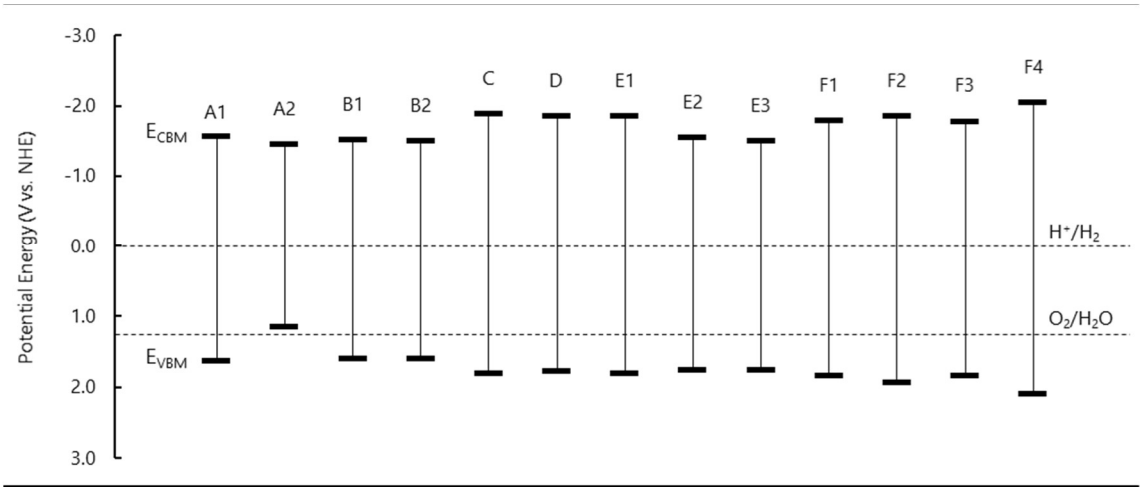

Figure 4-10. Band edge positions of *p*-$MgTaO_2N$. The vertical axis was set to the normal hydrogen electrode (NHE) potential.

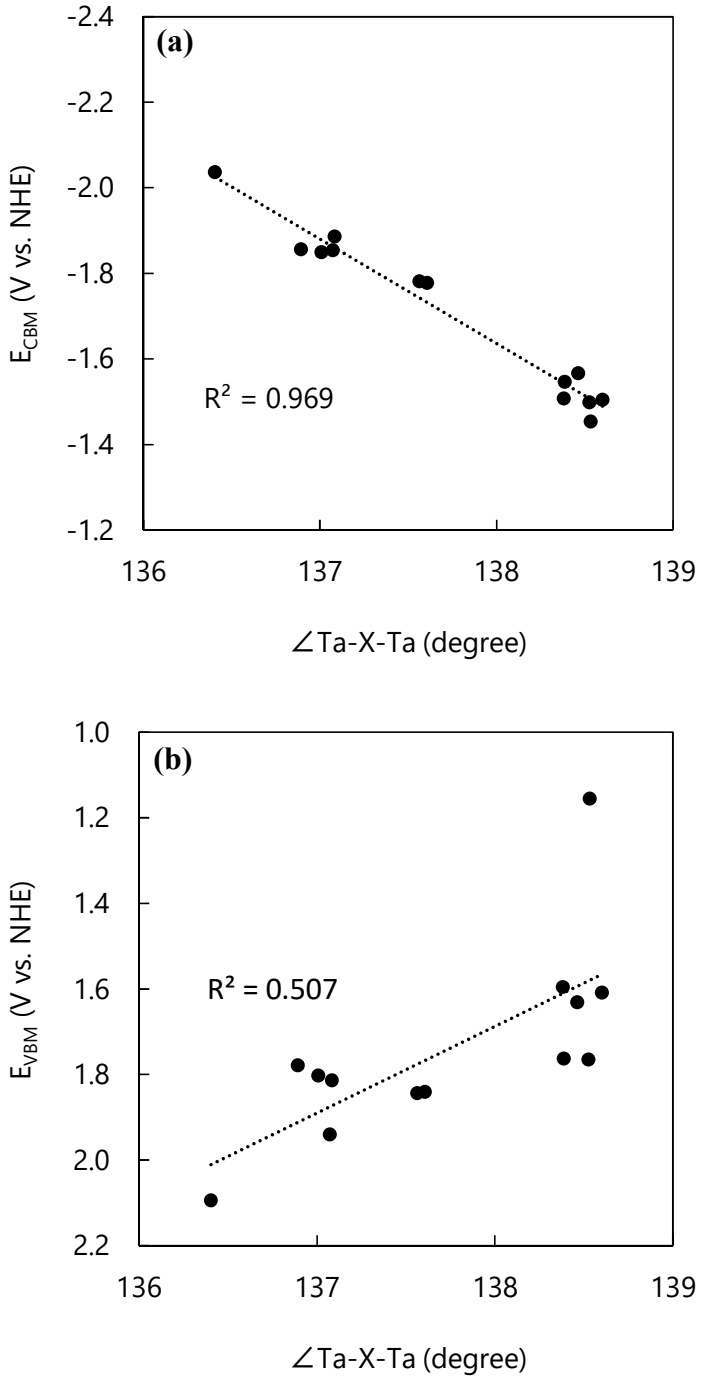

Figure 4-11. (a) Correlation between bond angles (∠Ta-X-Ta) and CBM positions. (b) Correlation between bond angles (∠Ta-X-Ta) and VBM positions.

The difference in CB electronic structures is also observed in the Density of States (DOS) and Projected Density of States (PDOS) of *p*-$MgTaO_2N$, reported in Figure 4-12. CB dispersions of *less-tilted aor*s *i.e.,* A1~B2, E2, and E3, are relatively smooth, while those of *more-tilted* ones are sharp. Besides, the bottom regions of the CBs of the formers mainly consist of Ta 5d, while additional contribution of O 2p is observed in the same regions of the latter ones. These characteristics indicate that the uplift of the CBM positions with the increasing octahedral-tilting originates from the band dispersion reduction that is caused by the *d-p* π interaction between Ta 5d and O 2p in the CBs. Similar trends are also reported in previous report by Eng *et al.* [17], where the relation between the band dispersion reduction together with the octahedral-tilting increase are ascribed to the increase of the antibonding character at the CBM.

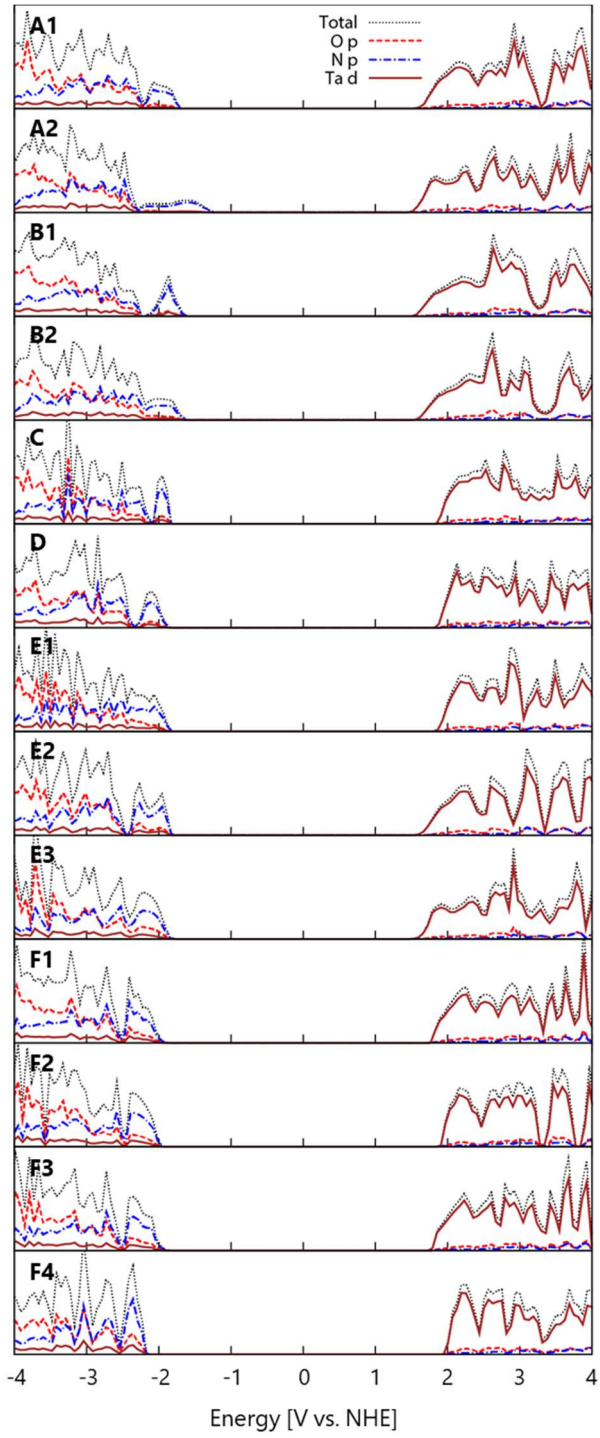

Figure 4-12. DOS and PDOS of *p*-$MgTaO_2N$. Their energy positions are aligned with the band edge positions depicted in Figure 4-10. Black dotted line: total DOS, Red dashed line: O 2p, Blue dashed line: N 2p, Brown solid line: Ta 5d.

Now, based on the results above, the possible applicability and the material design guidelines of *p*-$MgTaO_2N$ can be discussed as follows.

First, as mentioned in the previous section, most of the *p*-$MgTaO_2N$ configurations have suitable band edge positions for overall water splitting, since their VBM positions are lower than the OER potential and CBM positions are higher than the HER potential. In particular, larger potential differences between CBM positions and HER potential are fingerprint of their strong tendency towards the HER. Nevertheless, their bandgaps are still larger than the energy of visible light, except for A2, whose VBM does not exceed the oxygen evolution potential.

Accordingly, the bandgaps of *p*-$MgTaO_2N$ should be reduced mainly modifying their CBM positions. As demonstrated in the previous section, CBM positions are strongly correlated with octahedral-tilting of *p*-$MgTaO_2N$ *i.e.,* the suppression of the tilting would lead to a CBM reduction. Furthermore, these *less-tilted p*-$MgTaO_2N$ are also promising as water splitting photocatalyts since the electron effective mass diminishes as the octahedral-tilting decreases, as reported in Figure 4-9. Therefore, a modified, tilting reduced *p*-$MgTaO_2N$, is highly desirable: doping/alloying by replacing Mg^{2+} with different cations whose ionic radii is larger than Mg^{2+} will reduce the octahedral-tilting in *p*-$MgTaO_2N$ offering suitable band structures for visible light driven water splitting.

4-4. Impacts of crystal polymorphism

Structural parameters, bandgaps, and carrier effective masses of each *i*-$MgTaO_2N$ are reported on Table 4-3. Their formation energies were also compared to that of *p*-$MgTaO_2N$ in the most stable *aor*, and it was found that they are more stable by 249 meV/FU and 174 meV/FU in *cis* and *trans* arrangement, respectively.

In both *i*-$MgTaO_2N$, average bond lengths $r_{\mathrm{Ta-N}}$ are always shorter than r_{Ta-O}, like in *p*-$MgTaO_2N$, confirming the existence of a partial covalent nature of the bond in such class of compounds. In this case, at variance with the *p*-$MgTaO_2N$, adjacent Ta–X bond lengths *i.e.*, Ta–X–Ta (X = O, N), are extremely different. Such differences ($\Delta r_{\mathrm{Ta-X}}$, X = O, N) were more than twice larger than the same in *p*-$MgTaO_2N$, and thus the enhanced covalent nature, that is, the enhanced overlap between tantalum and anion orbitals, are even larger in *i*-$MgTaO_2N$. Such difference between the two polymorphs is ascribed to their different bond angles ∠Ta-X-Ta (X = O, N). In *p*-$MgTaO_2N$, the overlap between Ta 5d and anion 2p is much hindered, since there is essentially a symmetry mismatch between such orbitals when they are in linear fashion [17,19] while the reduced bond angles in *i*-$MgTaO_2N$ diminish the symmetry mismatch and thus lead to the enhanced overlap.

Bandgaps of both *i*-$MgTaO_2N$ are larger than 4.2 eV, markedly larger than those of *p*-$MgTaO_2N$, with the material resulting a large gap semiconductor. Carrier effective masses are also larger in *i*-$MgTaO_2N$, most of which are over 3.0 m_0. Additionally, the band edge positions reveal

Table 4-3. Structural parameters, bandgaps, and carrier effective masses of each *i*-$MgTaO_2N$ geometry.

	Lattice parameters (Ang)			Bond angles (deg)			Bond lengths (Ang)						
	a	b	c	∠Ta-O-Ta	∠Ta-N-Ta	∠Ta-X-Ta	r_{Ta-O}	r_{Ta-N}	Δr_{Ta-O}	Δr_{Ta-N}	E_g (eV)	m_e^*	m_h^*
cis	5.33	5.33	14.38	99.4	94.3	97.7	2.12	1.99	0.26	0.16	4.28	3.01	1.62
trans	5.29	5.28	14.45	96.2	98.9	97.1	2.11	2.01	0.24	0.20	4.22	3.33	3.31
Ave	**5.31**	**5.31**	**14.42**	**97.8**	**96.6**	**97.4**	**2.11**	**2.00**	**0.25**	**0.18**	**4.25**	**3.17**	**2.47**

that *i*-$MgTaO_2N$ is unsuitable for both oxygen and hydrogen evolution reaction (OER and HER, respectively) according to their positioning towards the NHE (Figure 4-13). PDOS of *i*-$MgTaO_2N$ reported in Figure 4-14 shows that their VB top and CB bottom mainly consist of anion 2p and Ta 5d, respectively, as for *p*-$MgTaO_2N$. Nevertheless, for *i*-$MgTaO_2N$, Ta 5d contribution is also present in the top region of VBs, while that of O 2p and N 2p is similarly present in the bottom region of CBs. These results indicate that the overlap between Ta 5d and anion 2p occurs in both bands, similarly witnessing a reduced selectivity of the carriers with subsequent reduced applicability in devices for photoconversion. By comparing the DOS of *p*-$MgTaO_2N$ and *i*-$MgTaO_2N$, dispersions are clearly small in the latter one, and based on previous results, the *i*-$MgTaO_2N$ bandgap opening is ascribed to the band dispersion decrease which is consequence of the Ta-X interaction increase.

In addition to the increased interaction between Ta and X, the decrease of band dispersion in *i*-$MgTaO_2N$ is mainly related to the layered (2D) nature of the structures: in the crystal of *p*-$MgTaO_2N$, TaO_4N_2 octahedral units share their apices forming a 3D network, while they share their sides in the crystal of *i*-$MgTaO_2N$, thus resulting in a *quasi* 2D structure. As shown in Figure 4-15, the layered structures of *i*-$MgTaO_2N$ reduce their ionic density of both Ta cations and O, N anions compared to those of *p*-$MgTaO_2N$.

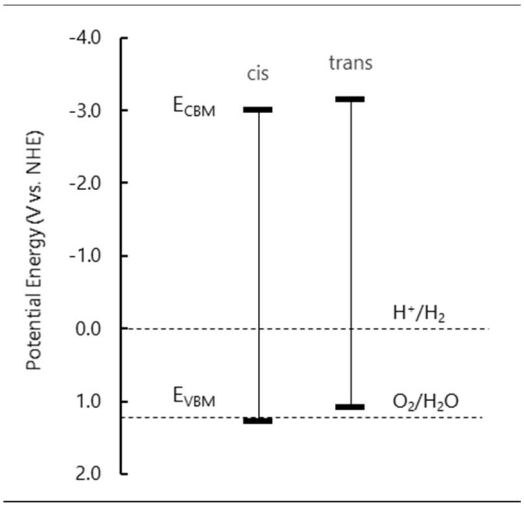

Figure 4-13. Band edge positions of *i*-$MgTaO_2N$. The vertical axis was set to the normal hydrogen electrode (NHE) potential.

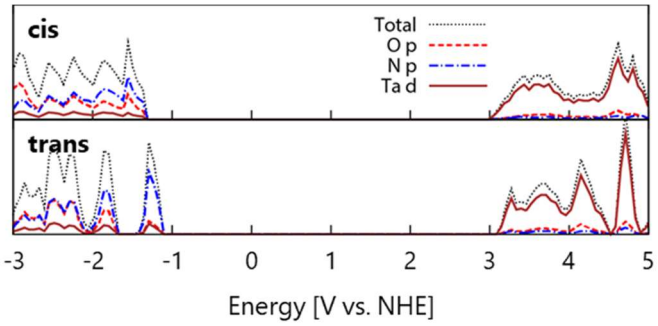

Figure 4-14. DOS and PDOS of *i*-$MgTaO_2N$. Their energy positions are in line with the band edge positions depicted in Figure 4-13. Black dotted line: total DOS, Red dashed line: O 2*p*, Blue dashed line: N 2*p*, Brown solid line: Ta 5*d*.

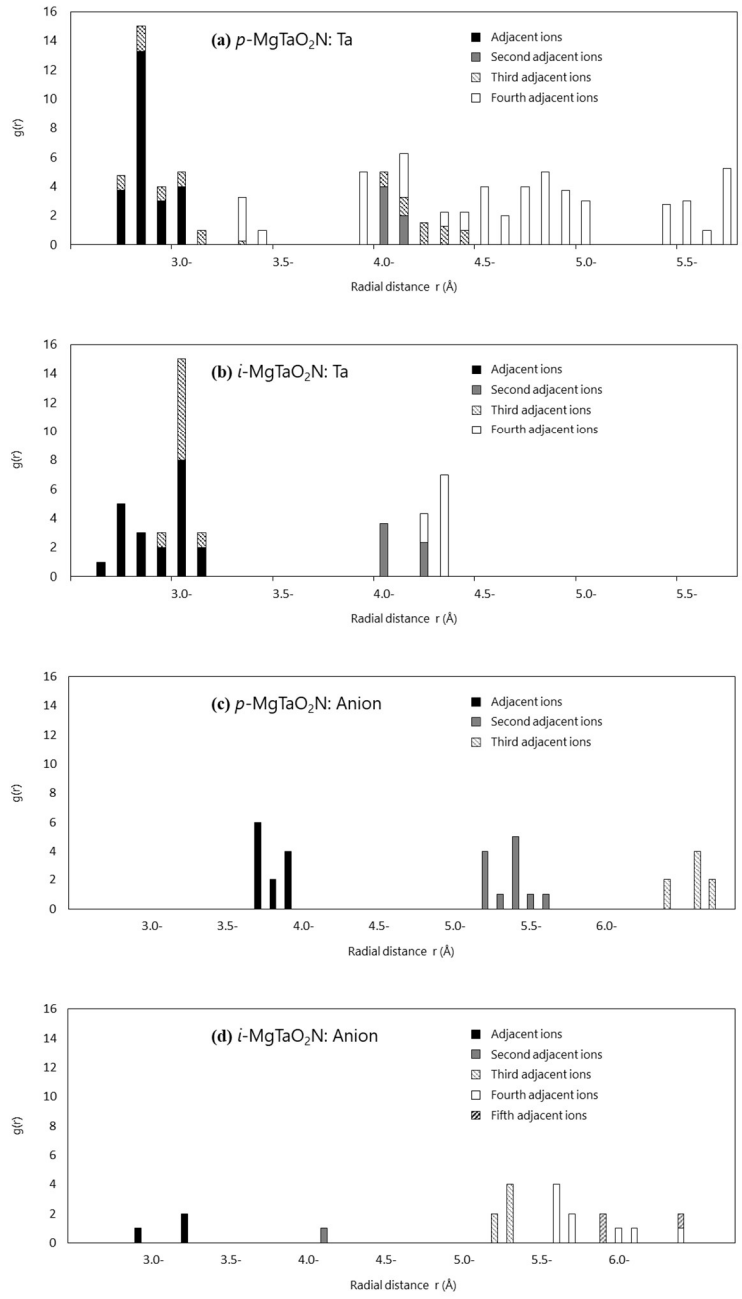

Figure 4-15. The distribution of the distance between the two homologous ions. For *p*-$MgTaO_2N$, each Ta has 12 other Ta ions and X has 75 other X anions within 5 Å distances (here, O and N are not distinguished). At variance, for *i*-$MgTaO_2N$, each Ta cation has only 4 other Ta cations, while each X has only 44 other anions within the same distance.

Considering the use as a photocatalyst, there are some disadvantages in *i*-$MgTaO_2N$ in terms of its photocatalyst related properties. The bandgap of both *i*-$MgTaO_2N$ models is larger than 4.0 eV, which is markedly larger than the energy of visible radiation. Also, since the carrier effective mass of *i*-$MgTaO_2N$ is noticeably larger, its carrier mobility will clearly result reduced. Although the CBM positions of *i*-$MgTaO_2N$ are negative enough to exceed the HER potential, their VBM positions are not positive enough to exceed the OER potential, and thus they are expected to be less performing in oxygen evolution ability. Therefore, in contrast to *p*-$MgTaO_2N$, *i*-$MgTaO_2N$ is not suitable as water splitting photocatalyst.

4-5. Conclusion

Computational screening procedures have revealed $MgTaO_2N$ a promising candidate for visible light responsive water splitting photocatalysis. However, some structural features such as octahedral-tilting, anion ordering, and polymorphism have not been considered in the previous studies, and thus the properties of $MgTaO_2N$ as a photocatalyst material have been largely overlooked.

I have here calculated the properties of $MgTaO_2N$ analyzing the mentioned features on different polymorphs and thereby discussed the applicability of $MgTaO_2N$ as a novel photocatalyst. Additionally, I have suggested a guideline to control and improve the properties of $MgTaO_2N$ in agreement with the results of the present analysis.

Accordingly, I have shown that, in contrast with the intrinsic structural instability, most of the perovskite-type $MgTaO_2N$ have band structures highly suitable for overall water splitting. In particular, *p*-$MgTaO_2N$ with reduced octahedral-tilting similarly has reduced bandgap and band edge positions that straddle the water redox potentials, although its bandgap is still slightly larger than the energy of visible light. On the other hand, $MgTaO_2N$ in ilmenite polymorph, the thermodynamically more stable one, has a bandgap extremely larger than visible light energy and band edge positions that do not match with the water redox potentials. As consequence, *i*-$MgTaO_2N$ performances in solar-to-energy devices will result quite poor.

By comparing the structural features and the calculated properties, octahedral-tilting results

to highly impact on the conduction band structures. In particular, the larger the octahedral-tilting the more marked the interaction between Ta 5d and anion 2p in the conduction band. Doping/alloying the A-site cation of $MgTaO_2N$ in the perovskite polymorph with a larger ionic radius cation, A^{2+}, forming isovalent $A'_xMg_{(1-x)}TaO_2N$ alloys is a way to reduce their octahedral-tilting, improving the performances of the final photocatalyst.

Bibliography

[1] Ceder, G.; Chiang, Y.-M.; Sadoway, D. R.; Aydinol, M. K.; Jang Y.-I.; Huang, B. Identification of cathode materials for lithium batteries guided by first-principles calculations. *Nature* **1998**, *392*, 694.

[2] Johannesson, G. H.; Bligaard, T.; Ruban, A. V.; Skriver, H. L.; Jacobsen K. W.; Nørskov, J. K. Combined Electronic Structure and Evolutionary Search Approach to Materials Design. *Phys. Rev. Lett*., **2002**, *88*, 255506.

[3] Armiento, R.; Kozinsky, B.; Fornari M.; Ceder, G. Screening for high-performance piezoelectrics using high-throughput density functional theory. *Phys. Rev. B: Condens. Matter Mater. Phys.*, **2011**, *84*, 014103.

[4] Hachmann, J.; Olivares-Amaya, R.; Atahan-Evrenk, S.; Amador- Bedolla, C.; Sanchez-Carrera, R. S.; Gold-Parker, A.; Vogt, L.; Brockway A. M.; Aspuru-Guzik, A. The Harvard Clean Energy Project: Large-Scale Computational Screening and Design of Organic Photovoltaics on the World Community Grid. *J. Phys. Chem. Lett.*, **2011**, *2*, 2241.

[5] O'Boyle, N. M.; Campbell C. M.; Hutchison, G. R. Computational Design and Selection of Optimal Organic Photovoltaic Materials. *J. Phys. Chem. C*, **2011**, *115*, 16200.

[6] Setyawan, W.; Gaume, R. M.; Lam, S.; Feigelson R. S.; Curtarolo, S. High-Throughput Combinatorial Database of Electronic Band Structures for Inorganic Scintillator Materials. *ACS Comb. Sci.*, **2011**, *13*, 382.

[7] Zhuang, H. L.; Hennig, R. G. Computational Search for Single-Layer Transition-Metal Dichalcogenide Photocatalysts. *J. Phys. Chem. C* **2013**, *117*, 20440.

[8] Wu, Y.; Lazic, P.; Hautier, G.; Persson, K.; Ceder, G. First principles high throughput screening of oxynitrides for water-splitting photocatalysts. *Energy Environ. Sci*. **2013**, *6*, 157.

[9] Castelli, I. E.; Olsen, T.; Datta, S. Landis, D. D.; Dahl, S.; Thygesen K. S.; Jacobsen, K. W. Computational screening of perovskite metal oxides for optimal solar light capture. *Energy Environ. Sci.* **2012**, *5*, 5814.

[10] Yamasita, D.; Takata, T.; Hara, M.; Kondo, J. N.; Domen, K. Recent progress of visible-light-driven heterogeneous photocatalysts for overall water splitting. *Solid State Ionics* **2004**, *172*, 591.

[11] Xu, J.; Pan, C.; Takata, T.; Domen, K. Photocatalytic overall water splitting on the perovskite-type transition metal oxynitride $CaTaO_2N$ under visible light irradiation. *Chem. Commun.* **2015**, *51*, 7191.

[12] Matoba, T.; Maeda, K.; Domen, K. Activation of $BaTaO_2N$ Photocatalyst for Enhanced Non-Sacrificial Hydrogen Evolution from Water under Visible Light by Forming a Solid Solution with $BaZrO_3$. *Chem. Eur. J.* **2011**, *17*, 14731.

[13] Maeda, K.; Domen, K. Water Oxidation Using a Particulate $BaZrO_3$-$BaTaO_2N$ Solid-Solution Photocatalyst That Operates under a Wide Range of Visible Light. *Angew. Chem. Int. Ed.* **2012**, *51*, 9865.

[14] Kasahara, A.; Nukumizu, K.; Hitoki, G.; Takata, T.; Kondo, J. N.; Hara, M.; Kobayashi, H.; Domen, K. Photoreactions on $LaTiO_2N$ under Visible Light Irradiation. *J. Phys. Chem. A* **2002**, *106*, 6750.

[15] Glazer, A. M. The Classification of Tilted Octahedra in Perovskites. *Acta Cryst.* **1972**, *B28*, 3384.

[16] Attfield, J. P. Principles and Applications of Anion Order in Solid Oxynitrides. *Cryst. Growth Des.* **2013**, *13*, 4623.

[17] Eng, H. W.; Barnes, P. W.; Auer, B. M.; Woodward, P. M. Investigations of the electronic structure of d^0 transition metal oxides belonging to the perovskite family. *J. Solid State Chem.* **2003**, *175*, 94.

[18] Balaz, S.; Porter, S. H.; Woodward, P. M. Electronic Structure of Tantalum Oxynitride Perovskite Photocatalysts. *Chem. Mater.* **2013**, *25*, 3337.

[19] Kubo, A.; Giorgi, G.; Yamashita, K. Anion Ordering in $CaTaO_2N$: Structural Impact on the Photocatalytic Activity. Insights from First-Principles. *Chem. Mater*. **2017**, *29*, 539.

[20] Goldschmidt, V. M. Die Gesetze der Krystallochemie. *Naturwissenschaften* **1926**, *14(21)*, 477.

[21] Hoffman, A. Examinations of compounds with Perovskite structure. *Z. Phys. Chem. B* **1935**, *28(1)*, 65.

[22] Li, W.; Ionescu, E.; Riedel, R. Gurlo, A. Can we predict the formability of perovskite oxynitrides from tolerance and octahedral factors? *J. Mater. Chem. A* **2013**, *1*, 12239.

[23] Kim, Y.-I.; Woodward, P. M.; Baba-Kishi, K. Z.; Tai, C. W. Characterization of the Structural,

Optical, and Dielectric Properties of Oxynitride Perovskites AMO_2N (A = Ba, Sr, Ca; M = Ta, Nb). *Chem. Mater.* **2004**, *16*, 1267.

[24] Wechsler, B. A.; Von Dreele, R. B. Structure Refinements of Mg_2TiO_4, $MgTiO_3$ and $MgTi_2O_5$ by Time-of-Flight Neutron Powder Diffraction. *Acta Cryst.* **1989**, *B45*, 542.

[25] Baura-Peña, M. P.; Martínez-Lope, M. J.; García-Clavel, M. E. Synthesis of the mineral geikielite $MgTiO_3$. *J. Mater. Sci.* **1991**, *26*, 4341.

[26] Shannon, R. D.; Prewitt, C. T. Effective Ionic Radii in Oxides and Fluorides. *Acta Cryst.* **1969**, *B25*, 925.

[27] Günther, E.; Hagenmayer, R.; Jansen, M. Structural Investigations on the Oxidenitrides $SrTaO_2N$, $CaTaO_2N$ and $LaTaON_2$ by Neutron and X-ray Powder Diffraction. *Z. Anorg. Allg. Chem.* **2000**, *626*, 1519.

[28] Kresse, G.; Hafner, J. Ab initio molecular dynamics for liquid metals. *Phys. Rev. B: Condens. Matter Mater. Phys.* **1993**, *47*, 558.

[29] Kresse, G.; Hafner, J. Ab initio molecular-dynamics simulation of the liquid metal−amorphous-semiconductor transition in germanium. *Phys. Rev. B: Condens. Matter Mater. Phys.* **1994**, *49*, 14251.

[30] Kresse, G.; Furthmüller, J. Efficiency of ab-initio total energy calculations for metals and semiconductors using a plane-wave basis set. *Comput. Mater. Sci.* **1996**, *6*, 15.

[31] Kresse, G.; Furthmüller, J. Efficient iterative schemes for ab initio total-energy calculations using

a plane-wave basis set. *Phys. Rev. B: Condens. Matter Mater. Phys.* **1996**, *54*, 11169.

[32] Perdew, J. P.; Burke, K.; Ernzerhof, M. Generalized Gradient Approximation Made Simple. *Phys. Rev. Lett.* **1996**, *77*, 3865.

[33] Blöchl, P. E. Projector augmented-wave method. *Phys. Rev. B: Condens. Matter Mater. Phys.* **1994**, *50*, 17953.

[34] Kresse, G.; Joubert, D. From ultrasoft pseudopotentials to the projector augmented-wave method. *Phys. Rev. B: Condens. Matter Mater. Phys.* **1999**, *59*, 1758.

[35] Krukau, A. V.; Vydrov, O. A.; Izmaylov, A. F.; Scuseria, G. E. Influence of the exchange screening parameter on the performance of screened hybrid functionals. *J. Chem. Phys.* **2006**, *125*, 224106.

[36] Toroker, M. C.; Kanan, D. K.; Alidoust, N.; Isseroff, L. Y.; Liao, P.; Carter, E. A. First principles scheme to evaluate band edge positions in potential transition metal oxide photocatalysts and photoelectrodes. *Phys. Chem. Chem. Phys.* **2011**, *13*, 16644.

[37] Huang, W. L. First-principles determination of the absolute band-edge positions of BiOX (X = F, Cl, Br, I). *Comput. Mater. Sci.* **2012**, *55*, 166.

[38] Tasker, P. W. The stability of ionic crystal surfaces. *J. Phys. C: Solid State Phys*. **1979**, *12*, 4977.

[39] Clark, L.; Oró-Solé, J.; Knight, K. S.; Fuertes, A.; Attfield, J. P. Thermally Robust Anion-Chain Order in Oxynitride Perovskites. *Chem. Mater.* **2013**, *25*, 5004.

[40] Yang, M.; Oró-Solé, J.; Rodgers, J. A.; Jorge, A. B.; Fuertes, A.; Attfield, J. P. Anion order in

perovskite oxynitrides. *Nat. Chem.* **2011**, *3*, 47.

[41] Porter, S. H.; Huang, Z.; Woodward, P. M. Study of Anion Order/Disorder in $RTaN_2O$ (R = La, Ce, Pr) Perovskite Nitride Oxides. *Cryst. Growth Des.* **2014**, *14*, 117.

[42] Fuertes, A. Metal oxynitrides as emerging materials with photocatalytic and electronic properties. *Mater. Horiz.* **2015**, *2*, 453.

Chapter 5.

Composition Dependence of Oxynitride Solid Solution: A Demonstration on $LaMg_xTa_{1-x}O_{1+3x}N_{2-3x}$

5-1. Introduction to $LaMg_xTa_{1-x}O_{1+3x}N_{2-3x}$ photocatalyst

5-1-1. Development of solid solution-based photocatalysts

Following the emerging photocatalysts consisting of oxynitrides, solid-solutions of such compounds are also attracting wide attention due to their improved photocatalytic activities. One of the noticeable examples of them is $LaMg_xTa_{1-x}O_{1+3x}N_{2-3x}$, which was developed by Domen's group in 2015 [1]. This compound had absorbed light with wider range of wavelengths (~ 600 nm) and had achieved overall water splitting without any sacrificial agent.

$LaMg_xTa_{1-x}O_{1+3x}N_{2-3x}$ is a solid solution between $LaMg_{2/3}Ta_{1/3}O$ and $LaTaO_2N$, all of which have perovskite structure. It had been prepared by synthesizing oxide precursors by citric acid method and subsequently nitriding them in a dry NH_3 flow under a high temperature [1-4]. It was also reported that the water splitting activity of $LaMg_xTa_{1-x}O_{1+3x}N_{2-3x}$ differs depending on its composition, and reaches the maximum at x = 1/3.

5-1-2. Important factors in modifying the solid solutions

There are two key factors which led to a successful achievement of overall water splitting by $LaMg_xTa_{1-x}O_{1+3x}N_{2-3x}$. One is the fine-tuning of its band structure by changing its composition. In particular, the O/N ratio, both of which contribute their orbitals to the valence bands, and Ta content, which gives their orbitals to construct the conduction bands, will be varied depending on the composition. Thus, it is strongly expected that the band structures of $LaMg_xTa_{1-x}O_{1+3x}N_{2-3x}$ will be changed due to the compositional variation.

The other key factor is that unwanted side reactions such as the backward reaction of O_2 and the self-oxidation of N^{3-} was successfully suppressed by coating the photocatalyst surface with amorphous oxyhydroxide TiOXH (= $TiO_{2-m}(OH)_{2m}\cdot xH_2O$). It is thought that the layers of amorphous TiOXH had played a role like a molecular sieve since they have a porous structure. Such coating method can also be applied not only to $LaMg_xTa_{1-x}O_{1+3x}N_{2-3x}$ but also to other photocatalyst materials, and have already succeeded in improving the water splitting activities of some other photocatalysts such as $CaTaO_2N$ [5] and $LaSc_xTa_{1-x}O_{1+2x}N_{2-2x}$ [2].

Nevertheless, there still remains a critical issue to be tackled in the former factor in order to consider the compositional tuning of the band structure of $LaMg_xTa_{1-x}O_{1+3x}N_{2-3x}$. The issue is that the dependence of the band structure of the solid solution on its composition has not been systematically investigated yet, and thus the factor that maximized its activity at the composition of x = 1/3 is not

fully understood yet. In other words, the guidelines to tune the photocatalyst related properties of solid solutions to their optimized ones for water splitting has not been established. Hence, in order to accelerate the material design in the field of solid solution photocatalysts, one need to relate their band structures to their compositions, and identify the positive and negative factors that exist at each composition.

5-1-3. Research objectives

Here, in this study, I will systematically calculate and compare the band structures of $LaMg_xTa_{1-x}O_{1+3x}N_{2-3x}$ by means of first principle calculations, using appropriate structural models of the solid solutions. Furthermore, I will estimate the photocatalyst related properties such as bandgaps, carrier effective masses, and band edge positions to understand the positive and negative factors at each composition and clearly articulate the reason why the water splitting activity of $LaMg_xTa_{1-x}O_{1+3x}N_{2-3x}$ reaches the highest at the composition of $x = 1/3$.

5-2. Computational details

First, I prepared the structural model of $LaMg_xTa_{1-x}O_{1+3x}N_{2-3x}$ at each composition, and then calculated its band structure from first principle. Subsequently, I estimated the photocatalyst related properties at each composition by analyzing the obtained band structure.

5-2-1. Structural models

The structural models of $LaMg_xTa_{1-x}O_{1+3x}N_{2-3x}$ were prepared based on the crystal coordinate data previously reported by neutron diffraction. The unit cells of $LaMg_xTa_{1-x}O_{1+3x}N_{2-3x}$ consists of 20 atoms with space group $I2/m$ at x = 0 ($LaTaO_2N$ [6]) and with $P2_1/n$ at the other compositions [7], both of which are monoclinic. In $LaMg_xTa_{1-x}O_{1+3x}N_{2-3x}$, Ta and Mg occupy the equivalent cation sites, and O and N occupy the equivalent anion sites. As mentioned later, the Ta/Mg ratio at each cation site has been already reported [7], and it has also been previously revealed that cations and anions in perovskite oxynitrides are generally arranged according to certain rules [6,8-10].

Thus, I prepared the structural models in accordance with such orderings of ions, using a 2 × 1 × 3 supercell for $LaTaO_2N$ and 2 × 3 × 1 supercells for $LaMg_xTa_{1-x}O_{1+3x}N_{2-3x}$ ($x \neq 0$) (120 atoms). Here, I considered the compositions at x = 0, 1/6, 1/3, 1/2, and 2/3 (The number of constituent atoms at each composition are listed in Table 5-1). It should be noted that, at each composition, the ionic arrangement was determined individually, since $LaMg_xTa_{1-x}O_{1+3x}N_{2-3x}$ is experimentally synthesized from the oxide precursor that differs depending on the composition [1,2].

Table 5-1. The number of the constituent atoms in the supercell at each composition

x	0	1/6	1/3	1/2	2/3
La	24	24	24	24	24
Mg	0	4	8	12	16
Ta	24	20	16	12	8
O	24	36	48	60	72
N	48	36	24	12	0

The possible cation arrangements in the structural models were considered by following the reported Ta/Mg ratio at each site in the unit cell in the previous neutron diffraction measurements (See Table 5-2 [7] and Figure 5-1). Then, the most stable arrangements were determined with help from the insights on cation orderings in perovskite crystals previously reported, where the two-different cations (B', B'') at B sites (equivalent sites) are revealed to be delocalized to form a "rock-salt" type arrangement when their sizes or charges are significantly different [8, 9]. Such an arrangement occurs in order to minimize the Coulomb interaction between the cations with the greater charge, and to make the six anion sites adjacent to B equivalent to each other. Our preliminary calculation results also followed such rule, *i.e.* the more delocalization of Ta^{5+} cations, the smaller total energy of the structural model.

Table 5-2. The reported Ta/Mg ratio at each site in the unit cell [7]

site	coordinate			composition		
	x	y	z	1/3	1/2	2/3
M1	0.5	0.0	0.0	2:1	2:1	2:1
M2	0.0	0.5	0.0	2:1	1:2	0:3

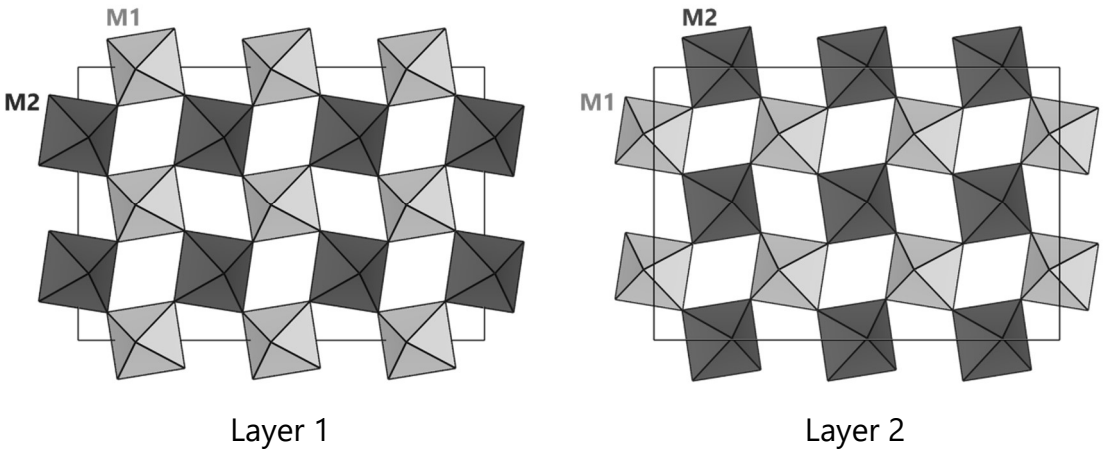

Figure 5-1. M1 and M2 sites in the 2 × 3 × 1 supercell for $LaMg_xTa_{1-x}O_{1+3x}N_{2-3x}$. For simplicity, La atoms are omitted. Hereafter, the two layers vertical to c-axis will be called “layer 1” and “layer 2”, respectively, as this illustrations in order to depict the structural models clearly in the following sections.

On the other hand, the possible anion arrangements in the structural models were considered in accordance with some previous studies on anion orderings [6, 10], since the O/N ratios had not been experimentally measured. In a number of previous studies on perovskite oxynitrides, N^{3-} was revealed to coordinate to the B site cation (central cation) in *cis*-configuration or *fac*-configuration. In addition,

according to the study in chapter 3, it was demonstrated that N^{3-} in perovskite oxynitrides prefers to be arranged in lower symmetric configurations. Our preliminary calculations on the structural models with different anion arrangements also confirmed that *trans*-configurations hardly occur at room temperature (78 meV/atom), and that the structures with delocalized N^{3-} are more stable than those with rather localized N^{3-}. Therefore, I only prepared the structural models of $LaMg_xTa_{1-x}O_{1+3x}N_{2-3x}$ with the restriction that N^{3-} can only take *cis*- or *fac*-configuration (It should be noted that at x = 1/6 a few pairs of N in *trans*-configuration were inevitably given since the N/Ta ratio is larger than three.).

Then, finally, the relative positions between cations and anions were determined according to the previously reported insights, where N combines with Ta more strongly than with Mg, and O combines with Mg more strongly than with Ta [11]. A similar trend was also obtained from our preliminary calculations on the testing structural models, indicating that N-Mg bond will hardly be formed at room temperature. Thus, I prepared the structural models of $LaMg_xTa_{1-x}O_{1+3x}N_{2-3x}$ without any N-Mg bonds in their supercells.

Here, the process of determining the structural model at each composition will be provided. First, the structural model at x = 0 ($LaTaO_2N$) was prepared in accordance with the crystal coordinates and the O/N ratio previously reported where the O/N ratio at Y1 sites (0.7394, 0.0, 0.6775), Y21 sites (0.0, 0.7818, 0.0), and Y22 sites (1/2, 0.2148, 0.0) were revealed to be 1:1, 1:1, and 0:1, respectively [6]. Though the number of possible anion arrangements that satisfy such O/N ratio is $2^2 \times 2^2 = 16$

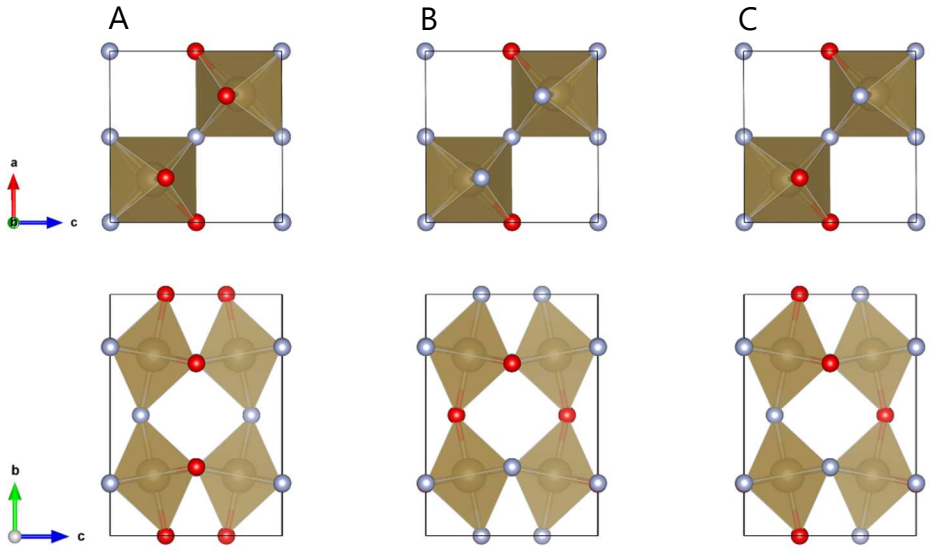

Figure 5-2. Possible anion orderings in $LaTaO_2N$ viewed from different angles with their relative total energies (ΔE) and bandgaps (E_g) calculated within PBE level. Brown, red, and blue are Ta, O, and N atoms, respectively. La atoms are omitted.

(where each 2^2 corresponds to the number of possible outcomes at Y1 and Y21 sites), some of them were essentially the same anion orderings due to their symmetries. Thus, they can be reduced to three different anion orderings (A-C) as shown in Figure 5-2. Here, C was revealed to be the most stable one, and A was revealed to have the smallest bandgap.

Second, the structural model at x = 2/3 ($LaMg_{2/3}Ta_{1/3}O_3$) was determined following the Ta/Mg ratio listed in Table 5-2. At this composition, two-thirds of M1 sites are dominated by Ta, while all the M2 sites are dominated only by Mg. Hence, in the structural models prepared using 2 × 3 × 1

supercells, eight of the twelve M1 sites were placed by Ta and the other B-cation sites were placed by Mg. Here, one can consider three different Ta arrangements in each layer and two different types of their sequence ("in" and "out") as depicted in Figure 5-3. Among these six possible cation orderings, A_{Out} was revealed to be the most stable one, and A_{In} in to have the smallest bandgap.

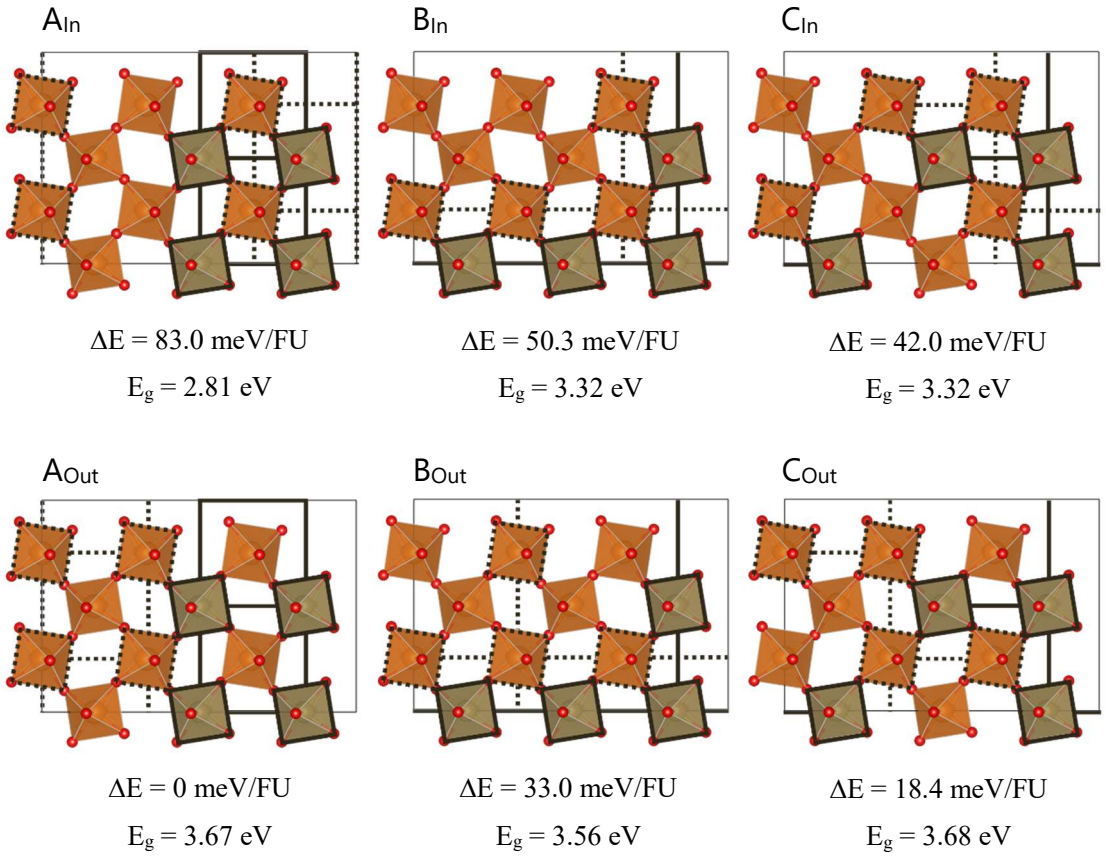

Figure 5-3. Possible cation orderings in $LaMg_{2/3}Ta_{1/3}O_3$ with their relative total energies (ΔE) and bandgaps (E_g) calculated within PBE level. Brown, orange, and red are Ta, Mg, and O atoms, respectively. La atoms are omitted. Solid and dotted lines correspond to the Ta sites on layer 1 and layer 2, respectively.

Subsequently, the structural model at x = 1/2 ($LaMg_{1/2}Ta_{1/2}O_{5/2}N_{1/2}$.) was also discussed in line with the Ta/Mg ratio in Table 5-2. According to the constraint that N can only combine with Ta, Ta was considered to form a kind of linkage mediated by N. Additionally, since two-thirds of Ta occupy M1 sites, such linkage was assumed to be a branched one as depicted in Figure 5-4. Then, all the remaining anion sites around Ta in Figure 5-4 was placed by O in order to satisfy the number of each constituent atom listed in Table 5-1. Here, the possible structural models were prepared by arranging four [-N-TaO_3(TaO_5N)-N-TaO_4-] units defined in Figure 5-4 in the supercell. These units can be arranged either on the two planes by half (as models A1-A6 in Figure 5-5) or on only single plane (as B1-B2 in Figure 5-5), and six and two different anion orderings can be introduced for each case, respectively. Then, among these eight candidates, it was revealed that A6 is the most stable one and B2 has the smallest bandgap.

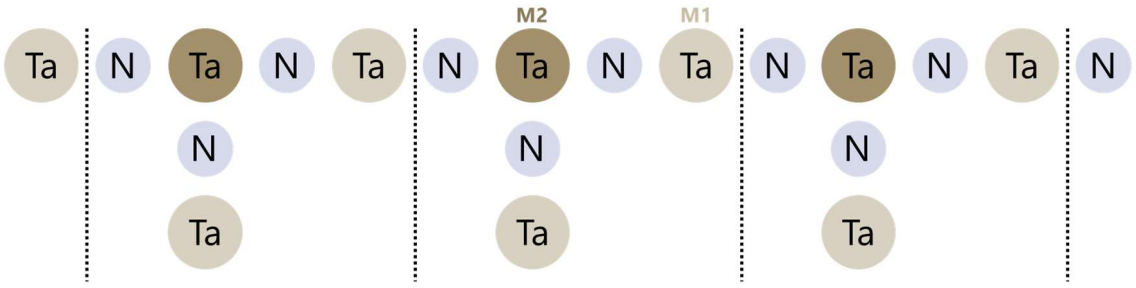

Figure 5-4. The assumed linkage unit [-N-TaO_3(TaO_5N)-N-TaO_4-] in the structural models of $LaMg_{1/2}Ta_{1/2}O_{5/2}N_{1/2}$. For the simplicity, O atoms are omitted.

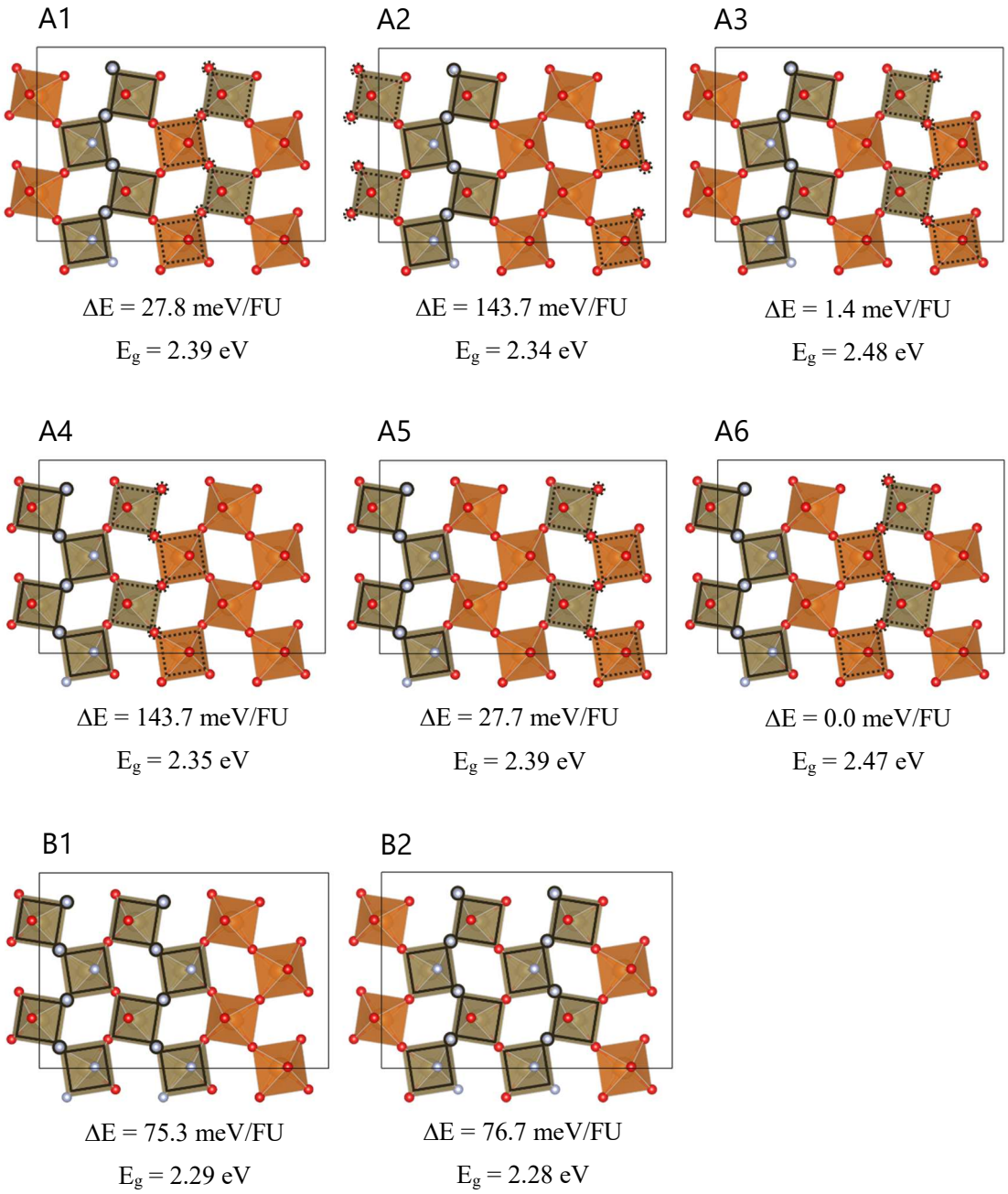

Figure 5-5. Possible arrangement of [-N-TaO_3(TaO_5N)-N-TaO_4-] units in $LaMg_{1/2}Ta_{1/2}O_{5/2}N_{1/2}$ with their relative total energies (ΔE) and bandgaps (E_g) calculated within PBE level. Brown, orange, red, and blue are Ta, Mg, O, and N atoms, respectively. La atoms are omitted. Solid and dotted lines correspond to the [-N-TaO_3(TaO_5N)-N-TaO_4-] units on layer 2 and layer 1, respectively.

Next, the structural model at x = 1/3 ($LaMg_{1/3}Ta_{2/3}O_2N$) was determined as well according to the Ta/Mg ratio shown in Table 5-2 and the constraints on the arrangements of N previously mentioned. First, since the N/Ta ratio is 3:1 at this composition, it was considered that all Ta were coordinated by three N in *fac*-configuration to form the linkage unit depicted in Figure 5-6. Then, such units were assumed to be arranged in "zig-zag" or "cylinder" orderings as depicted in Figure 5-7 and Figure 5-8, respectively, since the number of Ta placed at M1 and M2 sites are the same at this composition. Here, eight different arrangements of N were introduced for each case, and subsequently it was revealed that Z5 is the most stable one and C3 has the smallest bandgap.

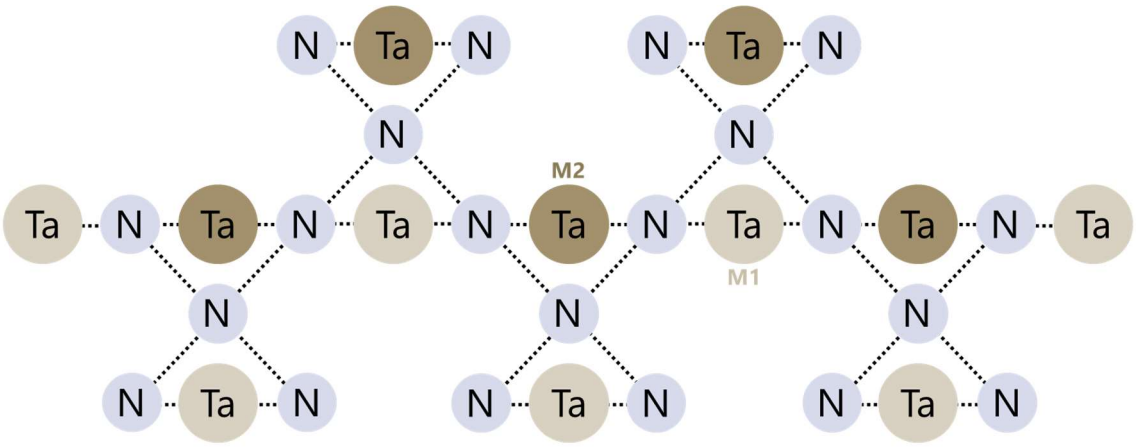

Figure 5-6. The assumed linkage in the structural models of $LaMg_{1/3}Ta_{2/3}O_2N$. For the simplicity, O atoms are omitted.

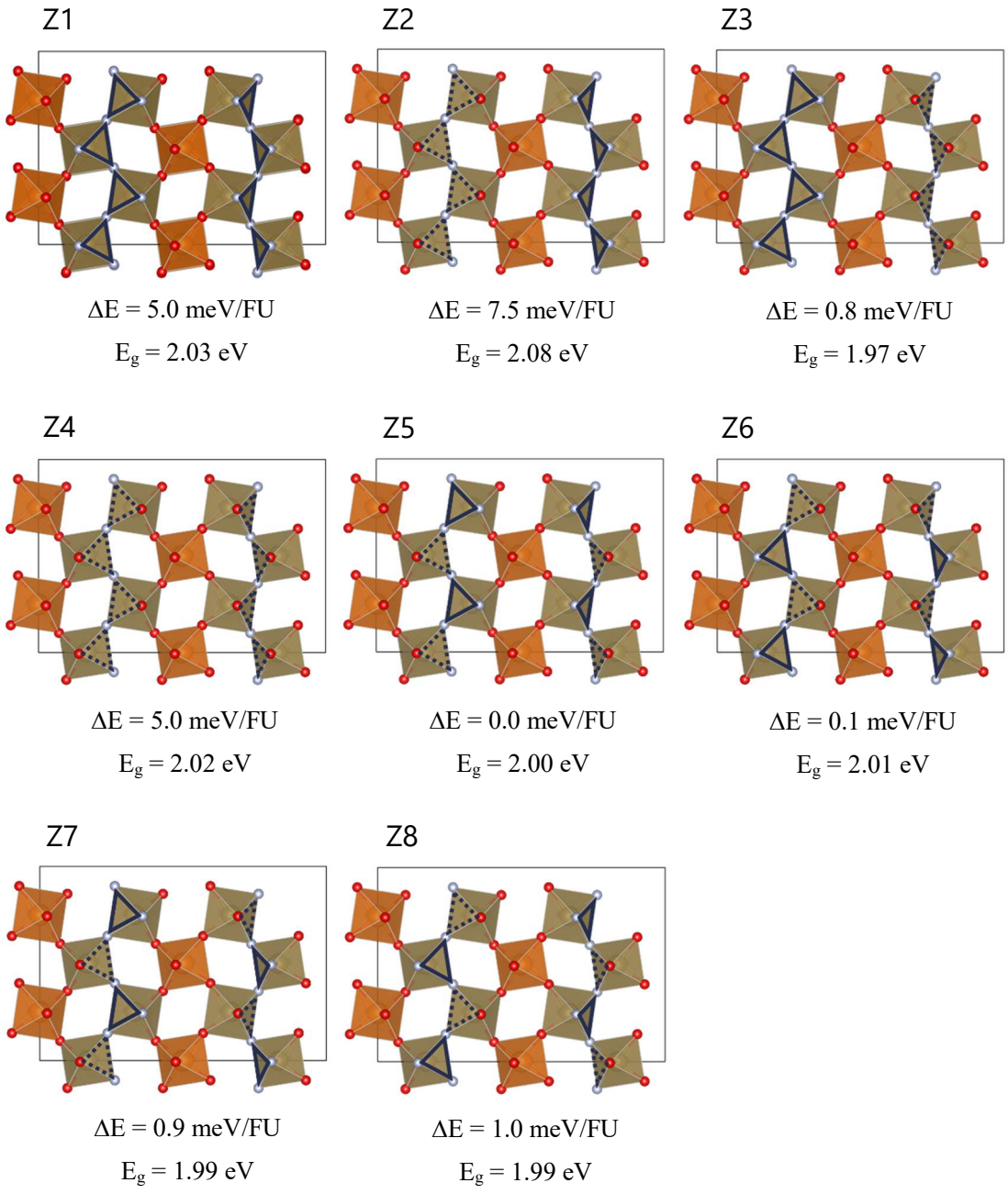

Figure 5-7. Possible "zig-zag" arrangement of the linkage units in $LaMg_{1/3}Ta_{2/3}O_2N$ with their relative total energies (ΔE) and bandgaps (E_g) calculated within PBE level. Brown, orange, red, and blue are Ta, Mg, O, and N atoms, respectively. La atoms are omitted. Solid and dotted triangles correspond to the N atoms surrounding Ta on layer 1 from the front and the back side, respectively.

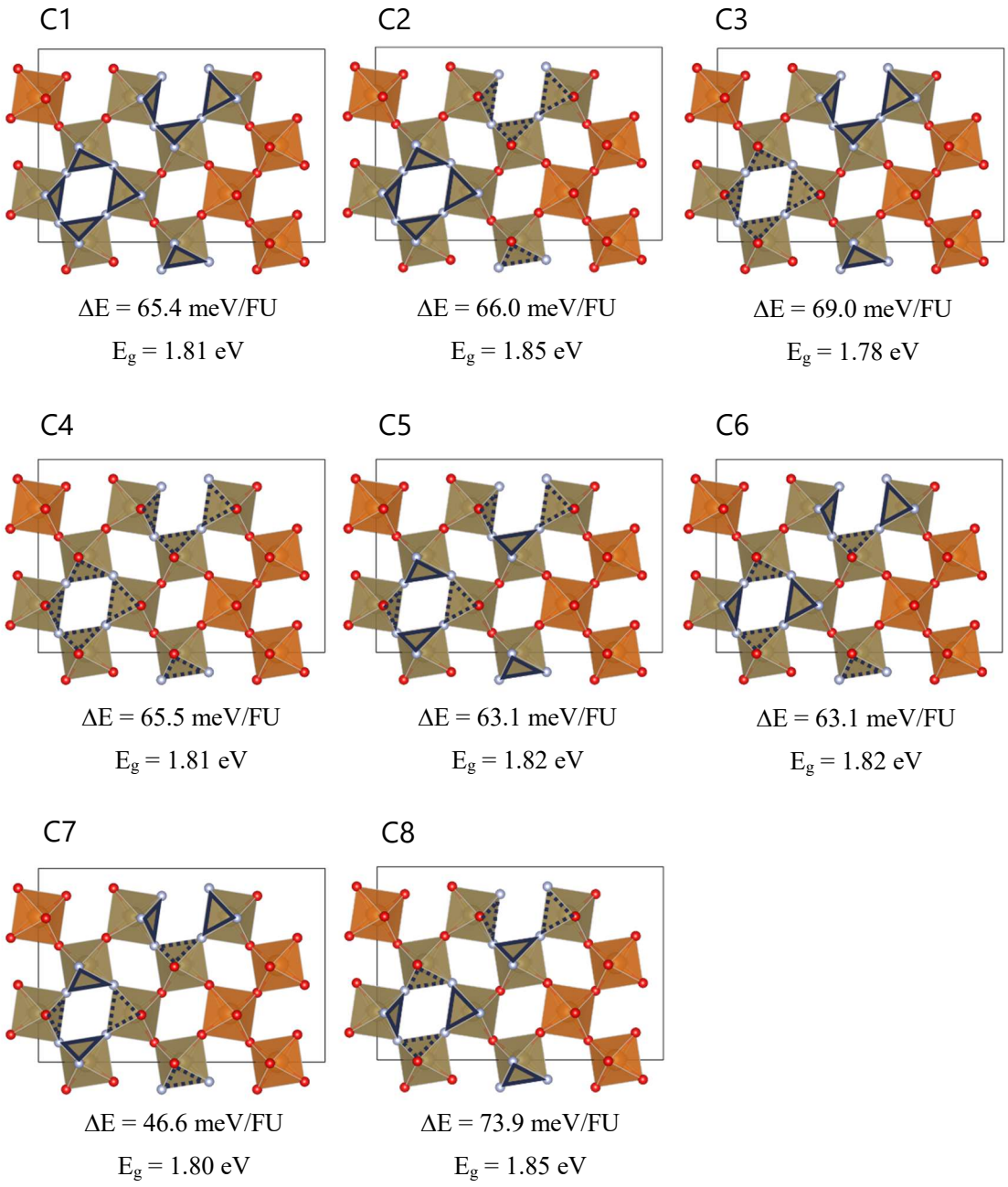

Figure 5-8. Possible "cylinder" arrangement of the linkage units in $LaMg_{1/3}Ta_{2/3}O_2N$ with their relative total energies (ΔE) and bandgaps (E_g) calculated within PBE level. Brown, orange, red, and blue are Ta, Mg, O, and N atoms, respectively. La atoms are omitted. Solid and dotted triangles correspond to the N atoms surrounding Ta on layer 1 from the front and the back side, respectively.

Finally, the structural model at x = 1/6 ($LaMg_{1/6}Ta_{5/6}O_{3/2}N_{3/2}$) was determined as follows. Initially, the cation ordering was investigated using the same size of supercell (2 × 3 × 1) of a hypothetical compound, $LaMg_{1/6}Ta_{5/6}ON_2$, where four Mg are surrounded by six O, and the other anion sites are occupied only by N. Here, the Ta/Mg ratio at M1 and M2 sites were assumed to be 5:1 (= random arrangements) by analogy with those at x = 1/3 (see Table 5-2), and Mg was assumed be non-adjacent to each other in order to reflect its dilute concentration. Thus, eight different cation orderings were prepared as shown in Figure 5-9, and among them A was revealed to be the most stable one. Subsequently, six anion arrangements were considered as shown in Figure 5-10, and A2 was revealed to be the most stable one and A5 to have the smallest bandgap.

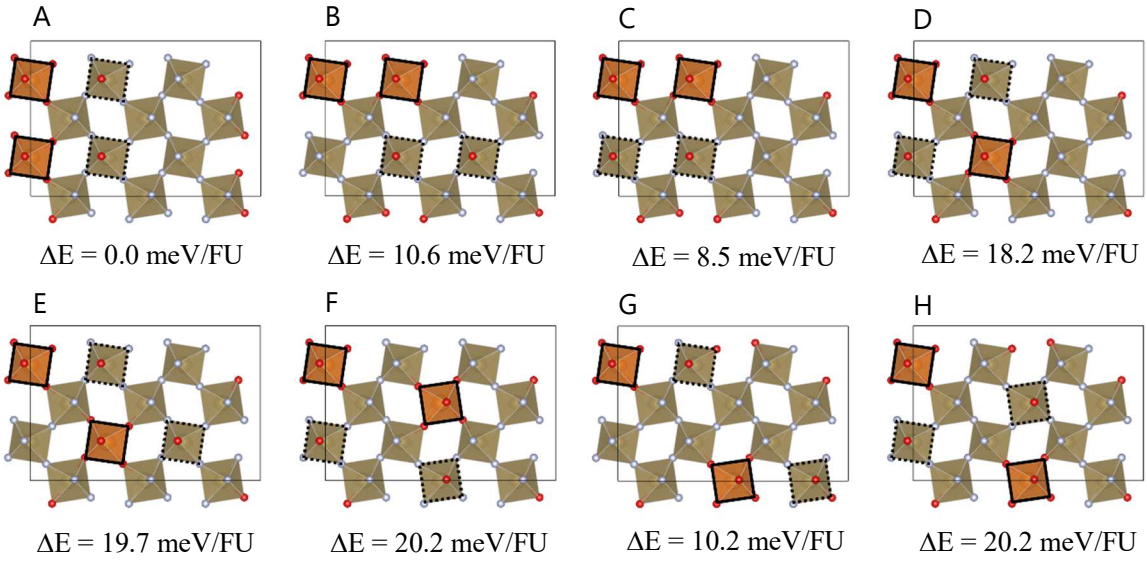

Figure 5-9. Possible cation orderings in $LaMg_{1/6}Ta_{5/6}ON_2$ with their relative total energies (ΔE) calculated within PBE level. Brown, orange, and red are Ta, Mg, and O atoms, respectively. La atoms are omitted. Solid and dotted lines correspond to the Mg sites on layer 2 and layer 1, respectively.

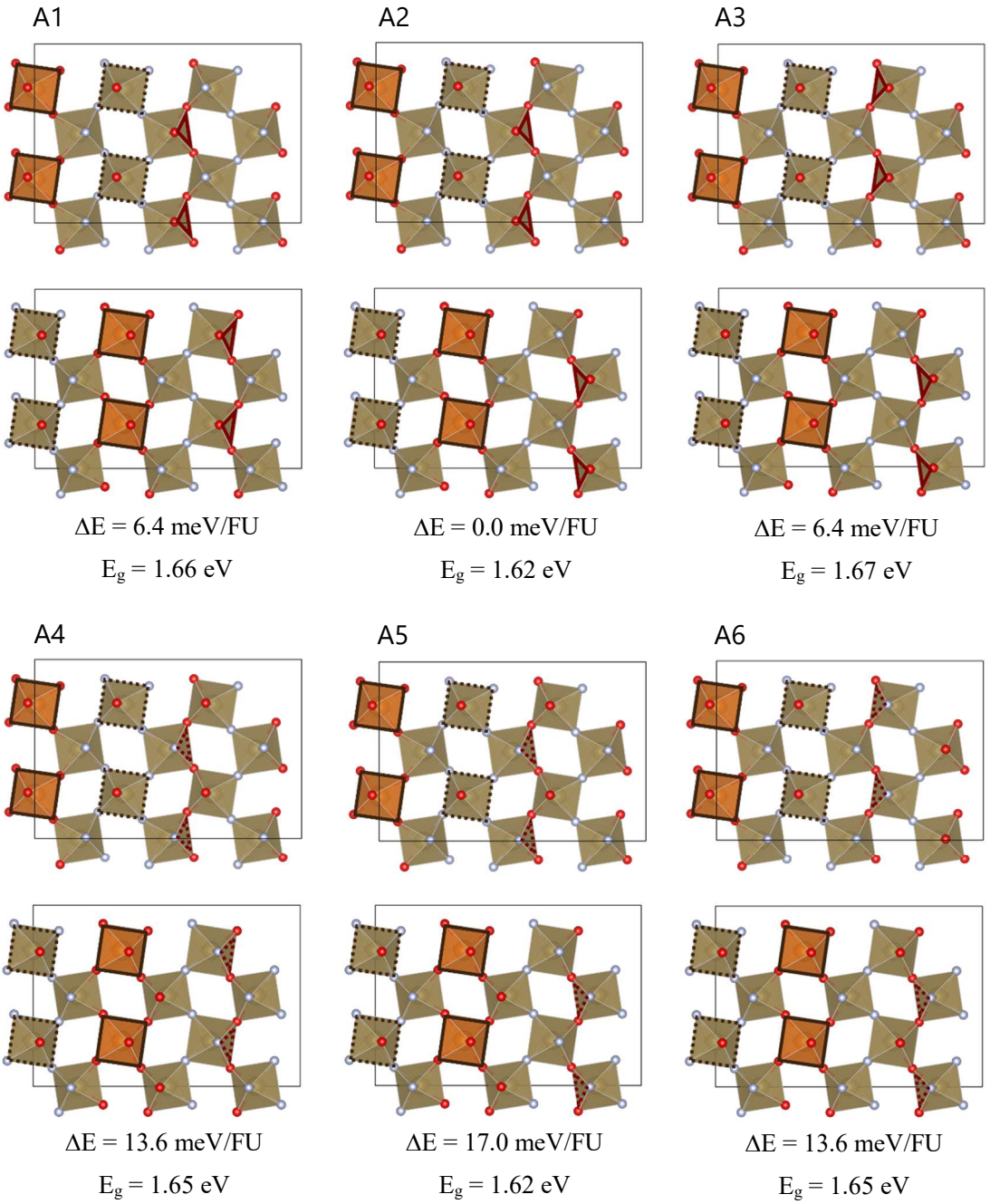

Figure 5-10. Possible ionic arrangements in $LaMg_{1/6}Ta_{5/6}O_{3/2}N_{3/2}$ on layer 2 (top) and 1 (bottom) with their relative total energies (ΔE) and bandgaps (E_g) calculated within PBE level. Brown, orange, red, and blue are Ta, Mg, O, and N atoms, respectively. La atoms are omitted. Solid and dotted triangles correspond to the O atoms surrounding Ta on each layer from the front and the back side, respectively.

Here, the structural model of $LaMg_xTa_{1-x}O_{1+3x}N_{2-3x}$ at each composition with the most stable ionic arrangement were shown in Figure 5-11. The fundamental properties of $LaMg_xTa_{1-x}O_{1+3x}N_{2-3x}$ such as band structures, density of states, carrier effective masses, were obtained by the calculation results of these most stable structural models. On the other hand, bandgaps and band edge positions were estimated not only from the most stable ones but also from the metastable structural model that has the smallest bandgap at each composition within an energy difference of 78 meV/atom (= vibrational energy per atom at room temperature), based on the consideration that the experimental absorption edge comes from the light absorption by the crystal domains with the smallest bandgap.

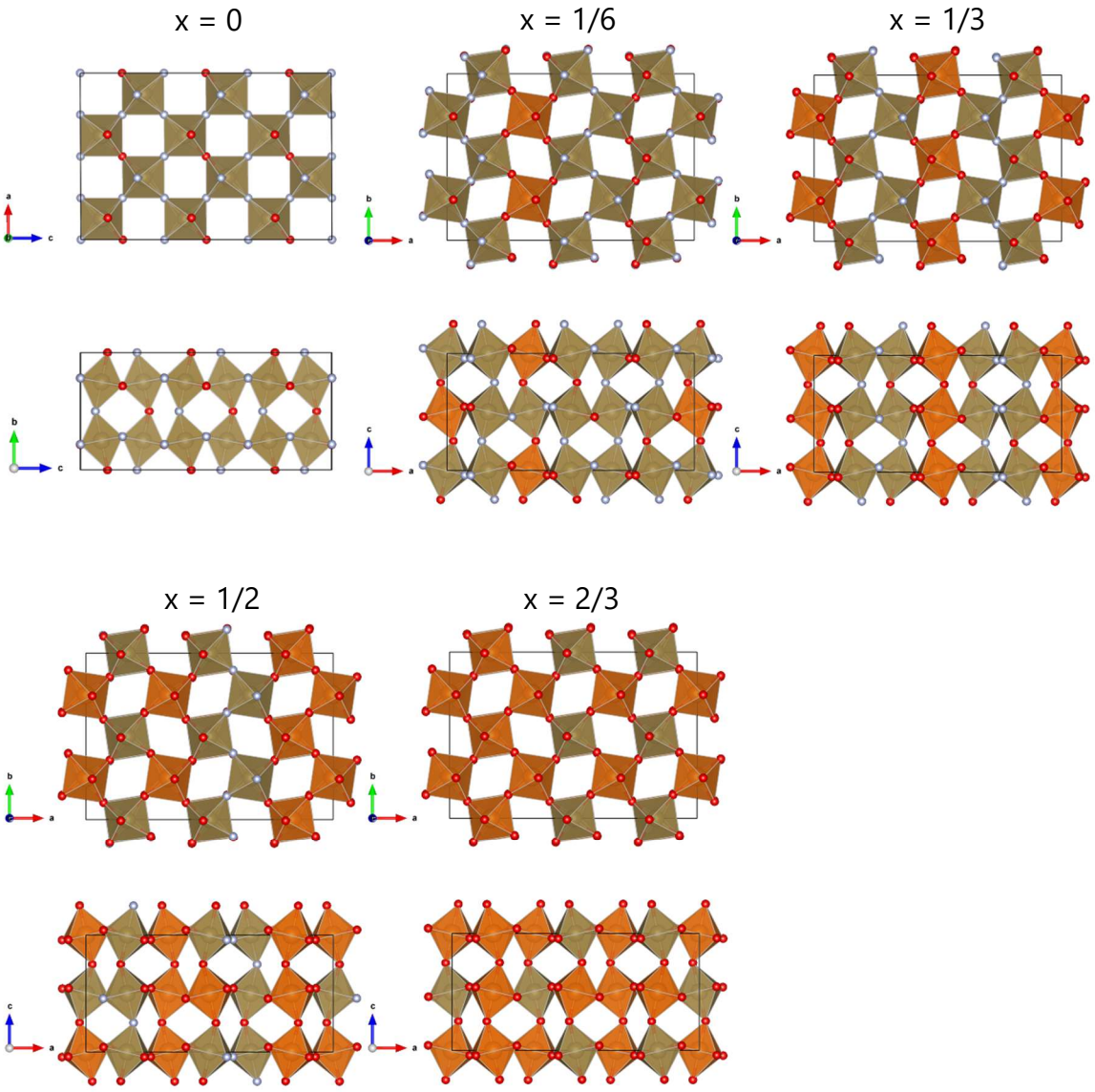

Figure 5-11. The structural models of $LaMg_xTa_{1-x}O_{1+3x}N_{2-3x}$ in its most stable ionic arrangement viewed from different angles. Brown, orange, red, and blue are Ta, Mg, O, and N atoms, respectively. La atoms are omitted.

5-2-2. Calculation procedures

The optimized geometries and the electronic structures of $LaMg_xTa_{1-x}O_{1+3x}N_{2-3x}$ were calculated by means of the density functional theory (DFT) as implemented in VASP code [12-15]. The exchange-correlation energies were described within the theory of general gradient approximation, and thus PBE (Perdew–Burke-Ernzerhof) functional [16] was adopted for the calculations. The projector augmented wave (PAW) method was also applied [17, 18], and thus eleven electrons (5s, 5p, 5d, and 6s) in La, eight electrons (2p and 3s) in Mg, eleven electrons (5p, 6s, and 5d) in Ta, six electrons (2s and 2p) in O, and five electrons (2s and 2p) in N were treated as valence states. In the geometrical optimizations, *k*-point sampling was set to 1 × 2 × 2 and the structures were relaxed until the forces on all atoms were smaller than 0.01 eV/Å and their total energies were converged within 10^{-4} eV. On the other hand, in the single point calculations, *k*-point sampling was set to 2 × 3 × 4 (3 × 4 × 2 at x = 0) and the electronic structures were calculated until their total energies were converged within 10^{-5} eV. In all cases, a 500 eV cutoff energy was used.

The band structures and the carrier effective masses were evaluated from Kohn-Sham eigenstates obtained in the single point calculations mentioned above, and the thermodynamic stabilities of the crystals were estimated based on their Kohn-Sham eigenvalues. In addition, to obtain the bandgaps and the band edge positions, HSE06 hybrid functional [19-21] was also applied to the single point calculations in order that the underestimation of the pure DFT calculated bandgaps will

be compensated.

The band structures of $LaMg_xTa_{1-x}O_{1+3x}N_{2-3x}$ were calculated along eight high symmetry points (Γ(0.0, 0.0, 0.0), A_0(0.5, 0.0, 0.5), B(0.0, 0.0, 0.5), C(0.5, 0.5, 0.0) D(0.0, 0.5, 0.5), E_0(0.5, 0.5, 0.5), Y(0.5, 0.0, 0.0), Z(0.0, 0.5, 0.0)) in the Brillouin zones. The same symmetry points were also used in the calculation of the band structure of $LaTaON_2$ (x = 0) though it has a different space group (*I*2/*m* for x = 0, and *P*2$_1$/*n* for x > 0), since *I*2/*m* also belongs to monoclinic crystal system as same as *P*2$_1$/*n* and thus has a similar Brillouin zone. It should be noted that there generally occurs a Brillouin zone folding in a supercell, and in this case the eight symmetry points were folded and to any one of the four symmetry points, Γ, A_0, B, or Y. However, the eight high symmetry points mentioned above were also directly applied to the band structures of the supercells here, since the VBM and CBM appeared at any one of the four symmetry points after the Brillouin zone folding at all compositions.

The charrier effective masses were obtained from the curvatures of valence and conduction bands around their maximum and minimum, respectively, as was the case in chapter 3 and 4 (see Eq (3.1) in chapter 3). Also in this study, the band curvatures were calculated from the high symmetry point where CBM and VBM appears toward the other seven high symmetry points. In this manner, the carrier effective mass for each direction was obtained individually. Here, the curvatures of the bands were calculated within a *k*-point range of ± 0.05 Å^{-1} from CBM and VBM, and the averaged effective mass was obtained as a harmonic mean value (see Eq (3.2) in chapter 3).

The band edge positions (E_{VBM}, E_{CBM}) of $LaMg_xTa_{1-x}O_{1+3x}N_{2-3x}$ relative to the redox potentials of water were estimated as following procedures. First, the band edge offsets (ΔE_{VBM} and ΔE_{CBM}) between different compositions were calculated only from first principles. Subsequently, the band edge positions of $LaTaO_2N$ (x = 0) were set to the experimentally reported values, E_{CBM} = -0.62 V_{NHE} and E_{VBM} = +1.31 V_{NHE}, which had been obtained from photoelectron spectroscopies in air (PESA) [2], and consequently all the band edge positions at the other compositions were estimated.

In order to calculate the band edge offsets (ΔE_{VBM} and ΔE_{CBM}) between different compounds or structures, there exist three different methods to be performed: (A) Referencing the band energies to the vacuum potentials [22, 23], (B) Referencing the band energies to the bulk potentials [23- 25], and (C) Referencing the band energies to the core levels [26, 27]. Each approach has advantages and disadvantages as follows.

In method (A), one can evaluate the band edge positions of a compound using the vacuum potential which is obtained from the calculation on a slab model that has both a crystal region and a vacuum region in its unit cell, as demonstrated in chapter 3 and chapter 4. Such approach is superior in terms of its ability to evaluate the band edge positions of various types of compounds and structures independently. However, as mentioned in the previous chapters, the vacuum potential obtained from the calculations on a slab model generally has a strong dependence on the slab surface structure [23, 28]. Therefore, when one evaluates the band edge offsets between different two compounds the result

will also inevitably reflects the difference between their surface structures.

In method (B), the band edge offsets between two different compounds (A, B) are estimated using the bulk potential ($V^{\mathrm{i}}_{\mathrm{bulk}}$, i = A, B) obtained from each unit cell and a bulk potential offset (ΔV_{bulk}) obtained from a superlattice, *i.e.* a structural model that consists of several units of A and B contacting to each other at their interface. Indeed, the band edge offsets are obtained as the following equations,

$$\Delta E_{\mathrm{VBM}} = \Delta E^{\mathrm{A}}_{\mathrm{VBM}} - \Delta E^{\mathrm{B}}_{\mathrm{VBM}} + \Delta V_{\mathrm{bulk}} \quad (5.1)$$

$$\Delta E_{\mathrm{CBM}} = E^{\mathrm{A}}_{\mathrm{g}} - E^{\mathrm{B}}_{\mathrm{g}} - \Delta E_{\mathrm{VBM}} \quad (5.2)$$

where,

$$\Delta E^{\mathrm{A}}_{\mathrm{VBM}} = \varepsilon^{\mathrm{A}}_{\mathrm{VBM}} - V^{\mathrm{A}}_{\mathrm{bulk}} \quad (5.3)$$

$$\Delta E^{\mathrm{B}}_{\mathrm{VBM}} = \varepsilon^{\mathbf{B}}_{\mathrm{VBM}} - V^{\mathbf{B}}_{\mathrm{bulk}} \quad (5.4)$$

$$\Delta V_{\mathrm{bulk}} = V^{\mathrm{A}}_{\mathrm{bulk}} - V^{\mathbf{B}}_{\mathrm{bulk}} \quad (5.5)$$

$\varepsilon^{\mathrm{i}}_{\mathrm{VBM}}$ and $E^{\mathrm{i}}_{\mathrm{g}}$ are the VBM energy and the bandgap of compound i (= A, B), respectively, that are also obtained solely from the calculations on each bulk unit cell. It should be noted that this method can be only applied to the evaluation of the band edge offsets between the compounds with similar crystal structures and lattice parameters, since one need to prepare the superlattice cell consists of both ones. When the lattice mismatch between the two compounds is small enough, this method will be excellent as it never contains the unphysical error caused by the difference between the surface

structures of the two compounds like method (A). Furthermore, when the bulk potential offset is assumed to be zero, as in the case of estimating the band edge offsets among the same compound with various ionic arrangements (= as was the case in chapter 3 and chapter 4.), one can obtain the band edge offset without performing any calculation on their superlattice.

In method (C), the band edge offset between different two materials (A, B) are evaluated using the core level (ε_c^i, i = A, B) obtained from each unit cell and a core level offset ($\Delta\varepsilon_c$) obtained from a superlattice, as following equations,

$$\Delta E_{\mathrm{VBM}} = \Delta E^{\mathrm{A}}_{\mathrm{VBM},c} - \Delta E^{\mathrm{B}}_{\mathrm{VBM,c}} + \Delta\varepsilon_c \tag{5.6}$$

$$\Delta E_{\mathrm{CBM}} = E_g^{\mathrm{A}} - E_g^{\mathrm{B}} - \Delta E_{\mathrm{VBM}} \tag{5.7}$$

where,

$$\Delta E^{\mathrm{A}}_{\mathrm{VBM,c}} = \varepsilon^{\mathrm{A}}_{\mathrm{VBM}} - \varepsilon_c^{\mathrm{A}} \tag{5.8}$$

$$\Delta E^{\mathrm{B}}_{\mathrm{VBM,c}} = \varepsilon^{\mathrm{B}}_{\mathrm{VBM}} - \varepsilon_c^{\mathrm{B}} \tag{5.9}$$

$$\Delta\varepsilon_c = \varepsilon_c^{\mathrm{A}} - \varepsilon_c^{\mathrm{B}} \tag{5.10}$$

Only $\Delta\varepsilon_c$ needs the calculation on their superlattice, and the other values can be obtained only from the calculations on each unit cell. With this approach, one can appropriately estimate the band edge offsets between the solid-solutions with different compositions, by adopting the deep bands that consist of composition-independent atomic states as their core levels.

Here, in this study, I evaluated the band edge offsets between the different compositions by

method (C), and those between the structural models of the same composition with different ionic orderings by method (B). As the core level used in method (C), I chose La 5s since the La content in $LaMg_xTa_{1-x}O_{1+3x}N_{2-3x}$ is exactly the same in any composition. Then, I obtained $\Delta\varepsilon_c$ by the calculation on the superlattice that consists of the supercell of two compositions conjugates on their bc plane where the lattice mismatch is the smallest, as depicted in Figure 5-12. In the superlattice, the lattice parameter of b and c were set to the average between those of the two compositions.

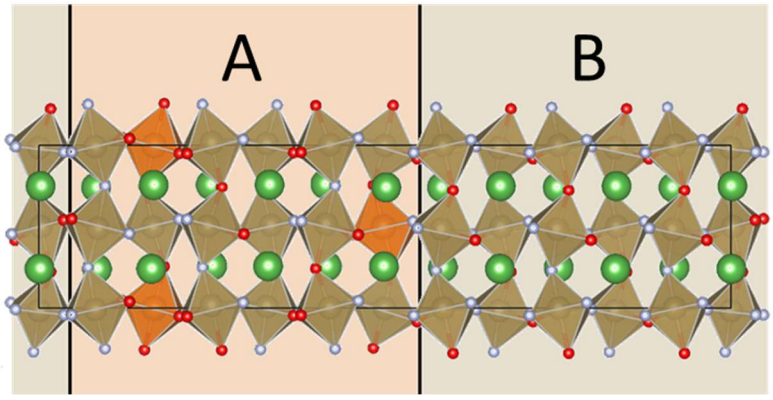

Figure 5-12. The example of superlattice used in the calculation of $\Delta\varepsilon_c$ between two compositions (A and B).

Finally, the thermodynamic stability of $LaMg_xTa_{1-x}O_{1+3x}N_{2-3x}$ at each composition was estimated from both the formation energy ΔE_{f} and the defect energy ΔE_{d} defined in Eq (5.11) and Eq (5.12), respectively.

$$\Delta E_{\mathrm{f}} = E_{\mathrm{bulk}} - \sum_{\mathrm{i}} n_{\mathrm{i}}\,\mu_{\mathrm{i}} \tag{5.11}$$

$$\Delta E_{\mathrm{d}} = E_{\mathrm{defect}} + \sum_{\mathrm{i}} n_{\mathrm{i}}\,\mu_{\mathrm{i}} - E_{\mathrm{bulk}} \tag{5.12}$$

Here, E_{bulk} is the total energy of the bulk model of $LaMg_xTa_{1-x}O_{1+3x}N_{2-3x}$, n_{i} is the number of constituent atom i in its supercell, μ_{i} is the energy of the element substance of i per atom, and E_{defect} is the total energy of the supercell with a defect. The structural data of the elemental substances (La, Mg, Ta, O_2, and N_2) were obtained from Inorganic Material Database (AtomWork) developed by National Institute for Materials Science [29 – 33]. For the estimation of the defect energies, only the N vacancy was taken into account since it is widely considered that the lattice nitrogen in oxynitrides are susceptible to the so called self-oxidation reaction to form N_2 gases. Hence, the structural models at each composition $x \leq 1/2$ with one N vacancy each at several inequivalent anion sites were prepared as shown in Figure 5-13.

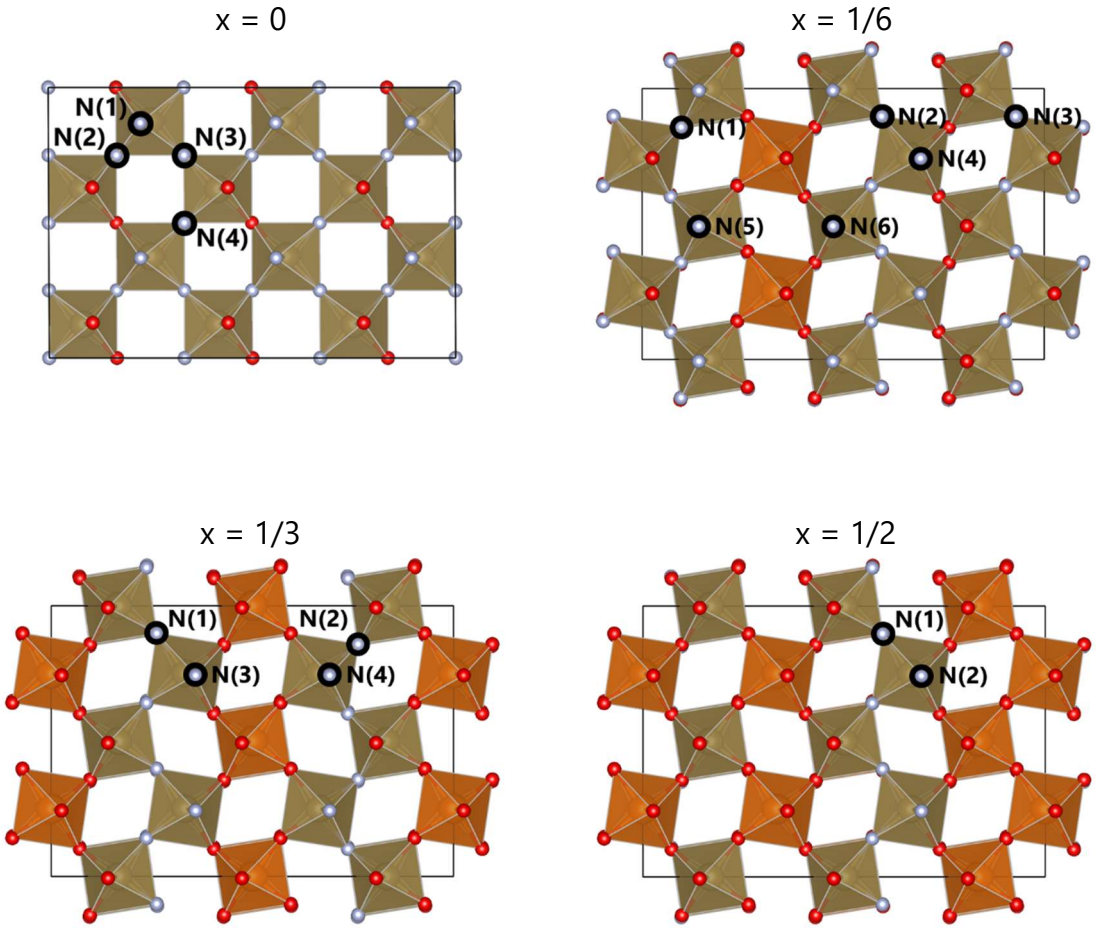

Figure 5-13. The positions of possible inequivalent N vacancies in the structural models at each composition. Brown, orange, red, and blue are Ta, Mg, O, and N atoms, respectively. La atoms are omitted.

5-3. Photocatalyst related properties at each composition

First, calculated lattice parameters, bond angles, and bond lengths of the optimized structural models at each composition are listed in Table 5-3. The calculated lattice parameters decrease with increasing x, denoting the similar tendency to the experimental value [6,7]. Since the calculated bond angles ∠M-X-M (M = Ta, Mg and X = O, N) also monotonically decrease with increasing x, the shrink of the lattice was probably induced by such changes in their bond angles. By comparing the bond angles and the bond lengths around N to those around O, one can notice that ∠Ta-N-Ta is larger than ∠M-O-M in most cases and $r_{Ta\text{-}N}$ is always shorter than $r_{M\text{-}O}$. Such trends strongly indicate the covalency of Ta-N bonds as also discussed in chapter 3 and 4. On the other hand, focusing on the bond lengths around O, one can also find that $r_{Ta\text{-}O}$ decreases with increasing x, while $r_{Mg\text{-}O}$ and $r_{Ta\text{-}N}$ remain almost unchanged. Such trend can be explained by assuming the ionic interactoin in Ta-O bonds, since with increasing x the effective charge of Ta becomes more positive due to the decreased number of N that combines to Ta, and consequently the Ta-O bonds get much stronger. Here, according to these discussion, the decrease in the bond angles ∠M-X-M with increasing x can be attributed to the decrease of anisotoropic bonds around N and the alternative increase of isotropic bonds around O.

Table 5-3.Calculated lattice parameters, bond angles, and bond lengths of the optimized structural model at each composition. The values in the parentheses are the experimental value reported in [6] and [7].

	Lattice parameters (Ang)			Bond angles (deg)					Bond length (Ang)		
x	a	b	c	∠Mg-O-Mg	∠Mg-O-Ta	∠Ta-O-Ta	∠Ta-N-Ta	∠M-X-M	r_{Mg-O}	r_{Ta-O}	r_{Ta-N}
0	11.54 (11.43)	8.13 (8.06)	17.34 (17.25)	--	--	146.3	161.5	156.4	--	2.19	2.04
1/6	17.20 (--)	11.51 (--)	8.11 (--)	--	151.3	151.0	157.6	154.4	2.13	2.13	2.03
1/3	17.08 (17.14)	11.54 (11.38)	8.06 (8.03)	153.9	152.0	149.5	154.8	152.9	2.12	2.12	2.01
1/2	17.00 (17.00)	11.53 (11.32)	8.03 (8.06)	152.7	150.9	153.2	151.9	151.6	2.12	2.08	2.01
2/3	16.88 (16.85)	11.51 (11.34)	8.03 (7.96)	152.1	149.7	--	--	150.5	2.12	2.01	--
Ave	**--**	**--**	**--**	**152.9**	**151.0**	**150.0**	**156.4**	--	**2.12**	**2.11**	**2.02**

Next, the bandgaps at different compositions were compared. Figure 5-14 shows the calculated bandgap of $LaMg_xTa_{1-x}O_{1+3x}N_{2-3x}$ as a function of its composition. The bandgap of $LaMg_xTa_{1-x}O_{1+3x}N_{2-3x}$. monotonically increases with incrrease in compostion x. This is probably because the contribution of O 2p which has a deeper energy level increased in the valence band that consists of O 2p and N 2p orbitals, with increase in O/N ratio at larger x, as discussed in the later section. The calculated bandgap was 1.9 eV ~ at x = 0 and 4.2 eV ~ x = 2/3, both of which reproduce the experimentally reported absorption edge of $LaMg_xTa_{1-x}O_{1+3x}N_{2-3x}$ (1.93 eV and 4.55 eV, respectively [2, 7]). Here, since the bandgaps at $x \geq 1/2$ are much larger than the energy of visible light, x should be less than or equal to 1/3 in terms of the bandgap. It should be noted that the bandgap changes much more significantly between x = 1/2 and 2/3 than between the other two compositions. Such behavior was probably caused by the extinction of the contribution of N 2p that has a relatively higher energy level than O 2p. A similar trend, so-called “band bowing”, had also been observed in the previous experiments [3].

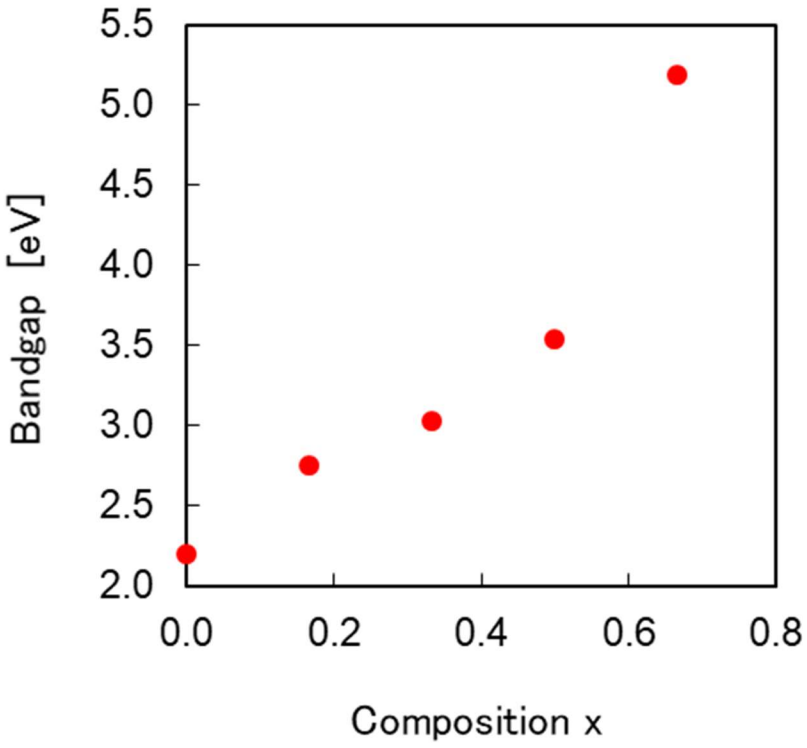

Figure 5-14 The calculated bandgap of $LaMg_xTa_{1-x}O_{1+3x}N_{2-3x}$ as a function of its composition.

Next, the band structure at each composition was shown in Figure 5-15. At most compositions, CBM (Conduction Band Maximum) appears at Γ point except for at x = 1/3, whose CBM appears at Y point and its band energy is still quite similar to the one at Γ point. On the other hand, VBM (Valence Band Minimum) appears at different points depending on the compositions, though its band energy were found to be similar to those at several other symmetry points, as was the case for CBM.

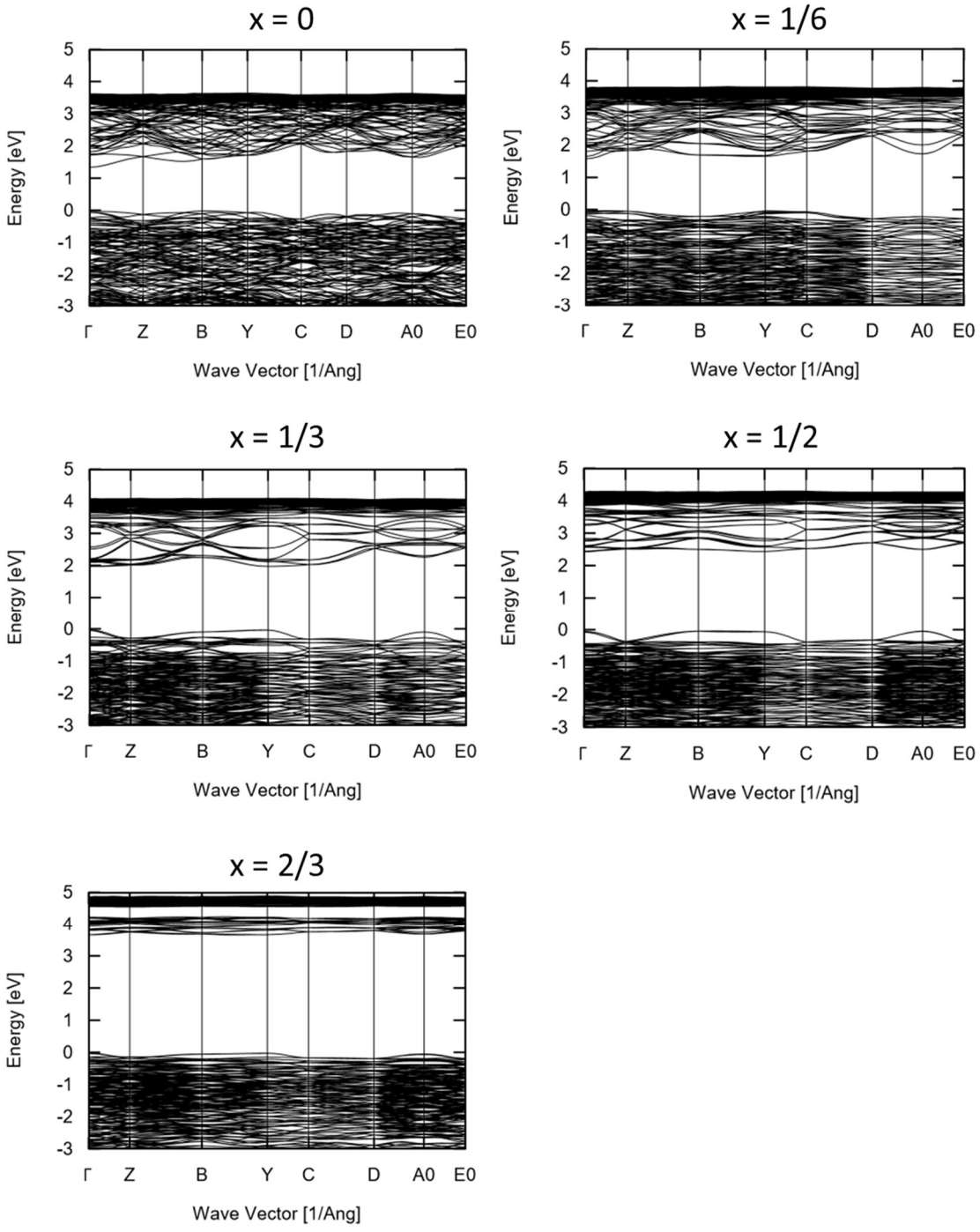

Figure 5-15 The band structure of each composition.

Subsequently, the carrier effective masses of $LaMg_xTa_{1-x}O_{1+3x}N_{2-3x}$ with different compositions were listed in Table 5-4. The electron effective mass (m_e^*) monotonically decreased with increasing x, suggesting that the dispersion of the conduction band was reduced. This is probably due to the reduced overlap among Ta 5d orbitals, as also mentioned later, since the Ta/Mg ratio gets lowered with the increase in x. In particular, the electron effective mass at x = 2/3 is significantly large, and thus the electron diffusion at this composition is expected to be poor.

On the other hand, the hole effective mass (m_h^*) became smaller at the intermediate compositions ($1/6 \leq x \leq 1/2$), and thus an enhanced hole diffusion within such composition range was expected. Combined with the discussion on the electron effective mass, $LaMg_xTa_{1-x}O_{1+3x}N_{2-3}$ solid solutions at relatively smaller composition (1/6 ~ 1/3) will be efficient as a photocatalyst in terms of carrier diffusions.

Additionally, focusing on the carrier effective mass along each direction, one can find that they are partially anisotropic depending on the composition. For instance, at x = 2/3, the electron effective mass along Γ → Z (= the direction of b-axis) is rather small as 2.5, while that along Γ → Y (= the direction of a-axis) and Γ → B (= the direction of c-axis) and are extremely large. Such anisotropy probably corresponds to the cation ordering in the structural model where Ta are arranged only along the direction of b-axis (see Figure 5-11). Similarly, at x = 1/2 and x = 1/3 the electron effective mass along Γ → Y and Y → Γ, respectively, is extremely large in accordance with the

separation of Ta along the direction of a-axis in their structural models. On the other hand, electron effective masses at the composition $x \leq 1/6$ is nearly isotropic. This is probably because the Ta content is rather high at such compositions, and thus Ta cations are not divided along any directions.

Table 5-4. (a) Electron effective masses m_e^* of $LaMg_xTa_{1-x}O_{1+3x}N_{2-3x}$ with different compositions along each direction. Note that at x = 1/3 the VBM appeared on Y as shown in the parentheses.

x	$\Gamma \rightarrow A_0$	$\Gamma \rightarrow B$	$\Gamma \rightarrow C$	$\Gamma \rightarrow D$	$\Gamma \rightarrow E_0$	$\Gamma \rightarrow Y$	$\Gamma \rightarrow Z$	**Ave**
0	0.28	0.44	0.44	0.72	0.39	0.37	0.72	**0.43**
1/6	1.36	1.47	0.60	0.70	0.90	1.02	0.35	**0.74**
1/3	0.85 ($Y \rightarrow A_0$)	1.04 ($Y \rightarrow B_0$)	3.12 ($Y \rightarrow C_0$)	1.32 ($Y \rightarrow D_0$)	1.11 ($Y \rightarrow E_0$)	30.85 ($Y \rightarrow G_0$)	5.54 ($Y \rightarrow Z_0$)	**1.62**
1/2	3.25	3.06	1.40	1.76	1.92	23.69	1.01	**2.02**
2/3	-17.85	-15.59	3.65	11.61	13.98	55.57	2.49	**9.57**

Table 5-4. (b) Hole effective masses m_h^* of $LaMg_xTa_{1-x}O_{1+3x}N_{2-3x}$ with different compositions along each direction. Note that at x = 0, 1/6, 1/2 the VBMs appeared B, Y and A_0, respectively, as shown in the parentheses.

x	$\Gamma \rightarrow A_0$	$\Gamma \rightarrow B$	$\Gamma \rightarrow C$	$\Gamma \rightarrow D$	$\Gamma \rightarrow E_0$	$\Gamma \rightarrow Y$	$\Gamma \rightarrow Z$	**Ave**
0	39.96 ($B \rightarrow A_0$)	2.05 ($B \rightarrow C$)	0.95 ($B \rightarrow D$)	1.77 ($B \rightarrow E$)	5.91 ($B \rightarrow G$)	7.30 ($B \rightarrow Y$)	1.22 ($B \rightarrow Z$)	**2.15**
1/6	0.39 ($Y \rightarrow A_0$)	0.47 ($Y \rightarrow B_0$)	4.52 ($Y \rightarrow C_0$)	0.64 ($Y \rightarrow D_0$)	0.55 ($Y \rightarrow E_0$)	16.51 ($Y \rightarrow G_0$)	15.49 ($Y \rightarrow Z_0$)	**0.83**
1/3	6.57	5.50	0.68	1.49	1.73	67.94	0.48	**1.35**
1/2	-47.56 ($A_0 \rightarrow B$)	1.45 ($A_0 \rightarrow C$)	0.73 ($A_0 \rightarrow D$)	0.50 ($A_0 \rightarrow E$)	-18.46 ($A_0 \rightarrow G$)	23.87 ($A_0 \rightarrow Y$)	1.89 ($A_0 \rightarrow Z$)	**1.53**
2/3	-17.85	-15.59	3.65	11.61	13.98	55.57	2.49	**2.04**

Next, the band edge positions of $LaMg_xTa_{1-x}O_{1+3x}N_{2-3x}$ at each composition were shown in Figure 5-16. Their CBM positions were nearly constant over all compositions except x = 2/3, probably due to the common structure of their conduction bands that mainly consist of Ta 5d. The elevated CBM position at x = 2/3 is thought to be the consequence of the reduced band dispersion due to the decreased content of Ta in $LaMg_xTa_{1-x}O_{1+3x}N_{2-3x}$. Here, since all the CBM positions are far more negative than the hydrogen evolution potential (0 V_{NHE}), it is expected that the photoexcited electrons in $LaMg_xTa_{1-x}O_{1+3x}N_{2-3x}$ are active enough to produce hydrogen over all compositions.

On the other hand, the VBM positions of $LaMg_xTa_{1-x}O_{1+3x}N_{2-3x}$ were monotonically lowered with increasing x, probably due to the reduced contribution of N 2p and the alternatively increased contribution of O 2p in the valence band. At x = 0, the VBM is positioned just below the oxygen evolution potential (1.23 V_{NHE}), and thus the oxidation activity of $LaMg_xTa_{1-x}O_{1+3x}N_{2-3x}$ is expected to be poor at this composition. By contrast, the VBM positions at the compositions more than or equal to 1/6 are sufficiently positive than the oxygen evolution potential. Hence, the holes generated in $LaMg_xTa_{1-x}O_{1+3x}N_{2-3x}$ ($x \geq 1/6$) are expected to have enough ability to oxidize water into oxygen.

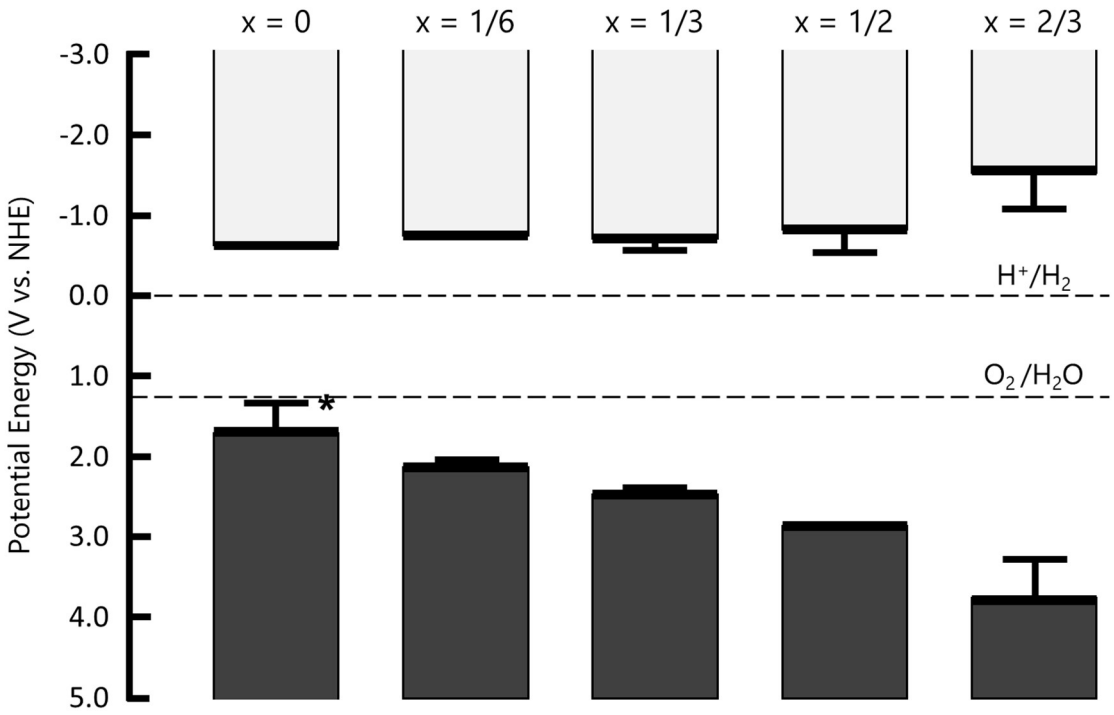

Figure 5-16. The band edge positions of $LaMg_xTa_{1-x}O_{1+3x}N_{2-3x}$ at each composition. The band edge positions were aligned by setting the VBM position of the structural model at x = 0 with the smallest bandgap (*) to the experimental value (+1.31 V vs. NHE) [3].

Finally, the formation energies ΔE_f and the defect energy ΔE_d of $LaMg_xTa_{1-x}O_{1+3x}N_{2-3x}$ at different compositions are listed in Table 5-5. The formation energy monotonically decreases with increasing x, reflecting the general trend that oxides are more chemically stable than nitrides. Such trend indicates that the degradation of the crystals will more easily occur at smaller x due to the lowered stabilities. Besides, since the defect energy increases with increasing x, the easier formation

of N vacancies at smaller x is also indicated. Such trend is probably related to the stabilization of the TaX_5 (X = O, N) unit where the N vacancy was formed, since the defect energy monotonically decreases with the increasing number of N in the TaX_5 unit. All these results strongly indicate the greater susceptibility of $LaMg_xTa_{1-x}O_{1+3x}N_{2-3x}$ to degradation at the smaller x, which is also confirmed from the experimental results where the self-oxidation of N^{3-} was observed only at the composition x < 0.2 [3].

Table 5-5. The formation energies and the defect tolerances of $LaMg_xTa_{1-x}O_{1+3x}N_{2-3x}$ at different compositions. The values in parentheses are the number of remaining N in the two TaX_5 unit where the N vacancy was formed.

x	ΔE_f (eV/FU)	ΔE_d (eV)					
		N(1)	N(2)	N(3)	N(4)	N(5)	N(6)
0	-10.00	3.38 (3,3)	2.72 (3,3)	3.29 (3,3)	2.74 (3,3)	--	--
1/6	-11.53	3.02 (3,3)	3.26 (2,3)	3.15 (2,3)	2.89 (3,3)	2.82 (3,3)	3.64 (2,2)
1/3	-13.05	3.61 (2,2)	3.61 (2,2)	3.84 (2,2)	3.60 (2,2)	--	--
1/2	-14.54	3.86 (1,2)	4.15 (0,2)	--	--	--	--
2/3	-16.04	--	--	--	--	--	--

5-4. Detailed discussion on the variation of electronic structures

For further discussion on the electronic structure of $LaMg_xTa_{1-x}O_{1+3x}N_{2-3x}$ at each composition, the density of states (DOS) and the projected density of states (PDOS) were shown in Figure 5-17. As already mentioned in the previous sections, it was found that the valence band and the conduction band consist of anion 2p and Ta 5d, respectively, over all compositions.

Figure 5-17 also shows that the width of the conduction band decreases with increasing x, probably reflecting the reduced overlap among Ta 5d orbitals due to the decreased content of Ta in $LaMg_xTa_{1-x}O_{1+3x}N_{2-3x}$. Additionally, the onset of the conduction band gets steeper as x increases, indicating the decrease of the band dispersion near the bottom of conduction bands and the consequent increase of the electron effective masses.

It should be noted that the conduction band width drastically decreases between x = 1/2 and x = 2/3, while their widths are not so different among the other compositions. This is probably because at the composition between x = 0 to x = 1/2 Ta^{5+} cations are connected to each other via the bonding units of Ta^{5+}-N^{3-}-Ta^{5+}, since N^{3-} can only combine to Ta^{5+} (*i.e.* the chemical bond between N^{3-} and Mg^{2+} are significantly weak), as mentioned in section 5-2-1. In other words, Ta^{5+} cations are partially localized in the crystals of $LaMg_xTa_{1-x}O_{1+3x}N_{2-3x}$ ($x \leq 1/2$) by gathering around N^{3-} anions to prevent the formation of N-Mg bonds, although the Ta/Mg cations prefers delocalized arrangements in oxides. Then, such partial localization of Ta creates a kind of “Ta-rich domains” in the crystals, and

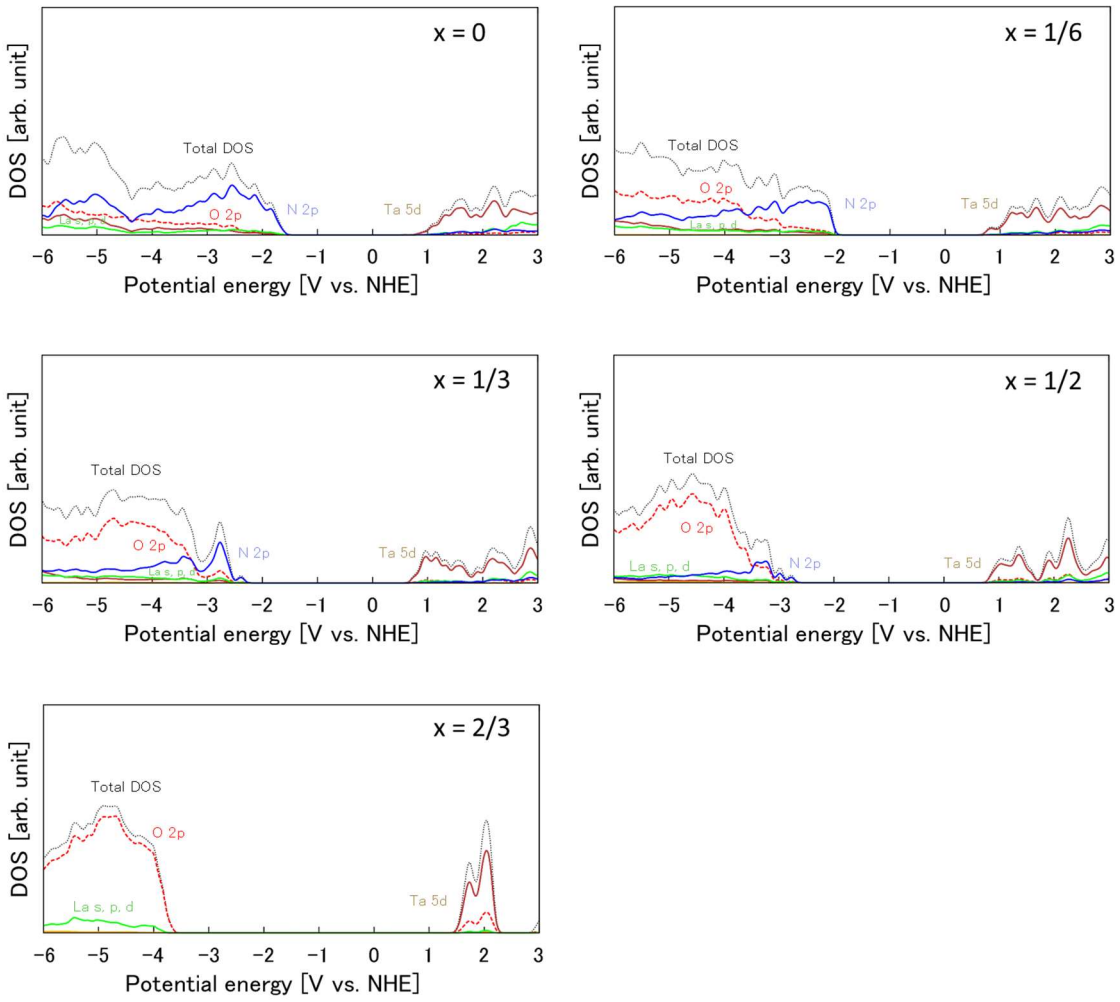

Figure 5-17. The density of states (DOS) and the projected density of states (PDOS) calculated within HSE06 level. The energy positions are aligned with the band positions depicted in Figure 5-16.

consequently the wide dispersion of the conduction band remains due to the retained large overlap among Ta 5d, even when the Ta content is rather low.

On the other hand, for the valence bands in Figure 5-17, it was confirmed that the contribution of N 2p decreases and that of O 2p alternatively increases with increasing x. As already mentioned, such trend is consistent with the increasing O/N ratio in $LaMg_xTa_{1-x}O_{1+3x}N_{2-3x}$. It was also revealed that the onsets of the valence bands are obviously steep at x = 0 and x = 2/3, while they are relatively moderate at intermediate compositions. In particular, at x = 1/6 and x = 1/3, a small contribution of N 2p appeared around the upper region of the valence band, and the mixing between N 2p and O 2p was considered to be the origin of the smooth onsets of their valence bands. Such trend is also consistent with the calculated effective masses of holes shown in Table 5-3.

Here, it should be noted that at $x \leq 1/6$, the DOS of the valence band around its upper region is almost dominated by the contribution of N 2p. This indicates that the holes generated by the photoexcitation will finally be localized only on N^{3-}, which are more susceptible to the self-oxidation reaction (Eq (5.12)) than O^{2-}.

$$2N^{3-} + 6h^{+} \rightarrow N_2 \qquad (5.12)$$

Thus, it is expected that at $x \leq 1/6$ the generated holes will be consumed in the self-oxidation of N^{3-} rather than in water oxidation. Indeed, such consideration supports the experimental results of the photocatalytic activity as the function of the composition [3]. On the other hand, at $x \geq 1/3$, there

appears not only the contribution of N 2p but also that of O 2p in the valence band around its upper region. Such mixing between the two states enables the holes to be delocalized over both anions, and thus the water oxidation activity will be improved due to the reduced self-oxidation of N^{3-}.

Based on the results above, the maximized photocatalytic activity of $LaMg_xTa_{1-x}O_{1+3x}N_{2-3x}$ at x = 1/3 can be explained as follows. Originally, the pure oxynitride $LaTaO_2N$ (x = 0) has smaller bandgap (1.9 eV ~ 2.2 eV) than the solid solution at any other composition, and this makes $LaTaO_2N$ an appealing candidate for a photocatalyst. However, as a trade-off for such a small bandgap, it also has a lot of drawbacks such as a VBM position which is too negative, a valence band whose upper region consists only of N 2p, poor chemical stability, and being susceptible to self-oxidations and defect formations. On the other hand, by increasing the O content by forming solid solutions with $LaMg_{2/3}Ta_{1/3}O_3$, not only the VBM positions gets lowered but also the dispersion of the valence band increases and the self-oxidations of N^{3-} are reduced due to the mixing between N 2p and O 2p. Note that, since the greatly increased O content will open the bandgaps and reduce the dispersion of the conduction bands, the composition x should not be more than 1/3. In other words, the drawbacks of $LaTaO_2N$, an appealing narrow gap photocatalyst, are compensated by a partial substitution of N with O in the solid solutions $LaMg_xTa_{1-x}O_{1+3x}N_{2-3x}$, especially at x = 1/3.

5-5. Conclusion

In this research, the dependence of the band structure of $LaMg_xTa_{1-x}O_{1+3x}N_{2-3x}$, a solid solution between $LaMg_{2/3}Ta_{1/3}O$ and $LaTaO_2N$, on its composition was investigated by means of first principle calculations. In particular, I aimed to identify the factors that make its activity reach the highest at the composition x = 1/3, by estimating and comparing the photocatalytic related properties such as bandgaps, band edge positions, carrier effective masses, and chemical stabilities of $LaMg_xTa_{1-x}O_{1+3x}N_{2-3x}$ at each composition.

As a consequence, their VBM positions were demonstrated to be monotonically decreased with increasing x, accompanied with the widening of the bandgaps. This was caused by the decrease and the extinction of the N 2p contribution and the alternative increase of the O 2p contribution in their valence bands. On the other hand, by comparing the carrier effective mass at each composition, it was revealed that the electron effective mass monotonically increases with the increase in x, while the hole effective mass becomes smaller at the intermediate compositions. Such trends reflect the variation in the band dispersions near their edge regions due to the reduced or the increased overlap of their constituent orbitals.

Based on these results, the reason why the photocatalytic activity of $LaMg_xTa_{1-x}O_{1+3x}N_{2-3x}$ reaches the highest at x = 1/3 can be explained as follows. First, $LaMg_xTa_{1-x}O_{1+3x}N_{2-3x}$ satisfies both a narrower bandgap that corresponds to the energy of visible light and a VBM position which is positive

enough to oxidize water at the composition between x = 1/6 to x = 1/3. Additionally, the mixing of N 2p and O 2p in the valence band at x = 1/3 will increase its dispersion and reduce the self-oxidation of N^{3-}. Hence, the carrier diffusion will be improved, and thus its activity will be maximized at this composition.

Bibliography

[1] Pan, C.; Takata, T.; Nakabayashi, M.; Matsumoto, T.; Shibata, N.; Ikuhara, Y.; Domen K. A Complex Perovskite-Type Oxynitride: The First Photocatalyst for Water Splitting Operable at up to 600 nm. *Angew. Chem. Int. Ed.* **2015**, *54*, 2955.

[2] Pan, C.; Takata, T.; Domen K. Overall Water Splitting on the Transition-Metal Oxynitride Photocatalyst $LaMg_{1/3}Ta_{2/3}O_2N$ over a Large Portion of the Visible light Spectrum. *Chem. Eur. J.*, **2016**, *22*, 1854.

[3] Pan, C.; Takata, T.; Kumamoto, K.; Ma, S. S. K.; Ueda, K.; Minegishi, T.; Nakabayashi, M.; Matsumoto, T.; Shibata, N.; Ikuhara, Y.; Domen K. Band engineering of perovskite-type transition metal oxynitrides for photocatalytic overall water splitting. *J. Mater. Chem. A* **2016**, *4*, 4544.

[4] Takata, T.; Pan, C.; Nakabayashi, M.; Shibata, N.; Domen K. Fabrication of a Core-Shell-Type Photocatalyst via Photodeposition of Group IV and V Transition Metal Oxyhydroxides: An Effective Surface Modification Method for Overall Water Splitting. *J. Am. Chem. Soc.*, **2015**, *137*, 9627.

[5] Xu, J.; Pan, C.; Takata, T.; Domen K. Photocatalytic overall water splitting on the perovskite-type transition metal oxynitride $CaTaO_2N$ under visible light irradiation. *Chem. Commun.* **2015**, *51*, 7191.

[6] Clark, L.; Oró-Solé, J.; Knight, K. S.; Fuertes, A.; Attfield J. P. Thermally Robust Anion-Chain Order in Oxynitride Perovskites. *Chem. Mater.* **2013**, *25*, 5004.

[7] Kim, Y. Ph.D. Thesis, The Ohio State University, 2005. “SYNTHESES, CRYSTAL

STRUCTURES, AND DIELECTRIC PROPERTY OF OXYNITRIDE PEROVSKITES."

[8] King, G.; Woodward P. M. Cation ordering in perovskites. *J. Mater. Chem.* **2010**, *20*, 5785–5796.

[9] Anderson, M. T.; Greenwood, K. B.; Taylor, G. A.; Poeppelmeier, K. R. B-CATION ARRANGEMENTS IN DOUBLE PEROVSKITES. *Pros. Solid. St. Chem.* **1993**, *22*, 197.

[10] Fuertes, A. Metal oxynitrides as emerging materials with photocatalytic and electronic properties. *Mater. Horiz.* **2015**, *2*, 453.

[11] Wolff, H.; Lerch, M.; Schilling, H.; Bähtz C.; Dronskowski, R. A density functional study on the stability of anatase type phases in the system Mg-Ta-O-N. *J. Solid State Chem.* **2008**, *181*, 2684.

[12] Kresse, G.; Hafner, J. Ab. initio molecular dynamics for liquid metals. *Phys. Rev. B: Condens. Matter Mater. Phys.* **1993**, *47*, 558.

[13] Kresse, G.; Hafner, J. Ab initio molecular-dynamics simulation of the liquid-metal−amorphous semiconductor transition in germanium. *Phys. Rev. B: Condens. Matter Mater. Phys.* **1994**, *49*, 14251.

[14] Kresse, G.; Furthmü ller, J. Efficiency of ab-initio total energy calculations for metals and semiconductors using a plane-wave basis set. *Comput. Mater. Sci.* **1996**, *6*, 15.

[15] Kresse, G.; Furthmü ller, J. Efficient iterative schemes for ab initio total-energy calculations using a plane-wave basis set. *Phys. Rev. B: Condens. Matter Mater. Phys.* **1996**, *54*, 11169.

[16] Perdew, J. P.; Burke, K.; Ernzerhof, M. Generalized Gradient Approximation Made Simple. *Phys. Rev. Lett.* **1996**, *77*, 3865.

[17] Blöchl, P. E. Projector augmented-wave method. *Phys. Rev. B: Condens. Matter Mater. Phys.* **1994**, *50*, 17953.

[18] Kresse, G.; Joubert, D. From ultrasoft pseudopotentials to the projector augmented-wave method. *Phys. Rev. B: Condens. Matter Mater. Phys.* **1999**, *59*, 1758.

[19] Heyd, J.; Scuseria, G. E.; Ernzerhof, M. Hybrid functionals based on a screened Coulomb potential. *J. Chem. Phys.* **2003**, *118*, 8207.

[20] Heyd, J.; Scuseria, G. E.; Ernzerhof, M. Erratum: Hybrid functionals based on a screened Coulomb potential. *J. Chem. Phys.* **2006**, *124*, 219906.

[21] Paier, J.; Marsman, M.; Hummer, K.; Kresse, G.; Gerber, I. C.; Angyan, J. G. Screened hybrid density functionals applied to solids. *J. Chem. Phys.* **2006**, *125*, 249901.

[22] Toroker, M. C.; Kanan, D. K.; Alidoust, N.; Isseroff, L. Y.; Liao, P.; Carter, E. A. First principles scheme to evaluate band edge positions in potential transition metal oxide photocatalysts and photoelectrodes. *Phys. Chem. Chem. Phys.* **2011**, *13*, 16644.

[23] Kubo, A.; Giorgi, G.; Yamashita, K. Anion Ordering in $CaTaO_2N$: Structural Impact on the Photocatalytic Activity. Insights from First-Principles. *Chem. Mater*. **2017**, *29*, 539.

[24] Ping, Y.; Rocca, D.; Galli, G. Electronic excitations in light absorbers for photoelectrochemical energy conversion: first principles calculations based on many body perturbation theory. *Chem. Soc. Rev.* **2013**, *42*, 2437.

[25] Colombo, L.; Resta, R.; Baroni, S. Valence-band offsets at strained Si/Ge interfaces. *Phys. Rev. B* **1991**, *44*, 5572.

[26] Wei, S.-H.; Zunger, A. Calculated natural band offsets of all II–VI and III–V semiconductors: Chemical trends and the role of cation d orbitals. *Appl. Phys. Lett.* **1998**,*72*, 2011.

[27] Nelson, A. J.; Schwerdtfeger, C. R.; Wei, S.-H.; Zunger, A.; Rioux, D.; Patel, R.; Höchst H. Theoretical and experimental studies of the ZnSe/$CuInSe_2$ heterojunction band offset. *Appl. Phys. Lett.* **1993**, *62*, 2557.

[28] Huang, W. L. First-principles determination of the absolute band-edge positions of BiOX (X = F, Cl, Br, I). *Comput. Mater. Sci.* **2012**, *55*, 166.

[29] Xu, Y.; Yamazaki, M.; Villars P. Inorganic Materials Database for Exploring the Nature of Material. *Jpn. J. Appl. Phys.* **2011**, *50*, 11RH02.

[30] National Institute for Materials Science (NIMS) AtomWork <http://crystdb.nims.go.jp/>

[31] Che, G.C.; Liang J.; Yi Y. *Jinshu Xuebao (Journal of Metallurgy)*,**1986**, *22*, B206.

[32] Vavilova, V. V.; Galkin, L.N.; Glazov, M.V.; Kovneristyi, Y. K.; Barmin, Y. V.; Zolotukhin, I. V.; Obvintsev, Y. A. Stabilization by Rapid Quenching of the Phase Having delta-Mn Structure in the Rhenium—Tantalum System. *Dokl. Phys. Chem*. **1988**, *300*, 531.

[33] Karen P.; Kjekshus A.; Huang Q.; Karen V. L. The crystal structure of magnesium dicarbide *J. Alloys Compd*. **1999**, *282*, 72.

Chapter 6.

Elucidation and Control of Defects in Solid Solution Photoelectrode: A Demonstration on $(ZnSe)_{0.85}(CuIn_{0.7}Ga_{0.3}Se_2)_{0.15}$

6-1. Introduction to $(ZnSe)_{0.85}(CuIn_{0.7}Ga_{0.3}Se_2)_{0.15}$ photocathode

6-1-1. Development of chalcopyrite-based photocathodes

As already mentioned in the chapter 1, water splitting photoelectrode systems are getting wide attention as well as water splitting photocatalysts. Photoelectrode systems have several advantages over photocatalyst based ones, since their reaction sites of oxygen and hydrogen are separated, and less restrictions for their band edge positions make it possible to utilize the materials with narrower bandgaps that can absorb wider range of solar energy.

As a photocathode material which is used for hydrogen evolution in photoelectrode system, Kumagai *et al.* had reported that $CuIn_{0.7}Ga_{0.3}Se_2$(hereafter CIGS), a well-known chalcopyrite-based photovoltaic material, produced a remarkable cathodic photocurrent up to 30 mA cm^{-2} at 0 V_{RHE} under AM 1.5G simulated sunlight [1]. However, the onset potential of CIGS photocathode is only about 0.7 V_{RHE}, which is still not sufficient to achieve high photocurrent when combined to photoanode material for oxygen evolution.

Then, Kaneko *et al.* had developed $(ZnSe)_{0.85}(CuIn_{0.7}Ga_{0.3}Se_2)_{0.15}$ (hereafter $(ZnSe)_x(CIGS)_{1-x}$) as a solid solution of CIGS and ZnSe, the latter of which has a lower VBM position, and achieved a higher onset potential up to 0.89 V_{RHE} [2]. Note that CIGS and ZnSe can easily form a solid solution, since their basic structures are common (ZnSe: zinc blende, CIGS: chalcopyrite) and their lattice mismatch is only about 1 % [2]. $(ZnSe)_x(CIGS)_{1-x}$ was synthesized by co-evaporation method onto a soda-lime glass substrate, and it showed the highest photocurrent at the composition of $x = 0.85$. Although its photocurrent is still only up to 12 mA cm^{-2} [3], $(ZnSe)_x(CIGS)_{1-x}$ is thought to be a promising photocathode material and is now intensively studied to improve its activity by optimizing the synthesizing process [3,4].

6-1-2. Unexplained behaviors of point defects

However, there remains an important subject to understand the properties of $(ZnSe)_x(CIGS)_{1-x}$, *i.e.* the behaviors of the point defects in $(ZnSe)_x(CIGS)_{1-x}$ have not been well studied yet, and thus the origin of its semiconductor characteristics is still unraveled. For instance, $(ZnSe)_{0.85}(CIGS)_{15}$ shows p-type characteristic though ZnSe itself, a constituent that dominates the most part of this material, is essentially an n-type semiconductor. Although the rest part of this material, CIGS, is still a p-type semiconductor due to Cu vacancy (V_{Cu}) acceptors [5], V_{Cu} is unlikely the dominant origin of the p-type characteristics of $(ZnSe)_{0.85}(CIGS)_{15}$ since the atomic content of Cu is only up to 15 %, and some antisite defects such as Zn_{Cu} can also be created. Furthermore, while CIGS shows enhanced p-type characteristics under Cu-poor conditions, $(ZnSe)_x(CIGS)_{1-x}$ shows n-type characteristics under the same condition [6]. These differences are attributed to the different defect structures between solid solution ($(ZnSe)_x(CIGS)_{1-x}$) and non-solid solution (CIGS), but the details of their defects have not been confirmed by experiments.

6-1-3. Research objectives

Here, in this research, I aimed to clarify the structures and the properties of the point defects in $(ZnSe)_x(CIGS)_{1-x}$ solid solution by means of first principle calculations. In particular, I will identify the dominant defects that determine the properties of $(ZnSe)_x(CIGS)_{1-x}$ by evaluating and comparing the formation energies of various defect structures. Furthermore, I will estimate the concentration of each defect and carrier from the calculated formation energies, to predict their dependence on growth conditions such as temperature and partial pressure, and to compare them to experimental results.

6-2. Computational details

In this study, the structural models of defects in $(ZnSe)_x(CIGS)_{1-x}$ were prepared and the defect formation energies were compared by means of first principle calculations. Subsequently, the dependence of the defect formation energies on the temperature and the partial pressure was investigated in order to provide the guidelines to control the defects in this material.

6-2-1. Structural models

First, I prepared the structural model of the bulk $(ZnSe)_x(CIGS)_{1-x}$ solid solution. The bulk structures are created by multiplying the unit cell of ZnSe (space group $F\bar{4}3m$, cubic, a = 5.62 Å, 8 atoms [7]), and one fourth of its Zn atoms were substituted by Cu, In, and Ga atoms. Here, the Zn/Cu ratio was fixed to 6 in order to reflect the experimental value (15 %).

To study the specific features of the cation ordering in bulk $(ZnSe)_x(CIGS)_{1-x}$, I initially prepared several structural models of the bulk using 1 × 1 × 2 supercell (16 atoms) and 1 × 2 × 2 supercell (32 atoms). For simplicity, Ga atoms were not included, and indeed the bulk structural models of $(ZnSe)_x(CIS)_{1-x}$ were prepared. All structural models are shown in Figure 6-1 and Figure 6-2. Since ZnSe and CIGS are II-VI and I-III-VI semiconductors, respectively, $(ZnSe)_x(CIGS)_{1-x}$ become a non-isovalent alloy [8, 9], where the octet-rule violation around Se atoms can occur depending on the arrangement of Zn, Cu, In and Ga in their structural models. Thus, the number of non-isovalent Se atoms (= Se atoms which break the octet-rule. Hereafter, a Se atom breaking the octet-rule with ±1

electron will be called “non-isovalent-1 Se” and that with ± 2 electron will be called “non-isovalent-2 Se”) in each structural model was written below each figure.

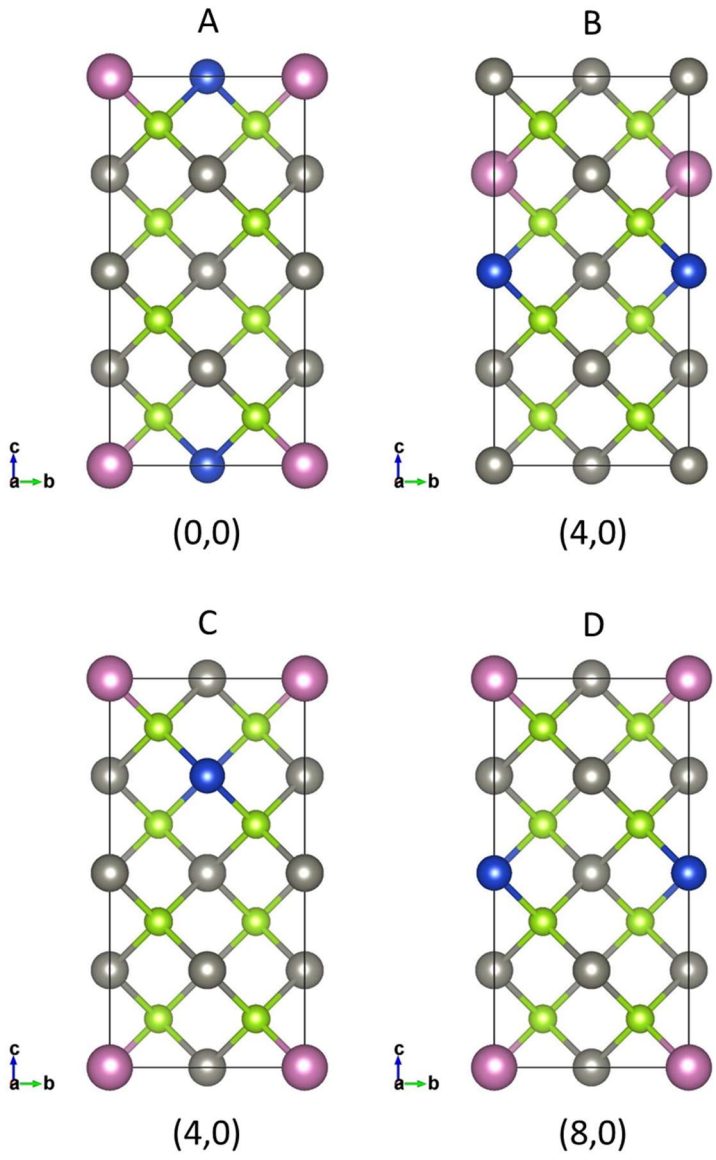

Figure 6-1. Structural models of the $(ZnSe)_x(CIGS)_{1-x}$, using 1 × 1 × 2 supercell (16 atoms). The numbers in the parenthesis correspond to (The number of “non-isovalent-1 Se”, The number of “non-isovalent-2 Se”). Gray, blue, pink, and light green are Zn, Cu, In, and Se atoms, respectively.

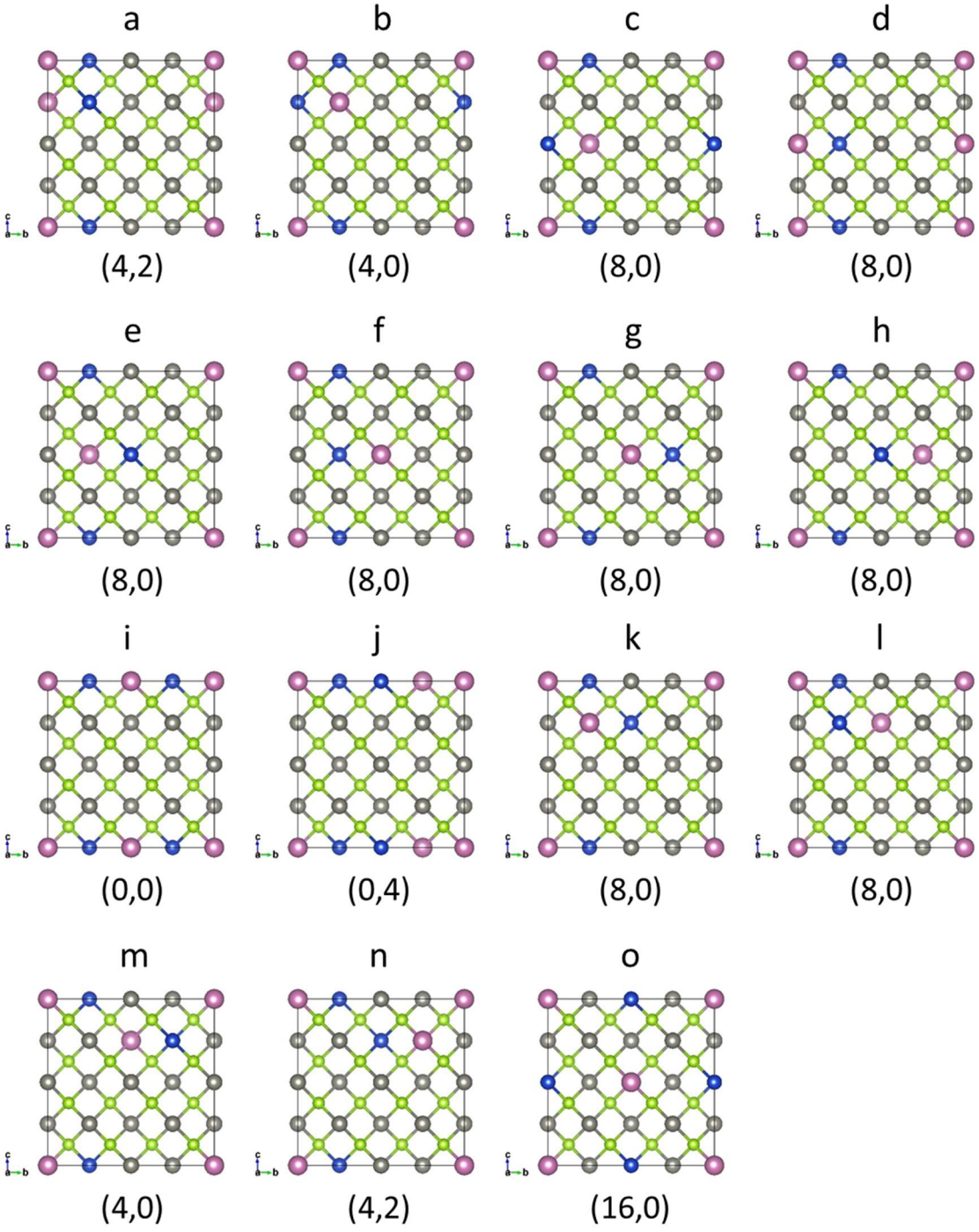

Figure 6-2. Structural models of the $(ZnSe)_x(CIGS)_{1-x}$, using 1 × 2 × 2 supercell (32 atoms). The numbers in the parenthesis correspond to (The number of "non-isovalent-1 Se", The number of "non-isovalent-2 Se"). Gray, blue, pink, and light green are Zn, Cu, In, and Se atoms, respectively.

Subsequently, all the above structures were geometrically optimized, and the total energy of each optimized structure was obtained by first-principle calculations as described later. As a consequence, it was found that the structures which obey the octet-rule are always more stable than those which violates the octet-rule. In addition, according to the Figure 6-3 and Figure 6-4 where "the number of non-isovalent Se vs. the total energy trend" was shown, it was also confirmed that the structural model becomes destabilized by 100 meV per four non-isovalent Se atoms. A similar trend was also reported by a previous study on CIGS using first principle calculations, where Cu, In and Ga atoms were found to be arranged to follow the octet-rule in the most stable structure [10]. So, hereafter, I will only consider the structural models without any octet-violation, whose Cu, In, and Ga atoms are always placed in planer arrangements as is the case in model A in Figure 6-1 and model i in Figure 6-2.

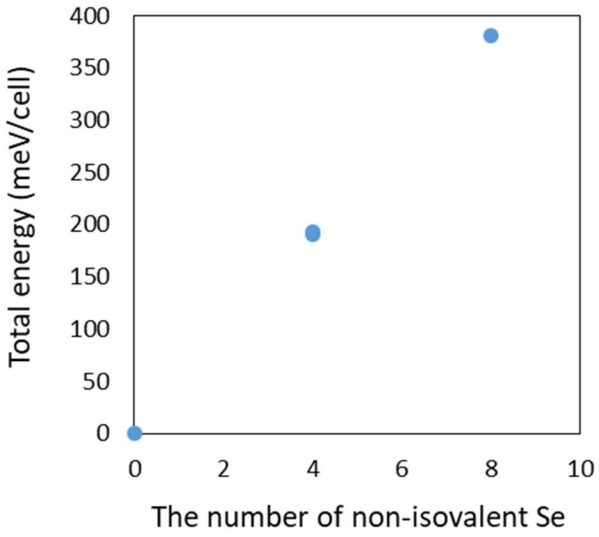

Figure 6-3. The number of non-isovalent Se vs. the relative total energy trend obtained from the calculations on 1 × 1 × 2 supercells. The number of non-isovalent Se is defined as "the number of "non-isovalent-1 Se" + 2 × The number of "non-isovalent-2 Se".

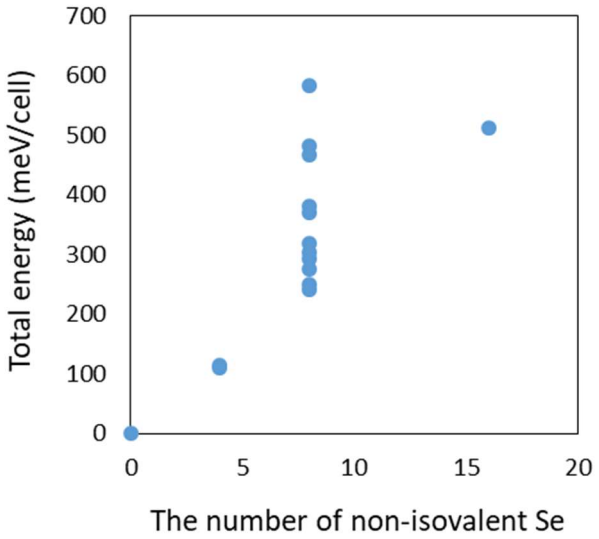

Table 6-4. The number of non-isovalent Se vs. the relative total energy trend obtained from the calculations on 1 × 2 × 2 supercells. The number of non-isovalent Se is defined as "the number of "non-isovalent-1 Se" + 2 × The number of "non-isovalent-2 Se".

Next, I prepared several structural models of bulk $(ZnSe)_x(CIGS)_{1-x}$ using 1 × 1 × 4 supercells (32 atoms), 2 × 2 × 2 supercells (64 atoms) and 2 × 2 × 4 supercells (128 atoms) to determine the ordering among Cu, In, and Ga atoms. For simplicity, the In/Ga ratio was fixed to 1. All structural models were shown in Figure 6-5, Figure 6-6, and Figure 6-7.

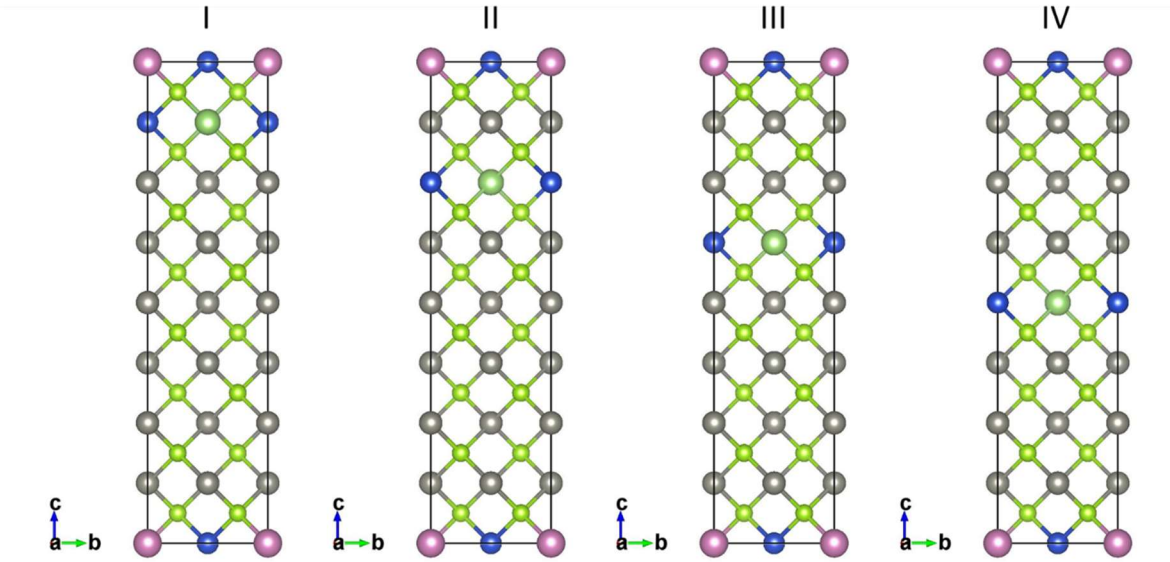

Figure 6-5. Structural models of the $(ZnSe)_x(CIGS)_{1-x}$, using 1 × 1 × 4 supercells. Gray, blue, pink, green, and light green are Zn, Cu, In, Ga, and Se atoms, respectively.

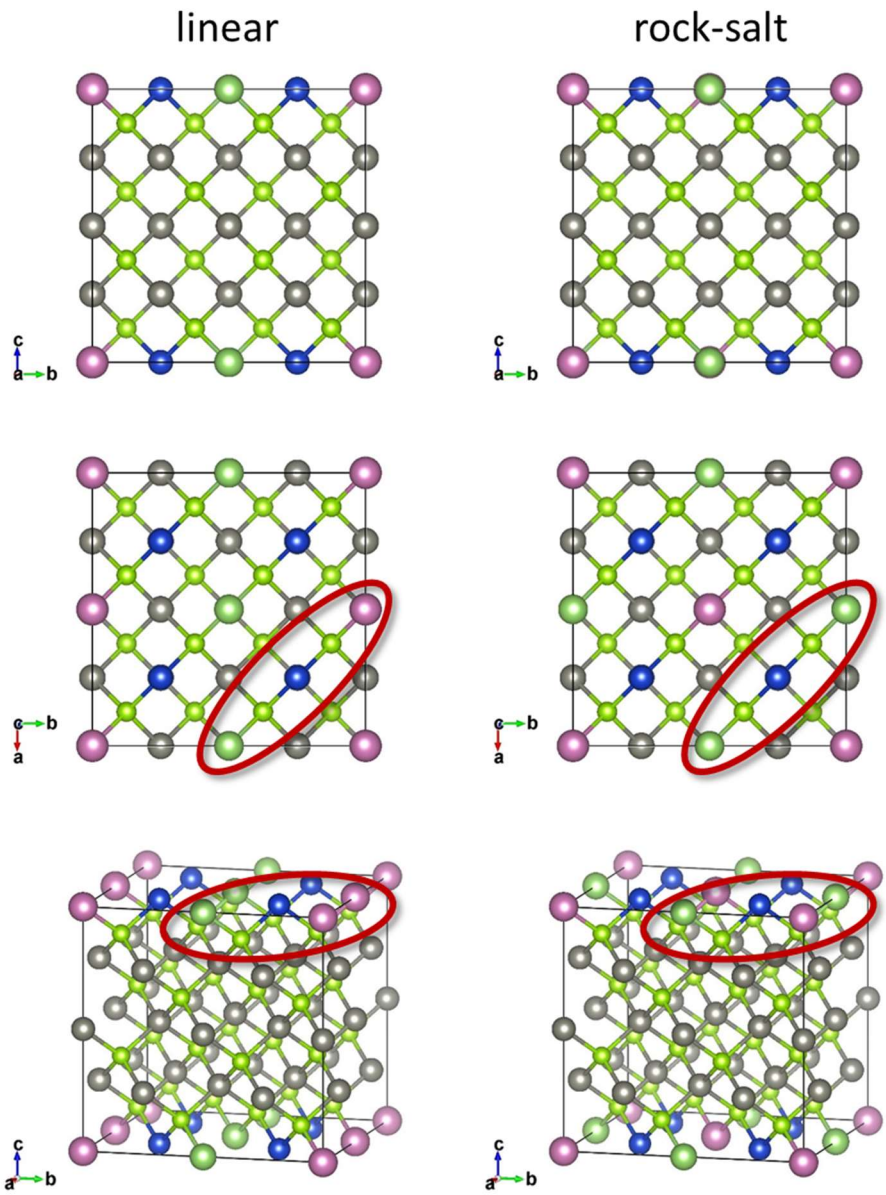

Figure 6-6. Structural models of the $(ZnSe)_x(CIGS)_{1-x}$, using 2 × 2 × 2 supercells viewed from three different angles. Gray, blue, pink, green, and light green are Zn, Cu, In, Ga, and Se atoms, respectively.

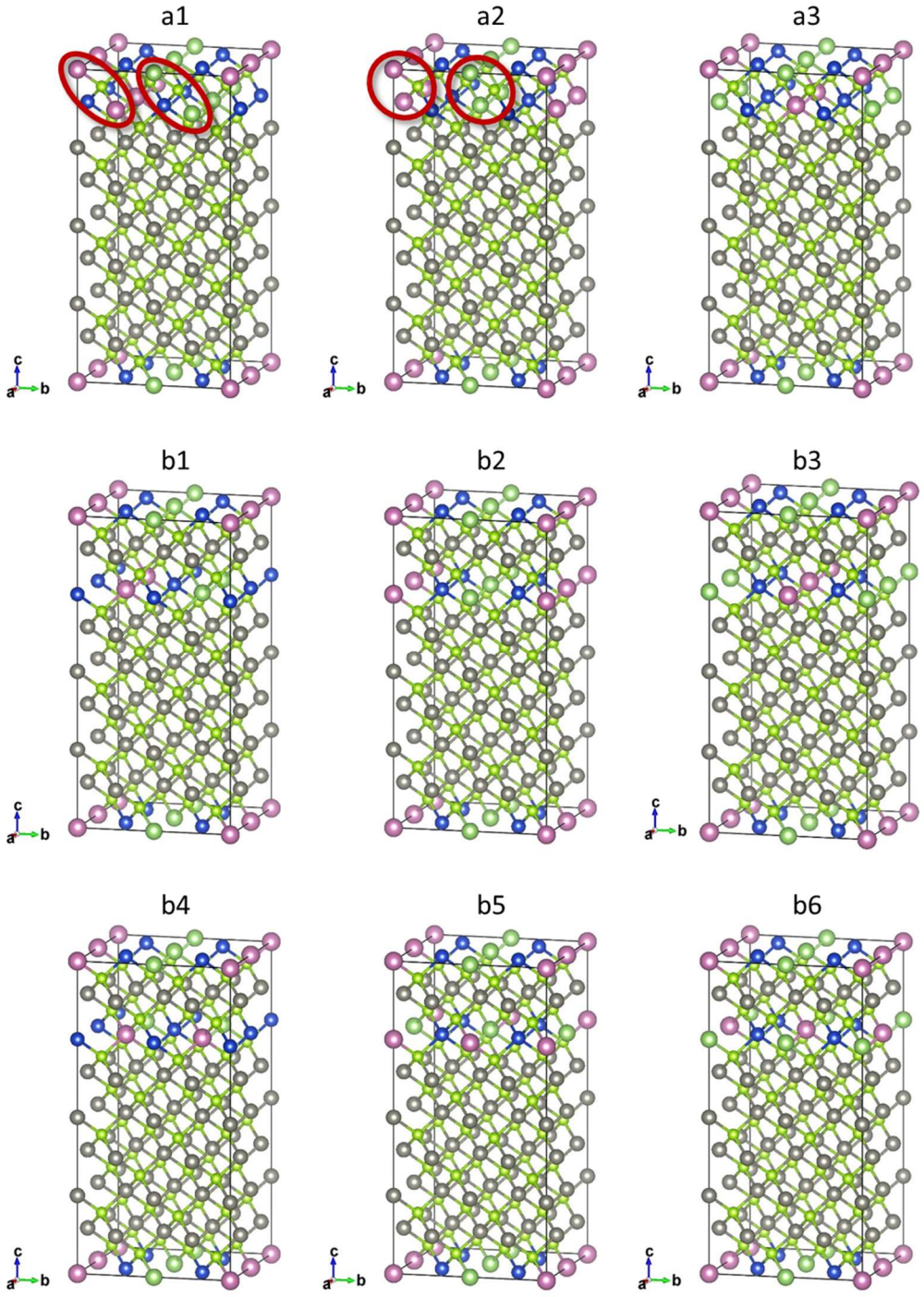

Figure 6-7. Structural models of the $(ZnSe)_x(CIGS)_{1-x}$, using 2 × 2 × 4 supercells. Gray, blue, pink, green, and light green are Zn, Cu, In, Ga, and Se atoms, respectively.

To these structural models, geometrically optimizations and energy calculations were also performed as the previous structural cells, and the obtained total energies are listed in Table 6-1. From these results, it was found that the cation orderings in $(ZnSe)_x(CIGS)_{1-x}$ have some tendencies as described below.

Table 6-1 The relative energies of each structural model with each relaxed structure.

supercell	model	total energy (meV/cell)
1 × 1 × 4	I	0.0
	II	21.1
	III	33.5
	IV	34.4
2 × 2 × 2	linear	0.2
	rock-salt	62.2
2 × 2 × 4	a1	37.4
	a2	104.6
	a3	0.0
	b1	114.0
	b2	178.7
	b3	184.1
	b4	110.0
	b5	180.4
	b6	182.6

First, from the results of the calculations on 1 × 1 × 4 supercells, it was confirmed that the cationic plane that consists of Cu, In, and Ga (hereafter, CIG plane) prefers to lie adjacent to each other than to be located separately. This is probably because the interface between ZnSe and CIGS is destabilized due to the mismatch in their lattice parameters. From such results, ZnSe and CIGS are presumed to be microscopically separated in the crystals of $(ZnSe)_x(CIGS)_{1-x}$, forming a kind of domains of each constituent compound.

Next, from the result of the calculations on 2 × 2 × 2 supercells, it was found that In and Ga prefer the linear arrangement rather than the rock-salt arrangement. Such trend is considered to be caused by the different bond length between In-Se (2.62 Å) and Ga-Se (2.47 Å), which originates from the difference between their ionic radii (In^{3+}: 81 pm, Ga^{3+}: 62 pm) [11]. As can be seen in the encircled part in Figure 6-6, each structural model has $[-M^{III}-$ Se-Cu-Se- M^{III}-Se-$]_n$ units. In the rock-salt model, these units are divided into two different ones, $[-In^{III}-$ Se-Cu-Se- In^{III}-Se-$]_n$ and $[-Ga^{III}-$ Se-Cu-Se-Ga^{III}-Se-$]_n$, and the bond length difference between In-Se and Ga-Se causes large distortions among these units. On the other hand, in the linear arrangement model, such distortions are not induced since In and Ga atoms are placed at 1:1 ratio in all $[-M^{III}-$ Se-Cu-Se- M^{III}-Se-$]_n$ units, and thus the structure becomes more stable than the other configuration.

Similar trends were also obtained from the results of the calculations on 2 × 2 × 4 supercells. Structural models a1-a3 in Figure 6-7, whose CIG planes are facing adjacently to each other, are more

stable than b1-b6, whose CIG planes are arranged separately. Among the former ones, a3 was revealed to be the most stable structure. This is probably because [-In-Se-] units and [-Ga-Se-] units are never arranged in adjacent to the same units in structure a3, while some of the units are combined to a single Se atom in a1 and a2 structure (as encircled in Figure 6-7.). Therefore, in the crystal of $(ZnSe)_x(CIGS)_{1-x}$, cations are presumed to be arranged like structure a3.

Finally, in accord with these discussions, the structural model of bulk $(ZnSe)_x(CIGS)_{1-x}$ was determined as depicted in Figure 6-8. Here, a 2 × 2× 6 supercell (192 atoms) with twelve cation layers was used so that the point defects inside the CIGS domains can be modeled by assigning them three layers.

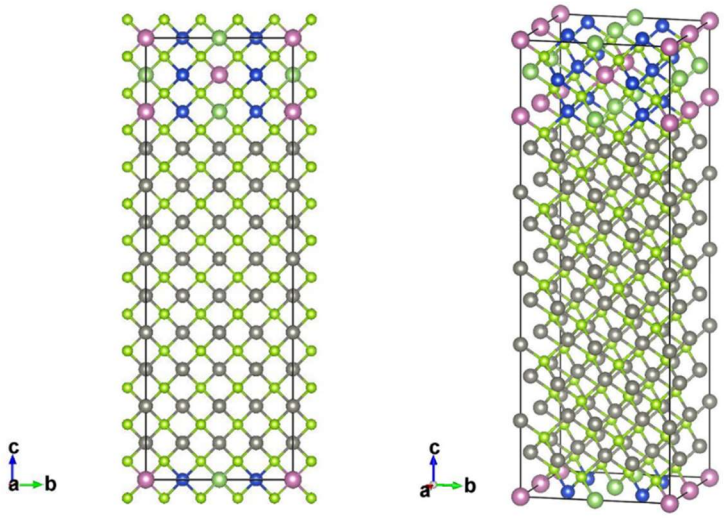

Figure 6-8. The structural model of the bulk of $(ZnSe)_x(CIGS)_{1-x}$, using a 2 × 2 × 6 supercell viewed from different angles. Gray, blue, pink, green, and light green are Zn, Cu, In, Ga, and Se atoms, respectively.

Subsequently, I prepared several defect structural models by using the this $(ZnSe)_x(CIGS)_{1-x}$ bulk model. I considered four types of vacancies (V_{Zn}, V_{Cu}, V_{In}, V_{Ga}), ten types of antisites (Cu_{Zn}, In_{Zn}, Ga_{Zn}, Zn_{Cu}, In_{Cu}, Ga_{Cu}, Zn_{In}, Cu_{In}, Zn_{Ga}, Cu_{Ga}), and one interstitial Se_{int} as defect models in $(ZnSe)_x(CIGS)_{1-x}$. The structural models of vacancies and anisites were prepared by removing or substituting an existing atom in the bulk model. On the other hand, the sites of the interstitials were determined according to a previous study on interstitials in Si [12], which has a quite similar crystal structure, and finally "tetragonal sites" and "split-(001) sites" were adopted for the structural models for Se_{int}. Here, the defects at the inner and at the edge of the domain where they originally belong (= ZnSe domain or CIGS domain) were distinguished, and the structural models of them were prepared individually. Additionally, the difference in the adjacent atoms around the defects were also considered. Here, since a bulk model has 96 anions and cations, the concentration of the defects was set to 1 % only considering the number of either cations or anions.

6-2-2. Calculations of defect formation energies

By using the defect structure models prepared in the previous section, the defect formation energy $E_f(D^q)$ defined by Eq (6.1) [13-16] was calculated. It should be noted that not only neutral but also charged structural models were calculated to estimate Eq (6.1) in order to take the donation and the acceptance of the electrons into account. Here, as the defect charges, the positive ones were considered for donors (which depicts the situations that the defect had donated the electrons) and the negative ones were considered for acceptors (which depicts the situations that the defect had accepted the electrons). All the energy terms in Eq (6.1) were calculated from the optimized structures.

$$E_f(D^q) = E(D^q) - E_p - \sum n_i \mu_i + q(\varepsilon_{VBM} + \varepsilon_F) \quad (6.1)$$

$E(D^q)$ is the total energy of the defect structural model with a charge q, E_p is a total energy of the bulk structural model, n_i is the number of reduced or added atoms of element i, μ_i is the chemical potential of element i, and ε_F is the Fermi energy which is referenced to VBM. Here, ε_F is considered as a variable, and thus $E_f(D^q)$ will be obtained as the function of the ε_F. The value μ_i was referenced to the total energy of each elemental substance, and was determined by using a kind of phase diagram as explained in the following paragraph.

First, the allowed range of the chemical potentials μ_i were determined by using the phase diagram shown in Figure 6-9. This diagram was depicted using the formation energies (Table 6-2) of the compounds that can be obtained as by-products in synthesizing $(ZnSe)_x(CIGS)_{1-x}$. The region in

the diagram marked with diagonal lines shows the allowed value range of μ_{Zn}, μ_{Cu}, μ_{Ga}, μ_{In}, and μ_{Se}, where point A, B(B'), and C correspond to the Cu-rich condition, In-rich (Ga-rich) condition, and Se-rich condition, respectively. All the crystal structures and coordinates of the compounds considered in the phase diagram were referenced from Inorganic Material Database (AtomWork) developed by National Institute for Materials Science [17,18].

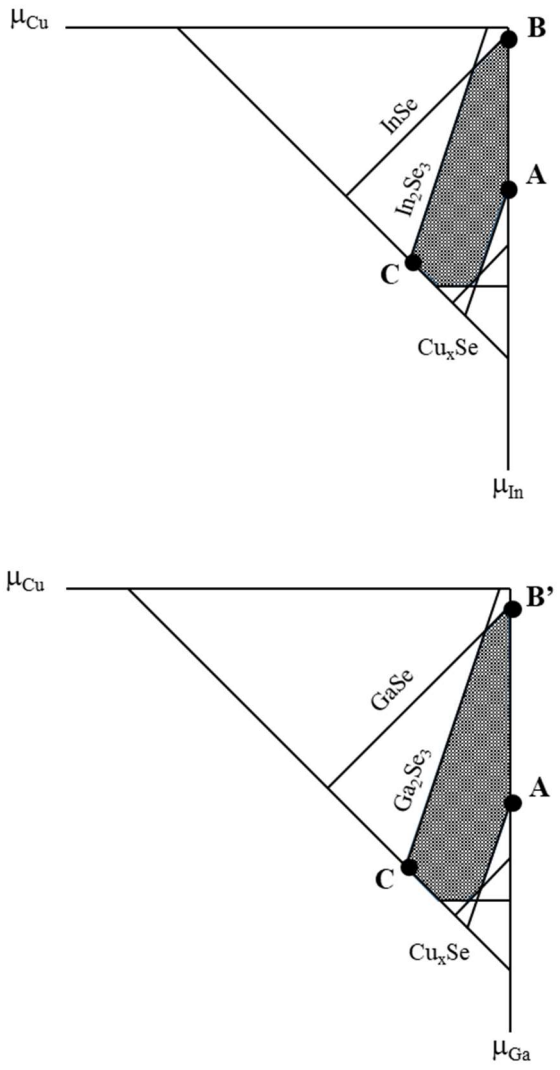

Figure 6-9. The value ranges of each chemical potential.

Table 6-2. The formation energies of $CuIn_{0.5}Ga_{0.5}Se$, ZnSe, and the compounds that can be obtained as by-products in synthesizing $(ZnSe)_x(CIGS)_{1-x}$.

compound	the number of atoms in a unit cell	total energy (eV/cell)	total energy (eV/FU)
$CuIn_{0.5}Ga_{0.5}Se$	16	-66.73	-33.36
ZnSe	8	-27.68	-6.92
Cu_2Se	12	-40.96	-10.24
Cu_3Se_2	10	-35.43	-17.72
Cu (metal)	4	-11.12	-2.78
CuSe	12	-43.58	-7.26
$CuSe_2$	6	-22.95	-11.48
Ga_2Se_3	20	-93.44	-23.36
Ga (metal)	8	-29.20	-3.65
GaSe	16	-72.84	-9.10
In_2Se_3	30	-128.35	-21.39
In (metal)	2	-5.91	-2.96
InSe	8	-32.81	-8.20
Se	3	-12.32	-4.11
Zn (metal)	2	-2.38	-1.19
$ZnSe_2$	12	-43.27	-10.82
$ZnGa_2Se_4$	14	-60.94	-30.47

Next, the chemical potential of each element in the vapor deposition beam under the synthesize condition of $(ZnSe)_x(CIGS)_{1-x}$ was estimated according to the following equations,

$$\mu_{\mathrm{i}}(\mathrm{T}) = \mu_{\mathrm{i}}^{\mathrm{o}}(T) + RTln\frac{p_{\mathrm{i}}}{p^{\mathrm{o}}} \tag{6.2}$$

$$\mu_{\mathrm{i}}^{\mathrm{o}}(T) = \Delta_{\mathrm{f}}G_{\mathrm{i}}^{\mathrm{o}} - TS^{\mathrm{o}} \tag{6.3}$$

where $\Delta_{\mathrm{f}}G_{\mathrm{i}}^{\mathrm{o}}$ is the standard molar Gibbs energy of element i, p^{o} is the standard pressure, p_{i} is the

partial pressure of element i, and T is the temperature. The values of $\Delta_f G_i^o$ were referenced from the literature [19], and p_i were obtained as the estimated values from their deposition rates [2]. Thus, the chemical potentials of the element were estimated as ((μ_{Cu}, μ_{In}, μ_{Ga}, μ_{Zn}, μ_{Se}) = (1.1, 0.1, 0.3, -0.9, 0.0)). Here, since μ_{Cu} has the largest value (+1.1 eV) and μ_{Zn} has the smallest value (-0.9 eV), the chemical potential of each elements in this material corresponds to point A in Figure 6-9. Therefore, the chemical potentials at point A ((μ_{Cu}, μ_{In}, μ_{Ga}, μ_{Zn}, μ_{Se}) = (0.0, -1.1, -1.4, -1.0, -0.6)) will used to calculate the defect formation energies in the following sections.

By the way, the defect structural model used in the calculation of Eq (6.1) consists of a supercell where an atom or an electron was removed or added from a bulk one. Therefore, the calculated shapes and occupancies of its bands are generally different from those of the bulk. Furthermore, the energies of its bands will also be shifted due to the potential shift associated with the changes of the number of atoms and electrons. Thus, the band energies and the total energies obtained from the defect structural model were corrected as follows.

First, the band energy at VBM was corrected according to Eq (6.4), where the correcting term was introduced as the difference between the potential of the bulk model (V_{bulk}) and that in the bulk-like region of the defect model (V_{defect}). Thus, the VBM energy was obtained using these potentials and the VBM energy of the bulk model ($\varepsilon_{VBM,bulk}$) [13].

$$\varepsilon_{VBM} = \varepsilon_{VBM,bulk} + (V_{defect} - V_{bulk}) \quad (6.4)$$

Here, V_{defect} was obtained by integrating the local potentials in the defect model at the positions where the distance from the defect is at least 5Å.

Next, the total energy of a defect structural model was corrected according to Eq (6.5), where the correcting term comes from the consideration that the energy of the excess charge will be overestimated (or under estimated) due to the potential shift in a defect supercell. Thus, the corrected energy ($E_{\mathrm{corrected}}(D^q)$) was obtained by adding the unphysical shift to the original total energy ($E(D^q)$) of the defect supercell [13].

$$E_{\mathrm{corrected}}(D^q) = E(D^q) + q(V_{\mathrm{defect}} - V_{\mathrm{bulk}}) \quad (6.5)$$

6-2-3. Calculation Conditions

All the calculations were performed by means of density functional theory (DFT) implemented in VASP (The Vienna Ab initio Simulation Package) [20-23] with the projector augmented wave (PAW) method [24,25] and the localized density approximation (LDA) exchange-correlation functional [26, 27]. For Cu, In, Ga, and Zn, s and p electrons in the outermost shell and d electrons just below these electrons were treated as valence states. For Se, 4s and 4p electrons were treated as valence states. The *k*-point sampling of the Brillouin zone was set to 2 × 2 × 1 (Gamma-centered sampling) and a 400 eV cutoff energy was used. In addition, in order to describe the d-electrons nearby the defects more precisely, onsite Coulomb potentials [28-31] were added to Zn (U = 7.0 eV), Cu (U = 6.0 eV), In (U = 7.0 eV) and Ga (U = 9.0 eV), so that the positions of their d-band peaks in the valence bands will reproduce the experimental data as shown in Figure 6-10 [32,33]. The structures were optimized until the forces on all atoms were smaller than 0.05 eV/Å and the total energies were calculated until they converged within 10^{-4} eV. The lattice parameters of all the defect structure models were fixed to that of the optimized bulk model.

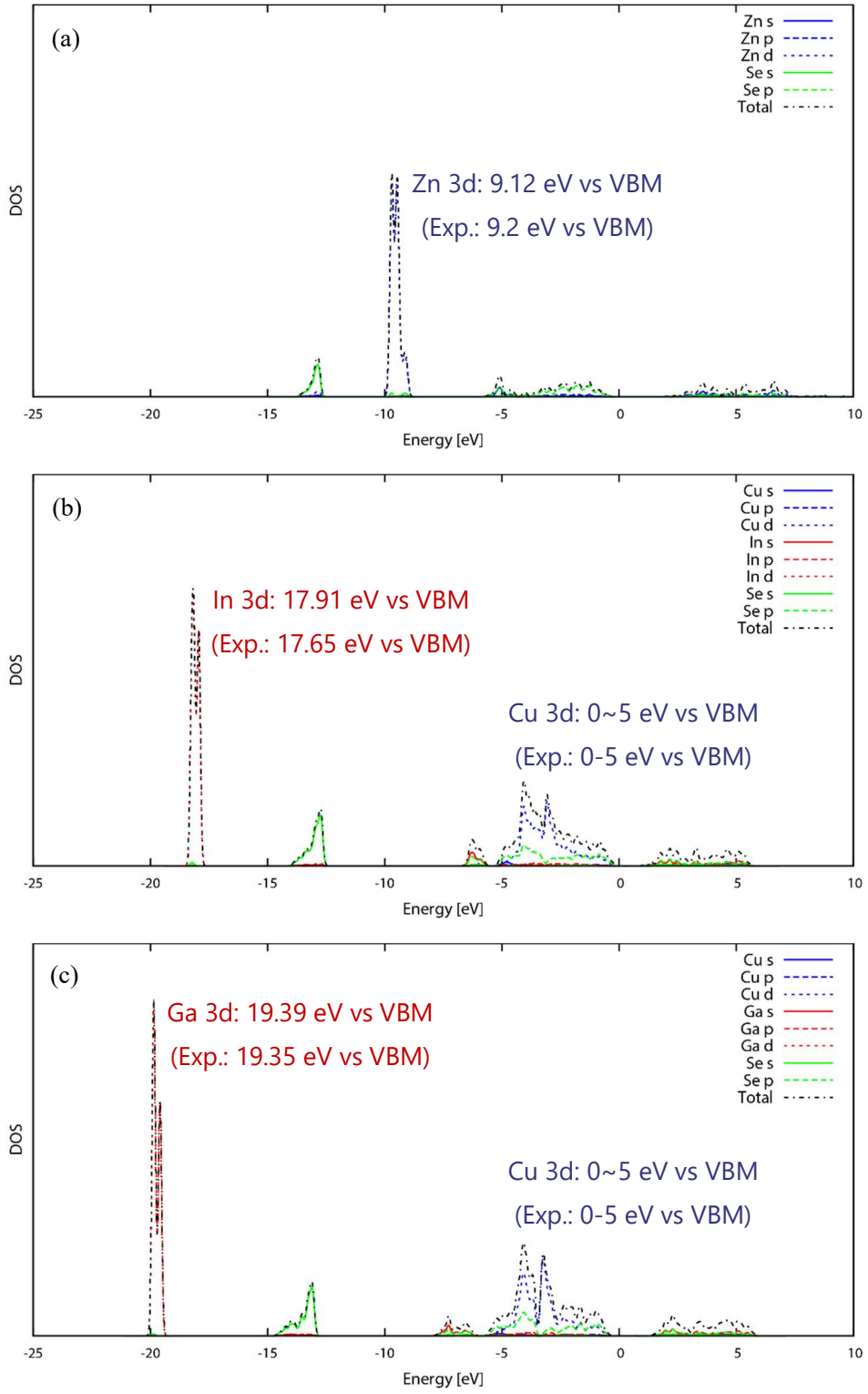

Figure 6-10. Calculated DOS of (a) ZnSe, (b) $CuInSe_2$, and (c) $CuGaSe_2$ with U parameters. The energy of VBM position was set to zero.

6-3. Comparison of the formation energy of each defect

6-3-1. Site dependence

First, the fomation energies of the defects at different sites will be compared. The caclculated formation energies of vacancies (V_{Zn}, V_{Cu}, V_{In}, V_{Ga}), antisites (Cu_{Zn}, In_{Zn}, Ga_{Zn}, Zn_{Cu}, In_{Cu}, Ga_{Cu}, Zn_{In}, Cu_{In}, Zn_{Ga}、 Cu_{Ga}), and interstitials (Se_{int}) were plotted as the functions of Fermi energy in Figure 6-11, 6-12, and 6-13, respectively.

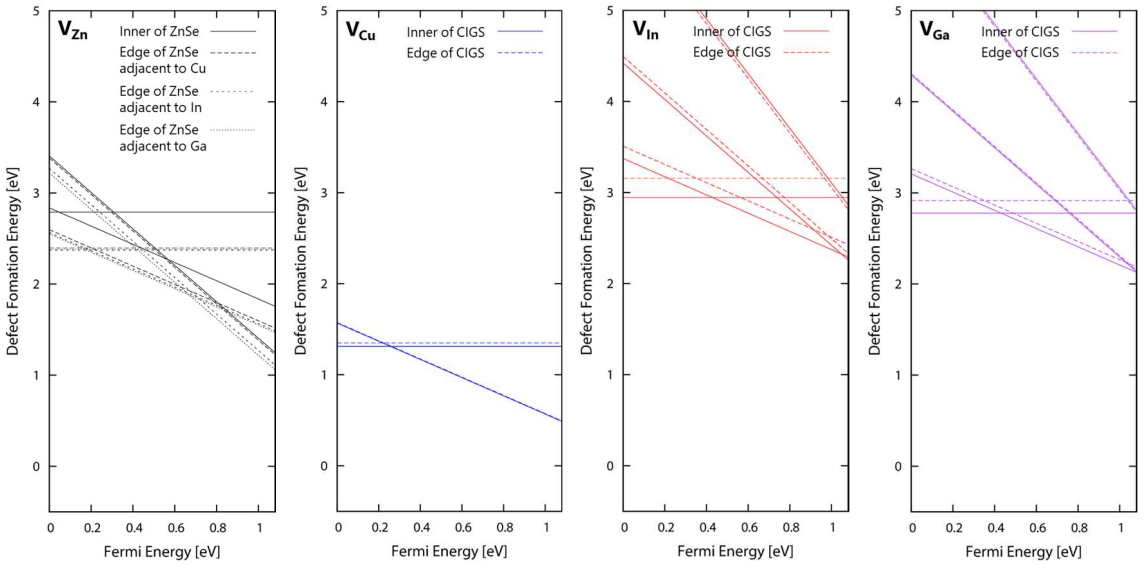

Figure 6-11. The fomation energies of vacancies (V_{Zn}, V_{Cu}, V_{In}, V_{Ga}) at each site.

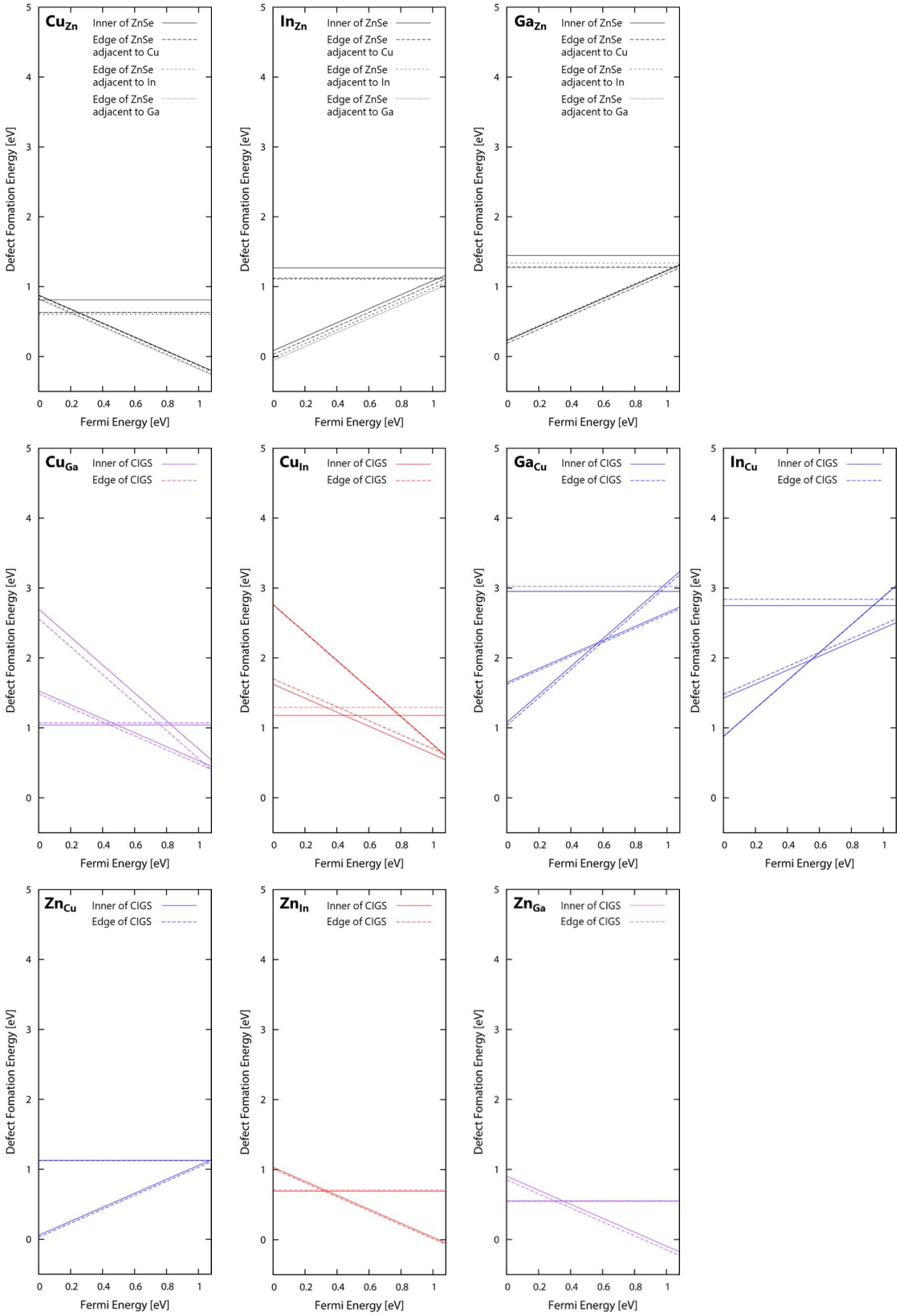

Figure 6-12. The fomation energies of antisites at each site.

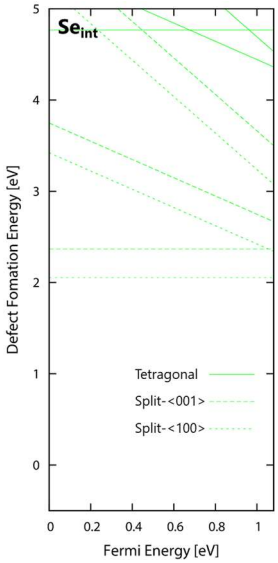

Figure 6-13. The fomation energies of interstitials (Se_{int}).

Comparing the formation energies among V_{Zn} vacancies (Figure 6-11), it was confirmed that they will be more easily created near the boundary region with the CIGS domains than inside the ZnSe domains. On the other hand, Figure 6-11 also shows that V_{Cu}, V_{In}, and V_{Ga} prefer to be created inside the CIGS domains rather than near the boundary with the ZnSe domains. From these results, it is indicated that the CIGS domains are more susceptible to creation of cation vacancies than the ZnSe domains in $(ZnSe)_x(CIGS)_{1-x}$ solid solutions.

A similar trend was also observed in the site dependence of the antisite formation energies. From the comparison between Cu_{Zn}, In_{Zn}, and Ga_{Zn} in Figure 6-12, one can find that Zn cations near the boundary region with the CIGS domains are more easily substituted by the other cations than those inside the ZnSe domains. Besides, Cu_{In}, Cu_{Ga}, Ga_{Cu}, and In_{Cu}, which are the internal antisites in CIGS

domains, also prefer to be formed inside the CIGS domains rather than near the boundary with the ZnSe domain as can be seen in Figure 6-12. However, for Zn_{Cu}, Zn_{In}, and Zn_{Ga}, the group of antisites where Zn cations substituted the other cations in the CIGS domains, the site dependence of the defect formation energies was hardly observed, indicating that these antisites are likely to be created to a similar extent at each cation site in the CIGS domain.

The site dependence of Se_{int} was found to be very large from Figure 6-13. The variation of the defect formation energies at different sites was up to 2 eV, which was quite larger than that of vacancies and antisites. This is probably because the distance between a point defect and its nearest neighbor atom is smaller for Se_{int}, and thus the size and the charge of the adjacent atom will strongly influence on the stability of the defect atom. Nevertheless, since the formation energies of any Se_{int} are much larger than those of the other types of defects, there should exist only a little amount of Se_{int} in the crystals of $(ZnSe)_x(CIGS)_{1-x}$.

6-3-2. Dominant defect in ZnSe/CIGS

Next, I will compare the formation energies among different defect species in order to indentify the dominant ones in the crystals of $(ZnSe)_x(CIGS)_{1-x}$. The formation energy of each defect at the most stable site is plotted in Figure 6-14. According to this plot, it was found that the formation energies of six antisites, Cu_{Zn}, In_{Zn}, Ga_{Zn}, Zn_{Cu}, Zn_{In}, Zn_{Ga} are especially small as can be seen in Figure 6-14 (middle). It should be noted that none of these antisites can be created in ZnSe nor CIGS itself, but can only be created in their solid solution. Besides, since the formation energies of these antisites are much smaller than that of V_{Cu} (Figure 6-14 (left)), which is a well-known acceptor that gives the p-type characteristics to CIGS, they are presumed to be the dominant defects in $(ZnSe)_x(CIGS)_{1-x}$ crystal which can be easily created.

Among these defects, In_{Zn}, Ga_{Zn}, and Zn_{Cu} work as donors and Cu_{Zn}, Zn_{In}, and Zn_{Ga} work as acceptors, and one can find that the straight lines that correspond to the formation energies of these defects intersect at the energy position of 0.4 eV above VBM as pointed with an arrow in Figure 6-14 (middle). This indicates that the position of its Fermi energy ε_F will be pinned nearby the intersection, since more donor will be created in the energy region of $\varepsilon_F < 0.4$ eV and more acceptors will be created in the energy region of $\varepsilon_F > 0.4$ eV, both of which cancelling the variation of the Fermi energy. In this material, the position of the intersection is closer to VBM than CBM, and thus $(ZnSe)_x(CIGS)_{1-x}$ is thought to be a p-type semiconductor. Such result supports the experimental fact that

$(ZnSe)_x(CIGS)_{1-x}$ has a p-type characteristics though ZnSe itself, which dominates the most part of this material, is essentially an n-type semiconductor.

At the end, it should be noted that the difference between the formation energies of these dominant defects and the other ones are more than 0.5 eV around the Fermi energy of 0.4 eV. Such difference in the formation energy corresponds to a 3000-fold difference in the carrier concentration according to Eq (6.8) mentioned later. Therefore, the defects other than the dominant ones can be neglected in the following discussion.

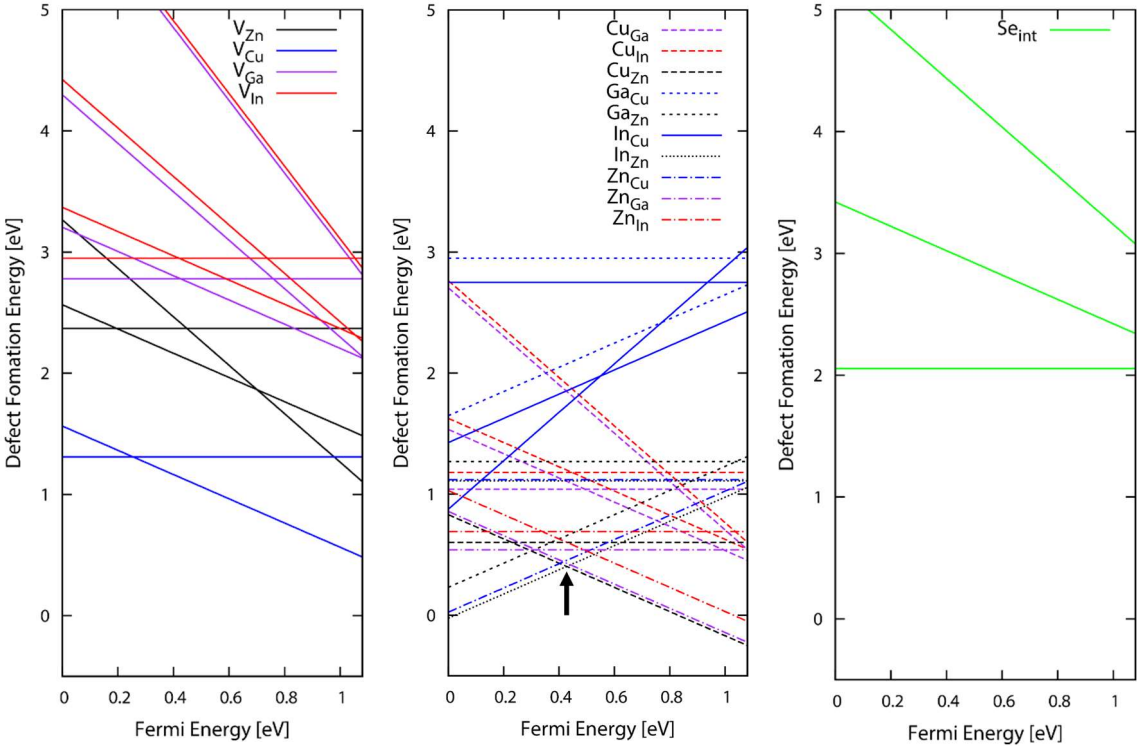

Figure 6-14. The formation energies of each defect at its most stable site. Left: vacancies, middle: antisites, and right: Se interstitial.

6-4. Dependence on external conditions

6-4-1. Thermal dependence

Now discuss the temperature dependence of the defect formation energy will be discussed. Since in Eq (6.1) only the term μ_i will be varied with temperature, the temperature dependence of the chemical potentials was investigated here. The calculated chemical potentials of elements in the vapor deposition beam at each temperature (350~650 ℃) are listed in Table 6-5, and one can find that for all the chemical elements their chemical potentials decrease by 0.3 ~ 0.4 eV with increasing temperature by 100 ℃. Therefore, according to Eq (6.1), the formation energies of vacancies will be decreased under the high-temperature conditions, while those of interstitials will be increased under the same conditions. Such consideration matches with the experimentally observed tendencies where the efficiency of pure CIGS, whose dominant defects are V_{Cu} vacancies [5], increases with the temperature in the region below 600 ℃ [34-36]. On the other hand, the formation energies of antisites will hardly change with the temperature variation, since the changes in the chemical potentials of the added element and the removed one will be counterbalanced. Thus, the thermal dependence of the photocurrents is expected to be small in $(ZnSe)_x(CIGS)_{1-x}$, since their dominant defects are antisites.

Now, there are some cases where the chemical potentials of the elements in the vapor deposition beam become too low to shape crystals above a certain temperature. For instance, at the temperature above 550 ℃, the sum of μ_{Zn} and μ_{Se} becomes lower than the formation enthalpy of

ZnSe (-1.62 eV), indicating that the ZnSe crystals cannot be created thermodynamically in this temperature region. On the other hand, the value of $2\mu_{Cu} + \mu_{In} + \mu_{Ga} + 4\mu_{Se}$ is always larger than the formation enthalpy of $Cu_2InGaSe_4$ (-4.77 eV) among all temperature region considered here. Thus, in was confirmed that CIGS can be crystalized under the high-temperature region above 550 ℃. From these results, it is expected that the crystallinity of $(ZnSe)_x(CIGS)_{1-x}$ will be lower than that of pure CIGS in the temperature region above 550 ℃, and thus its photocurrent will also be decreased in such high-temperature region.

Table 6-5. The calculated chemical potentials of the vapor deposition beam at each temperature.

	μ_{Cu}	μ_{In}	μ_{Ga}	μ_{Zn}	μ_{Se}
350 ℃	1.4	0.5	0.7	-0.6	0.3
450 ℃	1.1	0.1	0.3	-0.9	0.0
550 ℃	0.7	-0.2	0.0	-1.3	-0.4
650 ℃	0.4	-0.6	-0.4	-1.6	-0.7

6-4-2. Pressure dependence

Subsequently, the dependence of the defect properties on partial pressures will be discussed. Since the variations of the partial pressures will also be reflected in the chemical potentials, according to Eq (6.2), only the effects of the change in the chemical potentials of certain elements on the defect formation energies will be discussed here. Besides, since a 0.1 eV change of the defect formation energy corresponds to a five-fold difference in the partial pressure, I just changed the partial pressure within ± 0.1 eV. Hereafter, only the effect of the variation in Cu and Zn, which are the dominant cations in the solid solution, will be considered.

First, the defect formation energies with different μ_{Cu} were shown in Figure 6-15. For simplicity, only the formation energies of six dominant defects (Cu_{Zn}, In_{Zn}, Ga_{Zn}, Zn_{Cu}, Zn_{In}, Zn_{Ga}) mentioned above were plotted. From Figure 6-15, one can find that as μ_{Cu} increases (= as p_{Cu} increases) the intersection between the straight lines which correspond to the formation energies of the donors and the acceptors gets much closer to VBM. This is probably because the Cu_{Zn}, one of the dominant acceptors, becomes more easily to be created with increasing μ_{Cu}, while Zn_{Cu}, one of the dominant donors, gets less easily to be created in the same situation. On the other hand, the formation energies of the other dominant acceptors (Zn_{Ga}, Zn_{In}) and donors (In_{Zn}, Ga_{Zn}) remains almost unchanged. Therefore, it was indicated that the p-type characteristics of $(ZnSe)_x(CIGS)_{1-x}$ will be increased with increasing p_{Cu}.

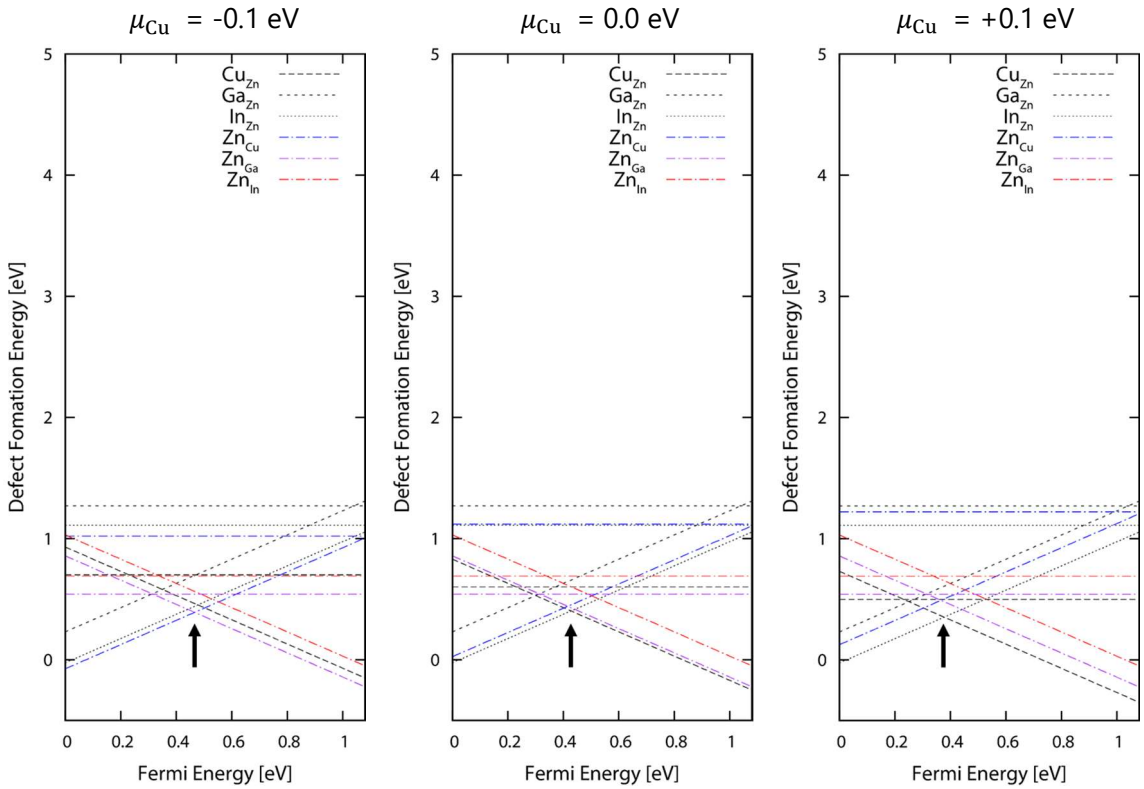

Figure 6-15. The defect formation energies with different μ_{Cu}.

In order to confirm such consideration, I subsequently estimated the variations of Fermi energy ε_F and the carrier concentration C_p in $(ZnSe)_x(CIGS)_{1-x}$ with increasing μ_{Cu}. Fermi energy ε_F and the carrier concentration C_p were calculated using the following equations [14],

$$\sum_{X,\,q}[D^q] - n + p = 0 \ \text{(electroneutrality condition)} \tag{6.6}$$

$$C_p = -n + p \tag{6.7}$$

where $[D^q]$, n, and p are the concentrations of charged defect D^q, electron, and hole, respectively. Each of them are related to Fermi energy ε_F by the following formulas,

$$[D^q] = N_0 \exp\left(-\frac{E_f(D^q)}{k_B T}\right) \tag{6.8}$$

$$n = \left(-\frac{m_e^* k_B T}{2\pi\hbar^2}\right)^{\frac{3}{2}} \exp\left(-\frac{\varepsilon_{CBM} - \varepsilon_F}{k_B T}\right) \tag{6.9}$$

$$p = \left(-\frac{m_h^* k_B T}{2\pi\hbar^2}\right)^{\frac{3}{2}} \exp\left(-\frac{\varepsilon_F}{k_B T}\right) \tag{6.10}$$

where N_0 is the number of the sites where the defect can be incorporated, k_B is Boltzmann's constant, and m_e^* and m_h^* is the effective mass of electrons and holes, respectively. Here, m_e^* and m_h^* was set to 0.21 and 0.60, respectively, which are the carrier effective masses of ZnSe [37]. It should be noted that only the effective masses of ZnSe were considered, since the most part of $(ZnSe)_x(CIGS)_{1-x}$ is dominated by ZnSe and the effective masses of CIGS (m_e^*: 0.09, m_h^*: 0.73 [38]) are also similar to those of ZnSe.

The calculated ε_F and C_p was listed in Table 6-6. The value of C_p ranged between 10^{15} to 10^{17} cm^{-3}, which is consistent with the experimental values reported for conventional p-type semiconductors [36,39-41]. As μ_{Cu} increases, ε_F gets lower and C_p gets larger. Therefore, these results also strongly support that the p-type characteristics of $(ZnSe)_x(CIGS)_{1-x}$ will be improved with increasing p_{Cu}.

Table 6-6. The calculated ε_F and C_p with different μ_{Cu}.

μ_{Cu}	-0.1	0.0	+0.1
ε_F (eV)	0.46	0.42	0.38
C_p (cm^{-3})	1.49×10^{15}	2.75×10^{16}	5.61×10^{16}

Next, the defect formation energies with different μ_{Zn} were shown in Figure 6-16. In contrast to the case for μ_{Cu}, the intersection between the lines of donors' and acceptors' formation energies was nearly unchanged with increasing μ_{Zn} (=increasing p_{Zn}). This is probably because the changes in the formation energies of the dominant donors (In_{Zn}, Ga_{Zn}, Zn_{Cu}) and the dominant acceptors (Cu_{Zn}, Zn_{In}, Zn_{Ga}) with increasing μ_{Zn} were cancelled out. Therefore, it is expected that the p-type characteristics of $(ZnSe)_x(CIGS)_{1-x}$ will hardly change with increasing p_{Zn}. The variations of ε_F and C_p with increasing μ_{Zn} also showed the same trend (Table 6-7).

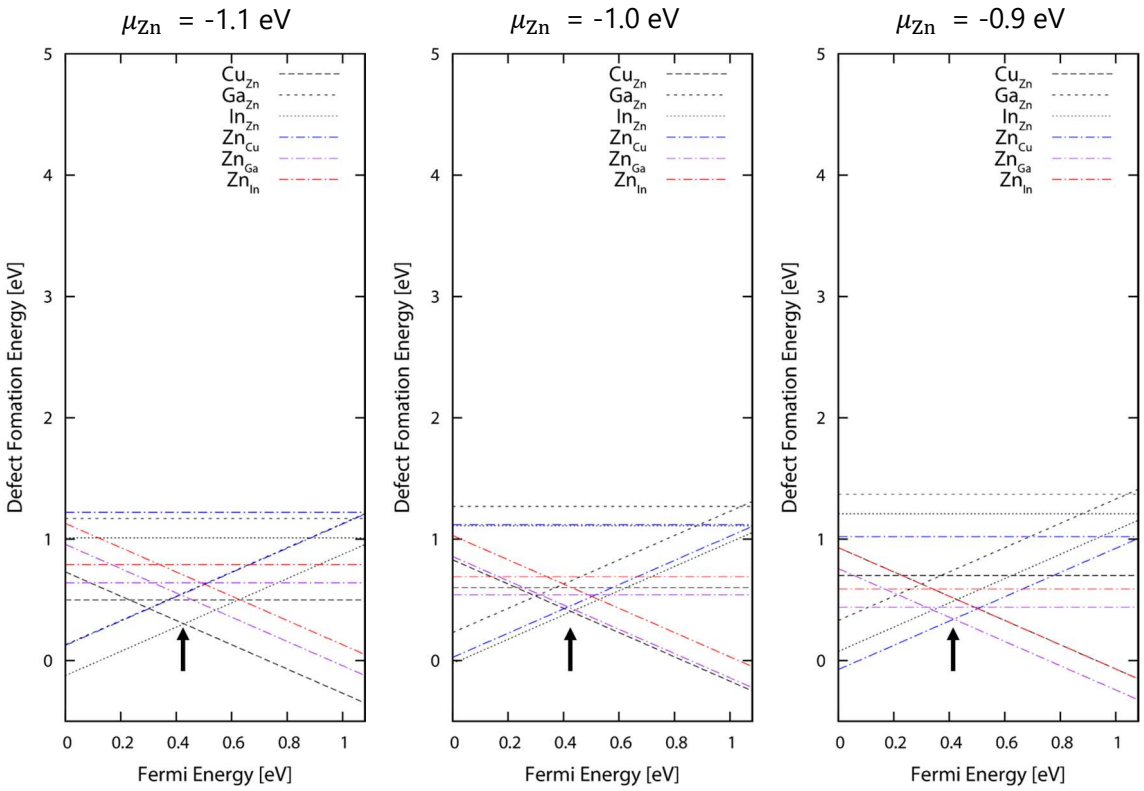

Figure 6-16. The defect formation energies with different μ_{Zn}.

Table 6-7. The variations of ε_F and C_p with increasing μ_{Zn}.

μ_{Zu}	-1.1	-1.0	-0.9
ε_F (eV)	0.43	0.42	0.40
C_p (cm^{-3})	2.34×10^{16}	2.75×10^{16}	4.15×10^{16}

From these results, it is strongly indicated that $(ZnSe)_x(CIGS)_{1-x}$ should be synthesized under Cu-rich conditions in order to improve their p-type characteristics. Indeed, similar trends have also been observed in some experiments, where $(ZnSe)_x(CIGS)_{1-x}$ had shown n-type characteristic under Cu-poor condition as previously mentioned, and where the photocurrent of $(ZnSe)_x(CIGS)_{1-x}$ had improved with the increase of the relative deposition rate of Cu ($J_{Cu}/J_{In}+J_{Ga}$, where J_i gives the deposition rate of element i.) [5]. All these previous reports indicate that the guideline obtained in this research is of high validity.

Bibliography

[1] Kumagai, H.; Minegishi, T.; Sato, N.; Yamada, T.; Kubota, J.; Domen K. Efficient Solar Hydrogen Production from Neutral Electrolytes Using Surface-Modified $Cu(In,Ga)Se_2$ Photocahodes. *J. Mater. Chem. A,* **2015**, *3*, 8300.

[2] Kaneko, H.; Minegishi, T.; Nakabayashi, M.; Shibata, N.; Kuang, Y.; Yamada, T.; Domen K. A Novel Photocathode Material for Sunlight-Driven Overall Water Splitting: Solid Solution of ZnSe and $Cu(In,Ga)Se_2$. *Adv. Func. Mater.*, **2016**, *26*, 4570.

[3] Kaneko, H.; Minegishi, T.; Nakabayashi, M.; Shibata, N.; Domen K. Enhanced Hydrogen Evolution under Simulated Sunlight from Neutral Electrolytes on $(ZnSe)_{0.85}(CuIn_{0.7}Ga_{0.3}Se_2)_{0.15}$ Photocathodes Prepared by a Bilayer Method. *Angew. Chem. Int. Ed.*, **2016**, *55*, 15329.

[4] Goto, Y.; Minegishi, T.; Kageshima, Y.; Higashi, T.; Kaneko, H.; Kuang, Y.; Nakabayashi, M.; Shibata, N.; Ishihara, H.; Hayashi, T.; Kudo, A.; Yamada, T.; K. Domen. A particulate $(ZnSe)_{0.85}(CuIn_{0.7}Ga_{0.3}Se_2)_{0.15}$ photocathode modified with CdS and ZnS for sunlight-driven overall water splitting. *J. Mater. Chem. A* **2017**, *5*, 21242.

[5] Zhao, Y. J.; Persson, C.; Lany, S.; Zunger, A. Why can $CuInSe_2$ be readily equilibrium-doped n-type but the wider-gap $CuGaSe_2$ cannot? *Appl. Phys. Lett.* **2004**, *85*, 5860.

[6] Kaneko, H.; Minegishi, T.; Domen, K. Effects of Zn- and Cu-related defects in $(ZnSe)_x(CuIn_{0.7}Ga_{0.3}Se_2)_{1-x}$ thin film photocathodes on the photoelectrochemical properties for

hydrogen production. “Defects in semiconductors” Gordon Research Conference, Colby-Sawyer College, New London, USA (2016).

[7] Andreev, A. A.; Bulanyi, M. F.; Golikov, S. A.; Mozharovsikii, L. A. Synthesis and some properties of single crystals of $Zn_xCd_{1-x}S$ and ZnS_ySe_{1-y} solid solutions. *Russ. J. Inorg. Chem.* **1995**, *40*, 1039.

[8] Wang, L. G.; Zunger, A. Dilute nonisovalent (II-VI)-(III-V) semiconductor alloys: Monodoping, codoping, and cluster doping in ZnSe-GaAs. *Phys. Rev. B* **2003**, *68*, 125211.

[9] Glicksman, M.; Kraeft, W. D. Effect of high intrinsic ion concentrations on electron energies in solid solutions of III–V and II–VI semiconductors. *Solid. State. Electron.* **1985**, *28*, 151.

[10] Chen, S.; Gong, X. G.; Walsh, A.; Wei, S.-H. Electronic structure and stability of quaternary chalcogenide semiconductors derived from cation cross-substitution of II-VI and I-III-VI_2 compounds. *Phys. Rev. B* **2009**, *79*, 165211.

[11] Contreras, M. A.; Egaas, B.; Dippo, P.; Webb, J.; Granata, J.; Ramanathan, K.; Asher, S.; Swartzlander, A.; Noufi, R. On the role of Na and modifications to $Cu(In,Ga)Se_2$ absorber materials using thin-MF (M=Na, K, Cs) precursor layers. *Conference Record of the Twenty Sixth IEEE Photovoltaic Specialist Conference* (1997) 359.

[12] Nishimatsu, T.; Sluiter, M.; Mizuseki, H.; Kawazoe, Y.; Sato, Y.; Miyata, M.; Uehara M. Prediction of XPS spectra of silicon self-interstitials with the all-electron mixed-basis method. *Physica B* **2003**, *340–342*, 570.

[13] Persson, C.; Zhao, Y.-J.; Lany, S.; Zunger, A. n-type doping of $CuInSe_2$ and $CuGaSe_2$. *Phys. Rev. B* **2005**, *2*, 035211.

[14] Freysoldt, C.; Grabowski, B.; Hickel, T.; Neugebauer, J.; Kresse, G.; Van de Walle, C. G. First-principles calculations for point defects in solids. *Rev. Mod. Phys.,* **2014**, *86*, 253.

[15] Zhang, S. B.; Northrup J. E. Chemical potential dependence of defect formation energies in GaAs: Application to Ga self-diffusion. *Phys. Rev. Lett*. **1991**, *67*, 2339.

[16] Van de Walle, C. G.; Laks, D. B.; Neumark, G. F.; Pantelides, S. T. First-principles calculations of solubilities and doping limits: Li, Na, and N in ZnSe. *Phys. Rev. B* **1993**, *47*, 9425.

[17] Xu, Y.; Yamazaki, M.; Villars, P. Inorganic Materials Database for Exploring the Nature of Material. *Jpn. J. Appl. Phys.* **2011**, *50*, 11RH02.

[18] National Institute for Materials Science (NIMS) AtomWork <http://crystdb.nims.go.jp/>

[19] David R. Lide, ed., CRC Handbook of Chemistry and Physics, Internet Version 2005, <http://www.hbcpnetbase.com>, CRC Press, Boca Raton, FL, 2005.

[20] Kresse, G.; Hafner, J. Ab. initio molecular dynamics for liquid metals. *Phys. Rev. B: Condens. Matter Mater. Phys*. **1993**, *47*, 558.

[21] Kresse, G.; Hafner, J. Ab initio molecular-dynamics simulation of the liquid-metal−amorphous-semiconductor transition in germanium. *Phys. Rev. B: Condens. Matter Mater. Phys.* **1994**, *49*, 14251.

[22] Kresse, G.; Furthmüller, J. Efficiency of ab-initio total energy calculations for metals and

semiconductors using a plane-wave basis set. *Comput. Mater. Sci.* **1996**, *6*, 15.

[23] Kresse, G.; Furthmüller, J. Efficient iterative schemes for ab initio total-energy calculations using a plane-wave basis set. *Phys. Rev. B: Condens. Matter Mater. Phys.* **1996**, *54*, 11169.

[24] Blochl, P. E. Projector augmented-wave method. *Phys. Rev. B,* **1994**, *50*, 17953.

[25] Kresse, G.; Joubert, D. From ultrasoft pseudopotentials to the projector augmented-wave method. *Phys. Rev. B*, **1999**, *59*, 1758.

[26] Perdew, J. P.; Zunger, A. Self-interaction correction to density-functional approximations for many-electron systems. *Phys. Rev. B*, **1981**, *23*, 5048.

[27] Ceperley, D. M.; Alder, B. I. Ground State of the Electron Gas by a Stochastic Method. *Phys. Rev. Lett.* **1980**, *45*, 566.

[28] Anisimov, V. I.; Zaanen, J.; Andersen, O. K. Band theory and Mott insulators: Hubbard U instead of Stoner I. *Phys. Rev. B* **1991**, *44*, 943.

[29] Anisimov, V. I.; Korotin, M. A.; Zaanen, J.; Andersen, O. K. Spin bags, polarons, and impurity potentials in $La_{2-x}Sr_xCuO_4$ from first principle. *Phys. Rev. Lett.* **1992**, *68*, 345.

[30] Liechtenstein, A. I.; Anisimov, V. I.; Zaanen, J. Density-functional theory and strong interactions: Orbital ordering in Mott-Hubbard insulators. *Phys. Rev. B* **1995**, *52*, R5467.

[31] Dudarev, S. L.; Botton, G. A.; Savrasov, S. Y.; Humphreys, C. J.; Sutton, A. P. Electron-energy-loss spectra and the structural stability of nickel oxide: An LSDA+U study. *Phys. Rev. B* **1998**, 57,

1505.

[32] Turowski, M.; Margaritondo, G.; Kelly, M. K. Photoemission studies of $CuInSe_2$ and $CuGaSe_2$ and of their interfaces with Si and Ge. *Phys. Rev. B* **1985**, *31*, 1022.

[33] Ley, L.; Pollak, R. A.; McFeely, F. R. Kowalczyk, S. P. & Shirley D. A. Total valence band densities of states of III-V and II-VI compounds from x-ray photoemission spectroscopy. *Phys. Rev. B* **1974**, *9*, 600.

[34] Haarstrich, J.; Metzner, H.; Oertel, M.; Ronning, C.; Rissom, T.; Kaufmann, C. A.; Unold, T.; Schock, H. W.; Windeln, J.; Mannstadt, W.; Rudigier-Voigt, E. Increased homogeneity and open-circuit voltage of Cu(In,Ga)Se2 solar cells due to higher deposition temperature. *Sol. Energy Mater. Sol. Cells* **2011**, *95*, 1028.

[35] Caballero, R.; Kaufmann, C. A.; Eisenbarth, T.; Unold, T.; Klenk, R.; Schock, H.-W. High efficiency low temperature grown $Cu(In,Ga)Se_2$ thin film solar cells on flexible substrates using NaF precursor layers. *Prog. Photovolt: Res. Appl.* **2011**, *19*, 547.

[36] Niki, S.; Contreras, M.; Repins, I.; Powalla, M.; Kushiya, K. Ishizuka, S.; Matsubara, K. CIGS absorbers and processes. *Prog. Photovolt: Res. Appl.* **2010**, *18*, 453.

[37] Singh, J. Physics of Semiconductors and Their Heterostructures. *McGraw-Hill International*, **1993**.

[38] Rincón, C.; Márquez, R. Defect physics of the $CuInSe_2$ chalcopyrite semiconductor. *J. Chem.*

Phys. Solids **1999**, *60*, 1865.

[39] Matsumura, K.; Fujita, T.; Itoh, H.; Fujita D. Characterization of carrier concentration in CIGS solar cells by scanning capacitance microscopy. *Meas. Sci. Technol.* **2014**, *25*, 044020.

[40] Repins, I.; Contreras, M.; Romero, M.; Yan, Y.; Metzger, W.; Li, J.; Johnston, S.; Egaas, B.; DeHart, C.; Scharf J.; McCandless B. E.; Noufi R. National Characterization of 19.9%-Efficient CIGS Absorbers. *Conference Record of the Thirty Third IEEE Photovoltaic Specialist Conference* (2008) 11-16.

[41] Bhattacharya, R. N.; Contreras, M. A.; Egaas, B.; Noufi, R. N.; Kanevce, A.; J. R. Sites. High efficiency thin-film $CuIn_{1-x}Ga_xSe_2$ photovoltaic cells using a $Cd_{1-x}Zn_xS$ buffer layer. *Appl. Phys. Lett.* **2006**, *89*, 253503.

Chapter 7.

Concluding Remarks

In order to establish the hydrogen production process utilizing solar energy, achieving overall water-splitting using photocatalysts and photoelectrode systems have been a critical issue. In particular, materials consisting of mixed ion compounds such as oxynitrides and solid-solutions are attracting wide attention since there exists a broad range of controllability in their properties due to the varieties of their structural factors. So far, there have been reported many cases where well-balanced properties were achieved by preparing solid-solutions and mixed ion compounds. Usually, such materials are designed in terms of the macroscopic final properties of the related materials, such as bandgaps, band edge positions, and their chemical stabilities.

However, it is still difficult for researchers to understand their macroscopic properties based on the microscopic structural features, owing to the limit of the crystallographic measurements on such complex compounds. Yet, it is a great deal of importance to understand the relation between the properties and the structural features in order to realize more efficient material design, since such structural features generally have non-negligible influence on the final properties.

Here, in this thesis, I investigated the electronic structures of several mixed ion compounds from first-principle in order to figure out the characteristics and the origins their local structures. In addition, I aimed to relate their microscopic structural features to their macroscopic properties, in order

to provide the guidelines to control their properties and to enhance their activities as photocatalysts or photoelectrodes.

In the first half of this thesis, I mainly focused on the local structural factors such as anion orderings and octahedral-tiltings in perovskite oxynitrides. As a result, I clarified the features of such local arrangements and distortions in the materials, and their influences on the materials' electronic structures. In particular, it was revealed that the characteristic chemical bonds such as d-pπ interactions strongly relate to the structural factors and the photocatalyst related properties.

In the latter half, I shifted the focus to the state-of-art photocatalysts and photoelectrode materials that consist of solid solutions, and investigated the impacts of their compositions on the properties and the roles of their point defects. Here, the structural models were determined considering the microscopic features of the chemical bonds and the local distortions, based on the insights obtained in the previous parts. As consequence, several crucial issues such as the explanation for the compositional dependence of the photocatalytic activities and the origin of the p-type semiconducting properties of the solid solutions were unraveled, and consequently the guidelines to enhance their activities were provided.

Through the researches presented in this thesis, it was clearly demonstrated that the calculation values of the properties strongly depend on the microscopic structures of the models. In other words, it was revealed that only a little difference in the structural model may also result in a

crucial difference in the calculated properties, and here, the importance of preparing adequate structural models was provided.

In this thesis, although the structural models of the mixed ion compounds were constructed from microscopic structural units consisting of several atoms as the building blocks, based on the insights of local structural features such as preferred ionic distributions, the arrangements of such fundamental units were determined only by hand, and thus this procedure is not applicable to much larger structural models or to the comprehensive studies on a large number of materials. Hence, in order to realize the modelization of more complex or various compounds in a feasible way, the future researchers should establish the advanced methods where the arrangements of such fundamental units are determined automatically and exhaustively, by introducing a kind of informatical methodologies.

Publications stemming from this work

[1] A. Kubo, G. Giorgi, K. Yamashita, "Anion Ordering in $CaTaO_2N$: Structural Impact on the Photocatalytic Activity. Insights from First-Principles" *Chem. Mater.* **2017**, *29*(2), 539–545.

[2] A. Kubo, G. Giorgi, K. Yamashita, "$MgTaO_2N$ Photocatalysts: Perovskite *vs*. Ilmenite Structure. A Theoretical Investigation" *J. Phys. Chem. C*, **2017**, *121*(50), 27813–27821.

[3] A. Kubo, K. Yamashita, "First-principle investigations on the composition dependence of the photocatalytic related properties of $LaMg_xTa_{1-x}O_{1+3x}N_{2-3x}$" in preparation.